

HOPPING ALONG THE WAY: GENETIC ANALYSIS OF PILI-MEDIATED CHARGE  
TRANSPORT IN *GEOBACTER SULFURREDUCTENS*

By

Rebecca J. Steidl

A DISSERTATION

Submitted to  
Michigan State University  
in partial fulfillment of the requirements  
for the degree of

Microbiology and Molecular Genetics - Doctor of Philosophy

2015

## ABSTRACT

### HOPPING ALONG THE WAY: GENETIC ANALYSIS OF PILI-MEDIATED CHARGE TRANSPORT IN *GEOBACTER SULFURREDUCTENS*

By

Rebecca J. Steidl

*Geobacter sulfurreducens* is a dissimilatory iron-reducing bacterium that is able to utilize insoluble external electron acceptors such as Fe(III) oxides, radionuclides, and the anode of a microbial electrochemical cell (MEC). To accomplish this process it uses direct contact mechanisms involving a host of *c*-type cytochromes. It also produces microbial nanowires that are necessary for efficient growth with all of the aforementioned insoluble electron acceptors. The question is then: Are these nanowires transferring electrons to the acceptors, or are they merely a scaffold for electron transporting cytochromes. Thus, I investigated the contribution of electroactive pili to electron transfer (ET) to external electron acceptors as well as the mechanism of electron transfer in the pili.

In chapter 2 I demonstrate the necessity of nanowires for electron transfer through an anode biofilm by generating a mutant that displays only pili defects. Deleting gene encoding the pilus motor, PilB, produces a pili-deficient mutant with wild-type cytochrome expression that formed anode biofilms as thick (*ca.* 10  $\mu\text{m}$ ) as the wild type yet with reduced electroactivity. Furthermore, the growth and electroactivity of thicker biofilms required the expression and conductivity of the pili. The results support a model in which the conductive pili form a nanopower grid that permeates the biofilms to wire the cells in all biofilm strata to the underlying electrode. The pili operate coordinately with cytochromes in the lower strata until the biofilm reaches a threshold thickness where the pili are required as electronic conduits and thus without this function the biofilm is unable to continue to grow.

In chapter 3 I investigate the mechanism of pilus conductivity by generating amino acid replacements of residues predicted to be involved in ET in the pilus. Pili isolated from a Y27A mutant strain displayed a decreased ability to transfer electrons along the length of the pilus. This mutant, however, displayed no defects in biological external electron transfer assays. Electron transfer rates explained this phenotype, as the mutated pili were still able to transfer electrons faster than the acetate respiration rates. Two additional tyrosine residues, Y32 and Y57 were essential for MEC electroactivity, as were the negatively charged amino acids D53 and D54. Replacement of the three tyrosine residues with the aromatic amino acid phenylalanine, however, resulted in a strain with no reduction in electroactivity. Thus, the presence of these aromatic and charged amino acids is required for optimal charge transfer in the *G. sulfurreducens* pilus.

In Chapter 4 I develop a system to determine the role of intramolecular ET of the pilin monomer. To this end, I collaborated with Dr. Castro-Forero of the Worden Lab to generate a method for the *in vitro* production of soluble pilin monomers. These recombinant pilins were able to form conductive filaments *in vitro* and thus retain their ET capabilities. I then modified these recombinant pilins to attach to a gold electrode and used these self-assembled monolayers to study the role of intramolecular electron transfer. I generated several point mutations in the codons for aromatic and charged residues predicted to be involved in ET.

Copyright by  
REBECCA J. STEIDL  
2015

I would like to dedicate my dissertation to my parents Robert and Barbara Steidl. They constantly peaked my interest in science and the world around me, and were always supportive of my seemingly eternal academic career. My dad constantly showed me the wonders of biology from teaching me about different species of plants to bringing me interesting bugs or seeds containing multiple embryos that he found while working outside. His doctorate and research background let me know from a young age that I wanted to strive for the same. I know he would have loved to see me complete my doctorate.

## ACKNOWLEDGEMENTS

I would like to thank my parents Barb and Bob Steidl for their support through my long graduate career. You have always been supportive and helped me see the light at the end of the tunnel. I would also like to thank the Stern family, Laura, Travis and Ellie for providing me with reasons to leave the lab and go home (namely an adorable niece to play with) and sending random cards and care packages to make me smile. I would also like to thank Laura and Travis for the endless amount of help and support they have provided to my mom through first grief and later illness that I was not able to provide myself.

I would like to thank my boyfriend and next door lab neighbor Lee Macomber and my lab mate and best friend, Mike Manzella. You were both always there for me when I needed it and made my time in here exponentially better; this wouldn't have been possible without you. You were great science-related sounding boards and also many a family dinner would not have been possible without my best sous chefs. Also in attendance at many of my dinners and often assisting in food prep were many of my other good friends I made while in grad school, including Nik McPherson, Ben and Sarah Koestler, and Darin Quach. You are the best friends I've ever had and I hope we will stay in touch and play lots of D&D! I would like to also thank all present and past members of the Hungry Hungry Hippos Kickball team it was good to have a fun activity to organize with great people.

I would like to thank all past and present members of the Reguera Lab. I would like to thank my undergraduate researchers that have both contributed to my work and allowed me to grow as a teacher: Carlos, Mike, and Alex. In particular, Mike and Alex who both assisted in the many EPS isolations and cytochrome gels. I would like to thank Allison and Bhushan for help with my electrochemical work and Krista and Sanela for all of their CP-AFM work. I would like to thank Dena for her moral support and always being there to bounce ideas off of.

My committee members have also been integral to my graduate work and my success here: Dr. Bob Hausinger, Dr. Rob Britton, Dr. Mark Worden, and Dr. Cecilia Martinez-Gomez. You were very patient as I tried to schedule meetings and gave me needed perspective on my research, plans, and writing. I would also like to thank all of those in the Microscopy center for their help including Alicia, Melinda, and Abby. I would like to thank those that have collaborated with me on this work: Dr. Angelines Castro Forero and Dr. Gustavo Feliciano.

Last but certainly not least, I would like to thank Dr. Gemma Reguera for the advice and support during my tenure here. It took a long time but you stuck with me through all of it and offered me support through all of the challenges.

## TABLE OF CONTENTS

LIST OF TABLES .....	xi
LIST OF FIGURES .....	xii
KEY TO ABBREVIATIONS .....	xv
<b>CHAPTER 1. INTRODUCTION.....</b>	<b>1</b>
1.1 The <u>Geobacteraceae</u> .....	2
1.2 Extracellular electron transfer in <u>Geobacter sulfurreducens</u> .....	3
1.3 <u>Geobacter</u> pili structure and function .....	7
1.3.1 Overview of type IVa pili.....	7
1.3.2 The <u>G. sulfurreducens</u> pilin is divergent in structure and amino acid composition .....	9
1.4 Metallic-like conductance in pili.....	10
1.5 Alternative methods of electron transfer in pili .....	11
1.5.1 Tunneling .....	11
1.5.2 Hopping .....	12
1.5.3 Protein structure and charge (electron or hole) hopping.....	14
1.6 Dissertation outline .....	16
1.6.1 Mechanistic stratification in electroactive biofilms of <u>Geobacter sulfurreducens</u> mediated by pilus nanowires.....	16
1.6.2 Site-directed mutagenesis reveals the role of aromatic amino acids and local electrostatics in pilus conductivity and extracellular electron transfer .....	17
1.6.3 Intramolecular charge transport in pilus nanowires investigated in pilin-electrode interfaces.....	18
<b>CHAPTER 2. MECHANISTIC STRATIFICATION IN ELECTROACTIVE BIOFILMS OF <u>GEOBACTER SULFURREDUCENS</u> MEDIATED BY PILUS NANOWIRES .....</b>	<b>19</b>
2.1 Introduction.....	20
2.2 Materials and Methods .....	22
2.2.1 Bacterial strains and culture conditions .....	22
2.2.2 DNA manipulations and mutant construction.....	23
2.2.3 Microbial electrochemical cells (MECs).....	25
2.2.4 Static biofilm assays on plastic surfaces .....	26
2.2.5 Gene expression analyses by quantitative Real Time-PCR (qRT-PCR).....	26
2.2.6 Assays for c-type cytochrome content and profiling.....	27
2.2.7 Pili purification and conductivity measurements by CP-AFM.....	28
2.3 Results .....	29
2.3.1 Inactivation of the PilB assembly motor does not affect c-type cytochromes expression.....	29
2.3.2 Pili expression is required for optimal electrochemical activity of thin biofilms. ....	31
2.3.3 The expression and conductivity of the pili are required to grow thick biofilms. ....	33
2.4 Discussion .....	35

**CHAPTER 3. SITE-DIRECTED MUTAGENESIS REVEALS THE ROLE OF AROMATIC AMINO ACIDS AND LOCAL ELECTROSTATICS IN PILUS CONDUCTIVITY AND EXTRACELLULAR ELECTRON TRANSFER .....40**

3.1 Introduction.....41

3.2 Materials and Methods .....45

    3.2.1 Growth conditions .....45

    3.2.2 Mutant construction.....46

    3.2.3 Pili purification and conductivity analyses.....46

    3.2.4 Calculation of Fe(III) oxide respiratory rates.....48

    3.2.5 Electrochemical activity of anode biofilms in MECs .....48

3.3 Results and Discussion .....49

    3.3.1 Modeling the structure of the Geobacter pilus at high resolution via molecular dynamics.....49

        3.3.1.1 Potential ET pathways via aromatic residues .....50

        3.3.1.2 Potential ET pathway via the amide backbone .....52

        3.3.1.3 Contribution of the pilin’s charged amino acids to ET.....53

    3.3.2 The role of tyrosine residues in biofilm electroactivity and Fe(III) oxide reduction....54

    3.3.3 The effect of alanine replacement of Y27 on pilus conductivity .....55

    3.3.4 Effect of phenylalanine replacements of the pilus tyrosines.....57

    3.3.5 Effect of negatively-charged amino acids of the pilus .....58

3.4 Conclusions.....59

**CHAPTER 4. INTRAMOLECULAR CHARGE TRANSPORT IN PILUS NANOWIRES INVESTIGATED IN PILIN-ELECTRODE INTERFACES.....62**

4.1 Introduction.....63

4.2 Materials and Methods .....66

    4.2.1 Construction of Expression Strains .....66

        4.2.1.1 QIAexpress™ system (His-tagged pilins).....66

        4.2.1.2 pMAL™ system (MBP-tagged pilin) .....66

        4.2.1.3 IMPACT™ system (CBD-tagged pilins).....67

        4.2.1.4 Mutagenesis of codons for pilin amino acids.....67

    4.2.2 Expression of recombinant pilins.....68

    4.2.3 Purification of recombinant pilins carrying a Chitin-binding domain protein tag .....69

    4.2.4 Electrochemical characterization of PilA<sub>19</sub>-A20C monolayers on gold electrodes ....70

4.3 Results .....71

    4.3.1 Rationale for partially truncating the N-terminal hydrophobic pilin region.....71

    4.3.2 Construction and heterologous expression of recombinant pilins .....74

        4.3.2.1 Recombinant production of pilins carrying an N-t His-Tag .....74

        4.3.2.2 Recombinant production of pilins carrying a MBP.....75

        4.3.2.3 Recombinant production of pilins carrying a chitin-binding domain (CBD) .....77

    4.3.3 Electrochemical characterization of recombinant PilA<sub>19</sub>.....79

        4.3.3.1 Functionalization of PilA<sub>19</sub> with a cysteine tag and construction of pilin-electrode interfaces.....79

        4.3.3.2 Cyclic voltammetry of pilin-electrode interfaces .....80

        4.3.3.3 CP-AFM probing of pilin-electrode interfaces.....81

    4.3.4 Intramolecular pilin pathway investigated in mutated pilin-electrode interfaces .....82

4.4 Conclusions.....83

**CHAPTER 5. Conclusions and Future Directions .....86**

5.1 Review of project.....87

5.1.1 Review of mechanistic stratification in electroactive biofilms of <u>Geobacter sulfurreducens</u> mediated by pilus nanowires.....	87
5.1.2 Review of site-directed mutagenesis reveals a role of aromatic amino acids and local electrostatics in pilus conductivity and extracellular electron transfer .....	88
5.1.3 Review of intramolecular charge transport in pilus nanowires investigated in pilin-electrode interfaces .....	89
5.2 Future directions.....	90
5.2.1 Future directions for studying mechanistic stratification in electroactive biofilms of <u>Geobacter sulfurreducens</u> mediated by pilus nanowires .....	90
5.2.2 Future directions for site-directed mutagenesis to reveal the role of aromatic amino acids and local electrostatics in pilus conductivity and extracellular electron transfer .....	91
5.2.3 Future directions for examining intramolecular charge transport in pilus nanowires via pilin-electrode interfaces .....	93
<b>APPENDICES.....</b>	<b>95</b>
APPENDIX A MEC ADAPTATION IN PILB MUTANT STRAIN.....	96
APPENDIX B TABLES .....	101
APPENDIX C FIGURES.....	112
<b>REFERENCES .....</b>	<b>156</b>

## LIST OF TABLES

Table 1 Strains and plasmids used in Chapter 2 .....	102
Table 2 Primers used in Chapter 2.....	103
Table 3 Bacterial strains and plasmids used in Chapter 4 .....	105
Table 4 Primers used in Chapter 3.....	106
Table 5 Strains used in Chapter 4.....	107
Table 6 Primers used in Chapter 4.....	108
Table 7 Plasmids used in Chapter 4.....	110
Table 8 Buffers used to purify recombinant pilins as fusion proteins with a Chitin-binding Domain (CBD) using the IMPACT™ system using a chitin resin column .....	111

## LIST OF FIGURES

Figure 1 Structure of the PAK pilin and geopilin .....	113
Figure 2 Properties of the <i>G. sulfurreducens</i> pilin.....	114
Figure 3 $\pi$ -stacking configurations .....	115
Figure 4 Charge transfer mechanisms .....	116
Figure 5 Amide backbone charge hopping .....	117
Figure 6 Absorption spectra of oxidize and reduced cell extracts .....	118
Figure 7 Characterization of cytochrome content in pili-deficient mutant cultures.....	119
Figure 8 Expression of biofilm related genes in pilus deficient mutants .....	120
Figure 9 Phenotypic characterization of pili-deficient mutant (pilB, pilA, and pilA-E5A) biofilms .....	121
Figure 10 Biofilm electroactivity of selected mutants in MECs fed with 1 mM acetate .....	122
Figure 11 Current production as a function of biofilm thickness in the WT and pilB strains.....	123
Figure 12 Role of pilus conductivity in the growth and electroactivity of anode biofilms.....	124
Figure 13 Model of mechanistic stratification of electroactive biofilms .....	125
Figure 14 Surface maps of MS-optimized GS pilus.....	126
Figure 15 Potential charge transfer pathways identified in the MD model.....	127
Figure 16 Electron transfer paths predicted in the <i>G. sulfurreducens</i> pilus from the MD-refined pilus model.....	128
Figure 17 Surface exposure of Y32 and Y57 .....	129
Figure 18 Amide electron hole hopping and phenylalanine dimer intermolecular transfer pathway .....	130
Figure 19 Biofilm electroactivity in MECs fed with 3 mM acetate for Y32 and Y57 .....	131
Figure 20 Biofilm electroactivity in MECs fed with 3 mM acetate for Y27 amino acid replacement mutants.....	132

Figure 21 Transversal CP-AFM measurements of Y27 amino acid replacements .....	133
Figure 22 CP-AFM transport measurements along WT and Y27A pili .....	134
Figure 23 Electron transport rates per cell during growth of <i>G. sulfurreducens</i> with poorly crystalline Fe(III) oxides .....	135
Figure 24 Biofilm electroactivity of phenylalanine vs. alanine replacement in MECs fed with 3 mM acetate .....	136
Figure 25 Comparison of the reduction of external electron acceptors by Asp2 and Tyr3.....	137
Figure 26 NMR-derived PilA structural model of the <i>G. sulfurreducens</i> PilA and predicted structure of recombinant PilA <sub>19</sub> pilins.....	138
Figure 27 AGGRESCAN and Kyte-Doolittle analyses .....	139
Figure 28 Expression and purification of recombinant pilins carrying a 6×His-tag .....	140
Figure 29 Western blot analysis of periplasmic (left) and cytoplasmic (right) proteins fractions during the expression and purification of MBP-PilA <sub>20</sub> .....	141
Figure 30 Cleavage efficiency of PilA <sub>20</sub> from its MBP tag by Factor Xa protease.....	142
Figure 31 Production of PilA <sub>20</sub> subunits after treatment with Factor Xa protease.....	143
Figure 32 Expression of the full-length pilin (PilA) and various truncated pilins (PilA <sub>n</sub> ), all in fusions with a CBD tag (CBD-PilA <sub>n</sub> ) .....	144
Figure 33 Presence of pilin monomers in elution from chitin column after cleavage from CBD tag determined by 16-20% Tricine SDS-PAGE .....	145
Figure 34 Expression and purification of recombinant PilA <sub>19</sub> -A20C subunits .....	146
Figure 35 Effect of DTT on the electrochemical activity of PilA <sub>19</sub> -A20C pilins on a gold electrode .....	147
Figure 36 Effect of solvent (acetonitrile) in the deposition of PilA <sub>19</sub> -A20C on a gold electrode.	148
Figure 37 Effect of length of deposition time of PilA <sub>19</sub> -A20C in acetonitrile on a gold electrode .....	149
Figure 38 Effect of mixing and age of pilin sample on deposition of PilA <sub>19</sub> -A20C in acetonitrile .....	150
Figure 39 Effect of concentration and temperature of pilin sample on deposition of PilA <sub>19</sub> -A20C in acetonitrile.....	151
Figure 40 CP-AFM of PilA <sub>19</sub> -A20C monolayers on gold electrodes .....	152
Figure 41 Effect of amino acid substitutions on cyclic voltammograms.....	153

Figure 42 Test of media component limitation .....154  
Figure 43 Growth adaptation of pilB after extended incubation in MFC .....155

## KEY TO ABBREVIATIONS

AEM	anion exchange membrane
Ag/AgCl	silver/silver chloride reference electrode
ATP	adenosine triphosphate
BCA	bicinchoninic acid
BLAST	basic local alignment search tool
BSA	bovine serum albumin
C-t	C-terminal
CBD	chitin binding domain
CD	circular dichroism
CEM	cation exchange membrane
CLSM	confocal laser scanning microscopy
CP-AFM	conductive probe atomic force microscopy
CV	cyclic voltammetry
DBAF	fuel cell media
DI	deionized
DLS	dynamic light scattering
DMSO	dimethyl sulfoxide
DTT	dithiothreitol
$E^\circ$	standard redox potential
EDTA	ethylenediaminetetraacetic acid
EM	electron microscopy
EPS	exopolysaccharide

ET	electron transfer
FWAF	fresh water acetate fumarate
Gm	gentamycin
GRAVY	grand average of hydropathicity index
HEPES	4-(2-hydroxyethyl)piperazine-1-ethanesulfonic acid
HOPG	highly oriented pyrolytic graphite
HPLC	high performance liquid chromatography
/	current
IPTG	isopropyl-1-thio-D-galactopyranoside
LB	lysogeny media
MALDI	matrix assisted laser desorption ionization
MBP	maltose binding protein
MD	molecular dynamics
MEC	microbial electrochemical cell
MS	mass spectrometry
N-t	N-terminal
NA	numerical aperture
NBAF	nutrient broth acetate fumarate
NHE	normal hydrogen electrode
NMR	nuclear magnetic resonance
NTA	nitrilotriacetic acid
OD	optical density
OG	octyl $\beta$ -D-glucopyranoside
PBS	phosphate-buffered saline
PCET	proton coupled electron transfer

PCR	polymerase chain reaction
PSII	photosystem II
QCM	quartz crystal microbalance
R	resistance
RE	reference electrode
RNR	ribonucleotide reductase
RT	real time
SAM	self-assembled monolayer
SDS-PAGE	sodium dodecyl sulfate polyacrylamide gel electrophoresis
SEM	scanning electron microscopy
SHE	standard hydrogen electrode
Sp	spectinomycin
STM	scanning tunneling microscopy
TMBZ	3,3',5,5'-tetramethylbenzidine
TEM	transmission electron microscopy
TFP	type IV pili
UV-vis	ultraviolet-visible spectroscopy
V	voltage
WT	wild-type
YE	yeast extract

## CHAPTER 1. INTRODUCTION

## 1.1 The Geobacteraceae

The *Geobacteraceae* are a diverse family of dissimilatory iron reducers in the  $\delta$ -*proteobacteria*, thus sharing the ability to gain energy for growth from the reduction of Fe(III) coupled to the complete oxidation of acetate, other organic compounds, and hydrogen gas<sup>1</sup>. Because of this type of metabolism, members of the family are ubiquitous in environments where Fe(III) reduction is a significant process, particularly in subsurface environments. The genus *Geobacter* is perhaps the best studied and includes several model representatives with sequenced genomes and genetic systems<sup>2-5</sup>. All *Geobacter* spp. are mesophiles and prefer low salt and neutral pH<sup>1</sup>. Members within this genus are abundant in soils where Fe(III) reduction is an important ecosystem driver<sup>1</sup> and are often enriched on anode electrodes from sediment fuel cells, which harness electricity from the oxidation of organic compounds by the anode-associated bacteria in sediments using a cathode positioned at the aerobic zones<sup>6</sup>.

While *Geobacter* spp. are typically classified as strict anaerobes, some tolerate oxygen and can even grow with it as sole terminal electron acceptor for respiration under microaerophilic conditions<sup>7,8</sup>. This physiological trait allows them to survive and even boost their growth during oxygen intrusions into the soils and sediments for brief periods of time. Electron transfer (ET) is not restricted to Fe(III) oxides and other chemical electron acceptors. *Geobacter* are also able to transfer electrons to syntrophic partners<sup>9</sup> and often account for a significant proportion of the microorganisms that form methanogenic aggregates<sup>10</sup>. In addition, many members of the *Geobacteraceae* can degrade a wide variety of organic substrates, including common pollutants such as hydrocarbons<sup>11</sup> and chlorinated contaminants<sup>12</sup>, thus showing potential as bioremediation agents. Similarly, many members of the *Geobacteraceae* can reduce toxic metals such U(VI)<sup>13</sup> and the anode of a microbial fuel cell<sup>14</sup>, activities that show promise for the bioremediation of metal contaminants and bioenergy applications<sup>13,15-17</sup>.

## 1.2 Extracellular electron transfer in *Geobacter sulfurreducens*

The insoluble nature of Fe(III) oxides, the natural electron acceptor for the *Geobacteraceae*, has selected for a respiratory mechanism that allows the cells to establish direct electronic contact with the mineral. Such a strategy requires cells to first attach to the surface of the mineral and then transfer respiratory electrons across the cell envelope to terminal reductases of the outer surface, which can transfer electrons to the oxides. The most common iron reductases in dissimilatory iron reducers with a direct-contact mechanism are *c*-type cytochromes<sup>18</sup>. *Geobacter sulfurreducens*<sup>19</sup>, for example, one of the most well-studied bacteria in the *Geobacteraceae*, contains over 100 genes predicted to encode *c*-type cytochromes<sup>3</sup>. However, cytochrome conservation among *Geobacter* genomes is low. For instance, only 14 % of the cytochromes encoded in the genome (the equivalent to 2 % of all of the genes) of *G. sulfurreducens* are conserved across the *Geobacter* species<sup>1</sup>.

In addition to being the first species within the *Geobacteraceae* to have a sequenced genome<sup>3</sup>, *G. sulfurreducens* was also the first member in the family to become genetically tractable<sup>5</sup>. Therefore, much of the research on extracellular electron transfer in this family has been performed in *G. sulfurreducens*. Genetic studies support the idea that the unprecedented number of *c*-type cytochromes in this bacterium allows it to utilize a wide range of electron acceptors in addition to Fe(III) oxides, such as Mn(IV) oxides, U(VI) and the anode of a microbial fuel cell<sup>14,20–26</sup>. This wide range of reductases may also act as an “insurance policy”, whereby the removal of a key cytochrome is rapidly compensated by the expression of another or several more cytochromes<sup>22,27</sup>. Such redundancy allows *Geobacteraceae* to maintain different electron transfer pathways for the reduction of electron acceptors with different redox potentials<sup>28</sup>. This would be important for the utilization of the many different metal oxides and other electron acceptors available in the environment, which have different redox potentials<sup>29</sup>.

Because the pressure is high to directly contact the insoluble Fe(III) oxides in order to discharge respiratory electrons, *Geobacter* cells have evolved mechanisms to extend their electroactive surface beyond the confines of the outer membrane. One such method is to produce an exopolysaccharide (EPS) matrix that anchors c-type cytochromes<sup>30</sup>. The matrix also allows the cell to build electroactive biofilms on electrodes, thereby harnessing the respiratory activities of the biofilm cells as an electrical current<sup>30</sup>. Another important component of the electroactive biofilm matrix of *Geobacter* are type IV pili<sup>31,32</sup>, extracellular protein appendages used by many bacteria for surface attachment, translocation, and to provide structural support within multilayered biofilms<sup>33</sup>. As in other bacteria, the pili of *G. sulfurreducens* play a structural role in the biofilm matrix, allowing cells to grow as multilayered communities on inert and electron-accepting surfaces<sup>31,32</sup>. However, in contrast to other bacterial pili, those of *G. sulfurreducens* are conductive<sup>34</sup> and have been proposed to form a nanopower grid that wires the biofilms to an underlying electron-accepting surface such as Fe(III) oxides or an anode electrode poised at an oxidizing metabolic potential<sup>31,32</sup>. Furthermore, the pili are also required for the respiration of insoluble Fe(III) oxides<sup>34</sup>. These early findings relied heavily on genetic studies with a pilin-deficient mutant of *G. sulfurreducens*, which lacked pili and was impaired in its ability to transfer electrons to a variety of external electron acceptors<sup>13,31,34</sup>. However, the mutant was later reported to also have defects in c-type cytochromes of the outer membrane<sup>13,15</sup>, thus raising doubts about the role of the pili in electron transfer in planktonic cells and biofilms.

Evidence that the pili do in fact function as electronic conduits was provided by studies that examined the mechanism that allows *G. sulfurreducens* cells to reduce the soluble uranyl cation<sup>13</sup>. These studies demonstrated the correspondence between piliation, but not c-type cytochromes, and the ability of the cells to reduce the U(VI) extracellularly<sup>13</sup>. Hence, the pili are the primary site for uranium reduction<sup>13</sup>. By strongly binding the soluble uranyl cation and

reductively precipitating it as a mononuclear solid phase of U(IV) on the pilus fibers, the pili prevent the soluble uranyl ion from permeating and being reduced in the cell envelope, thus shielding the cell from the toxic effects of uranium<sup>13</sup>.

The role of pili in wiring electroactive biofilms remains, however, controversial. Cells within *G. sulfurreducens* biofilms transfer electrons to an underlying electrode at rates substantially higher than other species, even mixed cultures<sup>35</sup>. Genetic studies have identified only one cytochrome, the matrix-bound cytochrome OmcZ<sup>30</sup>, as required for biofilm electroactivity<sup>20</sup>. OmcZ is an outer membrane c-type cytochromes that is proteolytically digested into a small form, OmcZ<sub>s</sub>, for export to the biofilm matrix<sup>20</sup>. OmcZ<sub>s</sub> localizes preferentially to the biofilm layers closer to the electrode surface<sup>36</sup>, suggesting a role in electronically connecting the biofilm to the electrode. Other cytochromes of the biofilm matrix may participate in electron transfer. However, genetic studies have failed to identify cytochromes other than OmcZ essential to ET in the anode biofilms, presumably because of the redundancy and compensatory adaptations often observed in cytochrome mutants<sup>22,27</sup>.

Electrochemical studies also demonstrated that the c-type cytochromes of the electroactive biofilm matrix can be reversibly oxidized or reduced depending on the anode potential<sup>37,38</sup>. In thin biofilms (1-2 cells thick), all cytochromes are reduced at positive voltages whereas in thick biofilms (ca. 20 μm thick) only fifty percent of cytochromes in the biofilm remain reduced<sup>38</sup>. Furthermore, a cytochrome redox gradient is established across thick biofilms, whereby the concentration of electrons is higher in the upper layers and decreases progressively towards the electrode-attached biofilm<sup>39</sup>. Such an electron gradient is predicted to drive ET from the upper to the lower strata of the biofilm. However, it also suggests that the conduction of electrons via cytochromes becomes limiting as the biofilm grows progressively away from the electron-accepting anode. The low redox potential of the upper strata of thick biofilms may begin as little as 10 μm from the oxidizing electrode based on source-drain

experiments<sup>39</sup>. Yet, despite this limitation, current production increases linearly with the biofilm thickness<sup>31</sup> and cells in the upper layers of thick biofilms remain metabolically active<sup>40</sup> and contribute to current production<sup>31</sup>.

The pili could be the elusive electronic conduits that allow cells in the upper stratum to maintain optimal catalytic currents. Not only are they conductive and required for the reduction of Fe(III) oxides<sup>34</sup> and the uranyl cation<sup>13</sup>, they are also required for efficient current production in MECs<sup>31</sup>. Furthermore, the pili provide structural support to the biofilms<sup>32</sup>, and pili-deficient strains only form thin biofilms and produce low levels of current<sup>31</sup>. However, the pili-defective strains used in earlier studies (the pilin-deficient  $\Delta pilA$  mutant<sup>34</sup> and the pili regulator mutant  $\Delta pilR$ <sup>41</sup>) also have defects in the expression of outer-membrane cytochromes<sup>13,41</sup>. Hence, the observed phenotypes could have been caused by the pilus deficiency, the cytochrome defects, or both. The role of pili as electronic conduits has also been challenged by the report that polyclonal antibodies raised against the outer membrane cytochrome OmcS bind pili in chemically-fixed preparations of pilated cells<sup>42</sup>. This has led to the proposal that OmcS, and perhaps other cytochromes, bind to the pili and contribute to its conductivity<sup>42</sup>. Results from this study are, however, difficult to interpret because the pili preparations were chemically fixed and the polyclonal antibodies could have bound non-specifically to the pili. Furthermore, when cell-associated pili were deposited on graphite without any type chemical treatment and then probed by scanning tunneling microscopy, they showed conserved topographic features of type IV pili and electronic features consistent with hotspots of conductivity; however, none of the electronic signatures matched those typical of the heme groups of *c*-type cytochromes<sup>43</sup>. Hence, the contribution of the pilus protein matrix and the potential of pilus-associated cytochromes to facilitate electron transfer remains controversial.

Recently, biofilms of the Aro-5 strain of *G. sulfurreducens*, which carries alanine replacements in five of the six aromatic amino acids of the pilin (including all tyrosine residues),

were shown to have reduced conductivity while still associating with the cytochrome OmcS on the pili<sup>44</sup>. As aromatic amino acids, in particular tyrosine residues, have been proposed to contribute to the pilus conductivity<sup>45</sup>, these results suggest that some or all of these amino acids are required for pilus conductivity and, consequently, that pili are necessary for biofilm electroactivity. However, potential effects of the extensive mutagenesis on the integrity of the pilus structure were never investigated<sup>46</sup>. Furthermore, defects in cytochrome production in the electroactive biofilms by the Aro-5 strain, which have been reported for other pili-deficient mutants<sup>13,15,41</sup>, were not evaluated in this study<sup>46</sup>. Thus, the role of pili as electronic conduits to external electron acceptors remains controversial.

### **1.3 Geobacter pili structure and function**

#### **1.3.1 Overview of type IVa pili**

Type IVa pili are thin (6 to 9 nm in diameter) pilus filaments that are assembled on the cell envelope and can grow to several microns in length. Despite their small diameter, type IVa pili are very strong and can withstand elastic forces of up to 110 pN<sup>47</sup>. They are widespread in bacteria, particularly in the  $\beta$ ,  $\gamma$ , and  $\delta$  subdivisions of the *Proteobacteria*, and serve various functions such as surface motility, microcolony and biofilm formation, surface adhesion, immune evasion, cell signaling, transformation of DNA, and phage attachment<sup>48</sup>. Despite their multiplicity of functions, they are surprisingly simple at the biochemical level, consisting of a single peptide subunit or pilin that polymerizes via hydrophobic interactions at the base of the fiber in a repeating, helical fashion. Hydrophobic interactions between adjacent subunits are mediated by the conserved N-terminal (N-t)  $\alpha$ -helix of all type IVa pilins, a region that can be further divided in two domains: the highly conserved and hydrophobic  $\alpha$ 1-N, which spans approximately the first 25 amino acids of the pilin's N-t, and the  $\alpha$ 1-C that contains a similar number of amino acids in the C-terminal (C-t) end of the  $\alpha$ -helix (Figure 1). In addition, most bacterial type IVa pilins

also contain a variable globular head of four anti-parallel  $\beta$ -sheets connected to the C-t end of the  $\alpha$ -helix via an  $\alpha\beta$ -loop, which mediates pilin-pilin interactions<sup>49</sup>. After the globular domain, there is also a highly variable region or D-region containing two conserved cysteine residues<sup>50</sup>. The globular domain and D-region confer on the pili much of their surface chemistry and biological functions such as cell-cell aggregation, adhesion, and surface motility and also stabilize the pilus filament through pilin-pilin interactions<sup>48</sup>.

Another conserved feature of type IVa pilins is that they are synthesized as a precursor or prepilin, which carries a short hydrophilic signal peptide at the N-t end. The last amino acid of this signal peptide is a conserved glycine and is recognized and required for efficient cleaving of the signal peptide by a dedicated prepilin peptidase<sup>51,52</sup>. Also conserved are the phenylalanine at position 1 (F1) of the processed pilin, which is methylated by the signal peptide upon cleavage of the signal peptide<sup>52</sup>, and the glutamic acid at position 5 (E5), which interact during assembly to align the incoming pilin at the base of the growing pilus fiber<sup>51,52</sup>. Also conserved are proteins of the type IVa apparatus required for pilin assembly such as PilC and ATPases that polymerize (PilB) and depolymerize (PilT) the pilins to maintain optimal cycles of protrusion and retraction<sup>53</sup>.

Structural studies of type IVa pili and their pilin subunit have proven difficult due to the insoluble nature of both. The small diameter and smooth surface of the pili make the structural characterization of type IVa pili difficult. The pilins, on the other hand, are insoluble due to the highly hydrophobic  $\alpha$ 1-N region, making NMR and X-ray crystallography approaches challenging as well. Despite these hurdles, full and truncated type IVa pilin structures have been crystallized and an NMR-derived structure for the pilin of *G. sulfurreducens* in lipid micelles is available<sup>49,54–65</sup>. Structural information is also available for two type IVa pili: a computational model of the *P. aeruginosa* strain K (PAK) pili (derived from X-ray fiber diffraction data)<sup>50</sup> and the pseudoatomic model of *Neisseria gonorrhoea* (GC) pili (constructed from the pilin's crystal

structure and cryo-electron microscopy [cryoEM])<sup>66</sup>. The most detailed experimental structure is that of the GC pilus, which was generated by fitting the crystal structure of a full-length GC pilin into a model of the GC pilus fiber reconstructed with 12.5 Å resolution by cryoEM<sup>66</sup>. The structure reveals a pilus with a diameter of approximately 60 Å with an inner hydrophobic core of 6 to 11 Å in diameter. The α1-N region of each pilin is buried in the fiber's core, which accounts for 75 % of the total buried surface area of the pilus. Furthermore, the pilus has a symmetry of 3.6 pilins per turn with a 10.5 Å rise between subunits<sup>66</sup>.

### **1.3.2 The *G. sulfurreducens* pilin is divergent in structure and amino acid composition**

The type IVa pilins of the family *Geobacteraceae* are shorter than other bacterial pilins and form an independent line of descent; for this reason they are sometimes referred to as 'geopilins'<sup>34</sup>. They contain the conserved α1 helix of other type IVa pilins, but lack the globular domain and D-loop of other type IVa pilins, which are replaced with a short C-t random coil<sup>45</sup>. As shown in Figure 1 for the pilin of *G. sulfurreducens*, this large truncation makes the pilin structure primarily α-helical. As with other characterized pilins, the α1-C region of the α1 helix has less sequence homology than the conserved α1-N region required for pilus assembly<sup>50</sup>. It is in this α1-C region of the pilin of *G. sulfurreducens* as well as in the C-t random coil where several aromatic amino acids conserved in the *Geobacteraceae* are located<sup>34</sup> (Figure 2)

The C-t random coil region is also highly flexible and mobile with no fixed position, as observed in the NMR structure of the *G. sulfurreducens* pilin<sup>58</sup> (Figure 2). Because the structural differences between the *G. sulfurreducens* pilin and other bacterial pilins are so profound, the predictive value of structural models for the PAK and GC pilins is limited. To address this limitation, my group collaborated with Drs. Artacho (University of Cambridge, U.K.) and Feliciano (University of Sao Paulo, Brazil) to generate a structural model of the pilin of *G. sulfurreducens* in solution via molecular dynamics (MD) simulations<sup>45</sup>. The electrostatic potential

of the pilin revealed in the simulations displayed a dipole along the length of the monomer with negative electrostatic region at the C-terminus and a positive region in the middle of the polypeptide confirming those calculated previously (Figure 2). This dipole was not merely due to the structure of the peptide as a poly-alanine peptide displayed no such effect<sup>45</sup>. The large dipole could dramatically increase the ET rate through the polypeptide similar to the effect of the natural dipole created by the N-terminus and C-terminus ends of helical peptides<sup>67,68</sup>. The pilin model also predicted that the pilin monomer is conductive with a band gap similar to conventional semiconductors and charge transfer would be more favorable in one direction<sup>45</sup>.

Evidence also suggests that type IVa pilins are post-translational modified and that such chemical modifications contribute to pili functions such as twitching motility, aggregation, attachment, and binding<sup>51,62,69-73</sup>. The role of post-translational modifications in *G. sulfurreducens* pilin are not known, except for an isolated report that suggested that one tyrosine of the pilin (Y32) could be modified with a glycerophosphate<sup>74</sup> as reported for other bacterial pilins<sup>75</sup>. Such post-translational modifications may be particularly relevant for a metal reducer such as *G. sulfurreducens*. For example, the S-layer of the bacterium *Bacillus sphaericus* JG-A12 is post-translationally modified with phosphate groups for efficient binding of uranium<sup>76</sup>.

#### **1.4 Metallic-like conductance in pili**

As mentioned earlier, the *G. sulfurreducens* pilus is conductive<sup>34</sup> and required for *G. sulfurreducens* to transfer electrons to a variety of external electron acceptors<sup>13,31,34</sup>. However, the mechanism by which this filament is conductive remains controversial. The temperature dependence of piliated anode biofilms and crude preparations of pili dried on electrodes has been interpreted as the pili behaving like metallic conductors<sup>77</sup>. However, this interpretation has been challenged based on limitations of the electrochemical approach used for the conductivity

measurements and the fact that the crude preparations of pili contained other proteins, including *c*-type cytochromes<sup>78</sup>. The metallic model of pilus conductance relies heavily on the assumption that aromatic residues of the pilus are clustered sufficiently so as to maintain inter-aromatic distances (*ca.* 3 Å) and configurations (sandwich type) that promote  $\pi$ -stacking<sup>79</sup> (Figure 3). Such configurations are unstable and rarely seen in proteins due to their rigidity<sup>80</sup>. Furthermore, it is unlikely that dynamic appendages such as pili can stably maintain these aromatic stacking geometries because even subtle dealignments or increases in inter-aromatic distances can have dramatic effects on charge mobility<sup>81,82</sup>. Furthermore, homology models of the *G. sulfurreducens* pilus reveal inter-aromatic residues too large (15-21 Å)<sup>83</sup> to support  $\pi$ -stacking and metallic conductance. However, more refined structural models are necessary to test the model of metallic conductance.

## **1.5 Alternative methods of electron transfer in pili**

In addition to the proposed metallic-like conductance there are two other well characterized mechanisms for ET in proteins: electron tunneling and hopping (Figure 4).

### **1.5.1 Tunneling**

One well-established mechanism of ET in proteins is via electron tunneling<sup>84</sup>. This mechanism is based on quantum mechanics rather than classical mechanics and it involves the direct transfer of an electron from donor to acceptor through the barrier (Figure 4). This process creates the first defining factor of electron tunneling: it is relatively temperature independent<sup>85</sup>, unlike classical thermodynamics. Because of the quantum-mechanical nature of electron tunneling, ET rates decrease exponentially with distance<sup>84</sup>. Hence, the ET rate constant for tunneling is an exponential function dependent on the decay constant and the distance between the donor and acceptor<sup>84</sup>. Because of this, ET over 14 Å<sup>86</sup> to 20 Å<sup>84</sup> becomes too slow to be biologically relevant.

Tunneling has been primarily studied by Gray and colleagues using flash-quench techniques that measured ET rates in ruthenium-modified metalloproteins. In these studies, the electrons tunnel from the metal cofactor (e.g., Cu in azurin) to a Ru moiety attached to histidine residues of the proteins positioned at defined distances from the metal cofactor<sup>84</sup>. The results of their studies demonstrated the exponential distance dependence and temperature independence of the ET rates, which were in the order of milliseconds at distances of about 20 Å at 170 K<sup>84</sup>.

Electron tunneling has been demonstrated in electrochemical studies of short helical peptides, however at lengths greater than 20 Å evidence does not support a single step tunneling mechanism<sup>87-89</sup>. As the pilins themselves are longer (ca. 80 Å) than both predicted and demonstrated single-step tunneling mechanisms for ET, it is highly unlikely that tunneling regimes are the primary mechanism of ET through the pilin or pilus.

### **1.5.2 Hopping**

In contrast to the quantum mechanical electron tunneling mechanism, electron hopping occurs by the classical theory of ET. As such, the electron is transferred via redox active groups that function as “stepping stones” (Figure 4). Because in the hopping model electrons do in fact reside in the relay residues, activation energies must be overcome for ET to occur leading to a strong temperature dependence. As the electron makes shorter hops from redox active site to site, the rates of ET no longer show a strong distance dependence and the rate constant is instead a linear function of the distance between the acceptor and donor<sup>90</sup>.

One amino acid commonly involved in electron hopping in proteins is tryptophan which is well-characterized in ET in several proteins such as photolyase<sup>91</sup> and ribonucleotide reductase (RNR)<sup>92</sup>. However as the pilin monomer contains no tryptophan residues, they cannot be involved in ET in the *G. sulfurreducens* pilus. Tyrosine residues have also been implicated in electron hopping in several well-studied proteins, such as RNR and within the photosystem II

(PSII) complex. In RNR an electron is transferred more than 35 Å along an established pathway: Y122→W48→Y356→Y731→Y730→C439<sup>92</sup>. This is one of the longest distances for ET recorded in a protein. The space between W48 and Y731 is 25 Å, with Y356 the only redox active residue between<sup>92</sup>. This means that a jump of more than 12.5 Å must be necessary. In PSII, on the other hand, a tyrosine residue transfers an electron to the next carrier, P<sub>680</sub>, over distances estimated to range from 8.3<sup>93</sup> to 13.8<sup>94</sup> Å. Thus, even though many hopping steps are required to enable long distance transfer, the individual steps can be greater than 12 Å in length themselves. Because removal of an electron from a tyrosine requires an oxidation potential (1.46 V vs NHE)<sup>92</sup> much higher than those that operate in biological systems, electron hopping via tyrosines in proteins occurs by a proton coupled electron transfer (PCET) reaction<sup>92</sup>. Acidic residues, histidine, and cysteine have been documented to act as proton acceptors for tyrosines in PCET reactions<sup>92,95,96</sup>. The removal of a proton from the tyrosine by these amino acids lowers the oxidation potential of the tyrosine residue and facilitates ET.

In addition to work characterizing protein systems, Cordes *et. al* developed a system to study ET rates in synthesized peptides<sup>97</sup>. This system was used to investigate the relay capabilities of aromatic amino acids<sup>97</sup>. The studies demonstrated that the presence of redox-active peptide side chains increases charge transfer rates along these peptides<sup>97</sup>. They also showed that redox-active amino acids such as tyrosine and redox-active aromatic derivatives can act as “stepping stones” in the middle of these peptides<sup>98</sup>.

The aromatic amino acid phenylalanine has a predicted redox potential (2.2 V vs. NHE)<sup>99</sup> much higher than any other aromatic residue and too high to allow it to function as a relay amino acid in an ET pathway *in vivo*; however, in several cytochrome *c* proteins studied, phenylalanine residues are surprisingly essential for optimal ET rates<sup>100,101</sup>. Electronic structure calculations in bacterial NADH:ubiquinone oxidoreductase have also identified conserved phenylalanine residues as essential to ET<sup>102</sup>. One phenylalanine in particular, F328, was

involved in all the fast paths of ET identified. Peptide systems have also been used to investigate the role of phenylalanine residues as stepping stones in ET<sup>103</sup>. Despite having an oxidation potential higher than that of its final electron acceptor, a phenylalanine residue in the middle of the peptide still resulted in a high ET efficiency. Surprisingly, this efficiency was slightly higher than a similar peptide carrying a redox-active methoxy-substituted relay instead of a phenylalanine, suggesting that, despite its high oxidation potential, the phenylalanine was able to act as a stepping stone.

### **1.5.3 Protein structure and charge (electron or hole) hopping**

*In vitro* studies have demonstrated that peptides, particularly helical ones, allow electrons to hop through the peptide backbone. Interestingly, electrons hop up to 120 Å; a distance significantly longer than the *G. sulfurreducens* pilin<sup>68,88</sup>. Hopping down the length of a peptide is theorized to occur via the amide groups of the peptide backbone,<sup>88</sup> with the amide taking on a positive charge. *Ab initio* calculations of single amino acids injected with an additional positive charge support this model, as 88 % of the introduced positive charge resides in the amide region<sup>90</sup>. Thus, hopping by this method is theorized to occur by electron hole hopping where the electron would first hop to the acceptor R-group and then the cation radical would hop along the amide groups to the electron donor<sup>88</sup> (Figure 4). Therefore, the amide region of a peptide may play an important role in charge transfer. In addition to the amide region, electron-rich bonds may also act as stepping stones and contribute to hopping. When the *ab initio* calculations were repeated on a serine residue modified with an alkene-rich side group, the amide region held only 68 % of the positive charge injected and 22 % of the charge resided in the electron-rich side group<sup>90</sup>. Electrochemical studies confirmed the contribution of these electron-rich groups to hopping while also demonstrating the negative role that backbone rigidity plays on charge transfer<sup>90</sup>. Hence, electron-rich groups not typically thought to be involved in charge transfer could in fact participate in charge hopping and could help explain

perplexing observations about phenylalanine residues acting as stepping stones for hole hopping<sup>103</sup>.

It has also been proposed that other non-traditional sources may act as stepping stones for charge transfer including the formation of lone pair –  $\pi$  three electron bonds ( $lp:\pi$ )<sup>104</sup>, lone pair – lone pair ( $lp:lp$ ) three electron bonds<sup>105</sup>,  $\pi$  –  $\pi$  three electron bonds ( $\pi:\pi$ )<sup>106</sup>, and the C-terminus of  $\alpha$ -helices<sup>107</sup>. As the aromatic residues are essential to the conductivity of the pili, the  $\pi:\pi$  bond is of particular interest. This mechanism of hole hopping is similar to  $\pi$  –  $\pi$  interactions mentioned earlier in that two aromatic rings must come *ca.* 3 Å from each other to facilitate ET. However, by the hole hopping mechanism, the formation of a hole causes the two rings to be brought closer together followed by the formation of a delocalized three electron bond between the rings. Calculations predict that subsequent separation of the rings will promote the electron hole relay to another group along the peptide. This contrasts with  $\pi$ - $\pi$  interactions for metallic-like conductance, which require a near static ring position and distance across the pilus. Thus, the advantage of hole hopping is that even transient aromatic interactions and thus limited  $\pi:\pi$  bonding could facilitate the movement of the hole relay<sup>106</sup>. Furthermore, because this is an electrostatic interaction, there's no barrier to overcome to transition to this state.

The rate of charge transfer via the backbone hopping method has been shown to increase with the natural dipole moment of a helical peptide<sup>67,108–110</sup>, from positive to negative. Hydrogen bonding naturally present in  $\alpha$ -helices is also predicted to increase ET through these peptides (Figure 5). Short peptides unable to form hydrogen bonds exhibit a decreased rate constant with additional length that is consistent with one-step tunneling. However, as longer peptide lengths permit hydrogen bonding, a transition is observed whereby a hopping mechanism takes over<sup>111</sup>. Similar relationships between the hydrogen bond number and rate constants of ET have been demonstrated in other peptide systems<sup>112–114</sup>. As mentioned earlier,

the flexibility of molecules also affects ET<sup>90</sup> and, as such, the natural movement and flexibility of organic structures such as DNA and peptides is predicted to increase their charge transfer rates<sup>115,116</sup>.

As stated earlier, the *G. sulfurreducens* pilin is predominantly an  $\alpha$ -helical structure with a narrow electronic band gap contributed in part by the peptide's large dipole<sup>45</sup>. Given that  $\alpha$ -helices are structures that promote charge transfer and that the rate of charge transfer is affected by the dipole of the peptide, the structure of the pilin is consistent with a peptide environment evolved for intramolecular charge transport by the hopping mechanism. Furthermore, once the pilins assemble, the aromatic amino acids of the pili could cluster sufficiently to create additional pathways for charge hopping through the pilus. Hence, inter- and intramolecular pathways likely mediate charge hopping in the pilus. Because of its complexity, it is important to dissect the contribution of both.

## **1.6 Dissertation outline**

### **1.6.1 Mechanistic stratification in electroactive biofilms of *Geobacter sulfurreducens* mediated by pilus nanowires**

Chapter 2 describes genetic studies to elucidate the role of conductive pili in electroactive biofilms formed on the anode electrode of MECs fed with acetate. The effect of several pili-inactivating mutations on biofilm formation and conductivity and epistatic effects on *c*-type cytochromes production were studied. A deletion mutant (*pilB*), which cannot produce the PilB ATPase that polymerizes pilins, had no detectable changes in cytochrome production or localization, and provided the elusive genetic tool needed to assess the contribution of pili to the growth and electrochemical activity of anode biofilms. A strain that produces pili with reduced conductivity was also analyzed. The results supported a model of mechanistic stratification in anode biofilms mediated by the conductive pili, whereby pili and cytochromes

work coordinately to transfer electrons to the underlying electrode until the biofilm reaches a threshold thickness (ca. 10  $\mu\text{m}$ ) that limits the efficiency of the cytochrome pathway but not of the pili.

All of the experiments reported in this chapter were conducted by me, except for the conductivity measurements with a conductive probe atomic force microscopy (CP-AFM), which were performed by a post-doctoral member of our lab, Dr. Sanela Lampa-Pastirk.

### **1.6.2 Site-directed mutagenesis reveals the role of aromatic amino acids and local electrostatics in pilus conductivity and extracellular electron transfer**

Chapter 3 describes the mutational analysis of key residues in the pilus predicted to be involved in ET along the pilus. A homology model for the *G. sulfurreducens* pilus was refined by MD simulations by Dr. Feliciano and then used to predict potential ET pathways in the pilus. Residues implicated in a hopping pathway of ET include the pilin's three tyrosine residues (Y27, Y32, and Y57) and several residues that contribute to a natural dipole in the pilus (D53, D54, and R28). Alanine replacement mutations were generated in the gene encoding the pilin to substitute these residues and study their effect in pilus conductivity *in vivo* (electrochemical activity of biofilms in MECs and growth in Fe(III) oxide cultures). Some of the variant pili were then purified and their transversal and axial conductivities were measured with a conductive probe atomic force microscope (CP-AFM). The experimental data were used to calculate the ET rates of individual pilus fibers and that of piliated cells respiring Fe(III) oxides or anode electrodes. The results support the predictions of the MD model, which indicated that the clustering and configuration of the aromatic residues is critical for optimal multistep hopping. They also revealed redundant pathways for ET in the pilus and potential paths for the transfer of electrons from the pilus to external electron acceptors such as Fe(III) oxides and the uranyl cation.

All of the experiments reported in this chapter were conducted by me, except for the conductivity measurements by CP-AFM, which were performed by, Dr. Sanela Lampa-Pastirk. Assistance from Dr. Allison Speers setting up the Fe(III) oxides cultures is acknowledged.

### ***1.6.3 Intramolecular charge transport in pilus nanowires investigated in pilin-electrode interfaces***

Chapter 4 describes the heterologous expression of truncated pilin monomers of *G. sulfurreducens* and their deposition as pilin monolayers on gold electrodes to isolate and study the intramolecular ET pathway of the pilus. Protein expression constructs of truncated pilins were generated using the following systems: QIAexpressionist, pMAL, and IMPACT. The expression and purification conditions were then optimized for the mass-production of recombinant pilins. One of them, PilA<sub>19</sub>, which was purified at high yields, was modified with an N-terminal cysteine to attach it to gold electrodes as a confluent monolayer. The conductivity of the pilin monolayer was demonstrated by cyclic voltammetry (CV). Furthermore, CV was also performed on the mutated pilin monolayers, which carried alanine replacements in residues predicted to be involved in pilin conductivity (Y27, Y32, Y57, D53, D54, and R28). The results suggest that intramolecular ET is not influenced by these amino acids. Potential limitations of the interfaces to unmask the mutant defects are discussed.

All of the experiments reported in this chapter were conducted by me, except for the optimization of the expression and purification of the recombinant pilins, which was performed by my collaborator Dr. Castro Forero (a graduate student in the lab of Dr. R. Mark Worden, Department of Chemical Engineering). She used the selected recombinant pilin to assemble conductive pili *in vitro*. I am also grateful to Dr. Bhushan Awate for his invaluable help in the early phase of the electrochemical experiments.

**CHAPTER 2. MECHANISTIC STRATIFICATION IN ELECTROACTIVE BIOFILMS OF  
*GEOBACTER SULFURREDUCTENS* MEDIATED BY PILUS NANOWIRES**

## 2.1 Introduction

The ability of *Geobacter* bacteria to completely oxidize organic compounds to CO<sub>2</sub> with an electrode poised at a metabolically oxidizing potential shows promise for the conversion of organic wastes and renewable biomass into electricity, hydrogen gas, and/or liquid fuels in microbial electrochemical cells (MECs)<sup>16,17,117</sup>. Energy recoveries in these devices depend in a great manner on the electroactivity of the electrode-associated biofilms<sup>118</sup> yet the mechanism of conductance is not fully understood. Genetic studies in the model representative *Geobacter sulfurreducens* have been instrumental to identify biofilm components required for biofilm formation and electroactivity. Among the identified genes are those encoding the Xap exopolysaccharide (EPS), which are required for the development of multilayered biofilms and for anchoring redox-active proteins, mainly *c*-type cytochromes<sup>30</sup>. Although the genome of *G. sulfurreducens* contains over 100 open reading frames annotated as *c*-type cytochromes, many of which are essential for the reduction of extracellular electron acceptors<sup>21,22,119</sup>, genetic studies have identified only one cytochrome, the matrix-associated OmcZ, as essential for biofilm electroactivity<sup>120</sup>. Other cytochromes may be required, but their genetic identification is challenging because of compensatory effects observed in some cytochrome mutants<sup>22,27</sup>.

The matrix-associated *c*-type cytochromes can be reversibly oxidized or reduced depending on the anode potential<sup>37,38</sup>, consistent with their role as electron carriers in the biofilms. However, redox potentials decrease in biofilm layers positioned *ca.* 10 μm or further away from the electrode, and a redox gradient is established whereby more electrons are concentrated in the upper, electron acceptor-limited biofilm stratum and decrease progressively towards the electrode-attached layers<sup>39</sup>. The redox gradient provides the driving force for electron transport across the biofilms in a manner analogous to how electrons diffuse through redox polymers by hopping among immobilized redox cofactors<sup>121</sup>. Consistent with this process, while it is possible to reduce all of the biofilm cytochromes of thin (< 10 μm) biofilms when the

potential is set at a positive voltage, only half are reduced in thicker (ca. 20  $\mu\text{m}$ ) biofilms<sup>38</sup>. Yet, despite this limitation, *G. sulfurreducens* can grow electroactive biofilms that are tens of micrometers from the electrode surface while generating current proportionally to the biofilm thickness<sup>31</sup>. Furthermore, the cells in the biofilm layers farthest from the anode surface are metabolically active and continue to oxidize acetate while contributing to current production<sup>40</sup>. This result suggests that electron carriers other than cytochromes operate in electroactive biofilms, particularly in the upper stratum of thick biofilms.

Biofilm formation in *G. sulfurreducens* also requires the expression of conductive protein filaments termed pili<sup>31</sup>. The pili permeate the biofilm matrix and provide structural support for the growth of the multilayered community<sup>32</sup>. Yet their conductive properties<sup>34</sup> suggest they could also form a nanopower grid across the biofilms to electronically connect the biofilm cells to the underlying electrode<sup>31</sup>. The pili have also been proposed to anchor cytochromes, inasmuch as polyclonal antibodies raised against the outer membrane c-type cytochromes OmcS hybridize to antigens along chemically-fixed, cell-associated pilus fibers<sup>42</sup>. Because the pili are part of a biofilm matrix with abundant cytochromes, they may also function as electronic conduits between the biofilm cells and the matrix-associated cytochromes, similarly to how planktonic cells use the pili to electronically connect with extracellular electron acceptors such as Fe(III) oxides<sup>34</sup> and uranium<sup>13</sup>.

Much of the difficulty in assessing the contribution of the pili to biofilm electroactivity stems from the fact that pili-deficient mutants reported thus far also have defects in cytochromes required for extracellular electron transfer<sup>13,15,41</sup>. Deleting the gene encoding the pilus subunit (the PilA pilin), for example, prevents pili formation and decreases current production by biofilms<sup>31</sup>. However, the mutation also results in defects in outer membrane cytochromes<sup>13</sup> and prevents the expression of OmcZ in the biofilm matrix<sup>15</sup>. Interestingly, replacement of the pilin's 5 aromatic amino acids with alanines resulted in a strain (Aro-5) that formed thick anode

biofilms yet had reduced conductivity<sup>44</sup>. The study did not investigate potential pleiotropic effects of the Aro-5 mutation in cytochrome expression<sup>46</sup>. Furthermore, although Aro-5 pili sheared from the cells had reduced conductivity<sup>44</sup>, the shearing procedure also releases c-type cytochromes<sup>77</sup>, which could contribute to the measured conductivity<sup>78</sup>. Yet the studies raise the interesting possibility that the conductive properties of the pili influence biofilm conductance.

In this study, I addressed current limitations of genetic studies with pili-deficient mutants and investigated the effect of several pili-inactivating mutations in the expression of cytochromes. One of the mutations, a deletion in the gene encoding the pilin polymerization motor, PilB, inactivated pili expression without affecting cytochrome expression. Hence, I used this mutant to investigate the role of pili in the growth and electrochemical activity of *G. sulfurreducens* biofilms. The genetic studies indicate that the pili are required for optimal growth and current production by the biofilm cells. Electron transfer in thin (ca. 10  $\mu\text{m}$ ) biofilms required the expression of both the pili and the matrix-associated cytochrome OmcZ, suggesting that both components function as charge carriers. Yet to grow thicker biofilms and sustain linear increases of current the biofilm cells require the expression and conductive properties of the pili. Presence of conductive pili confers on *Geobacter* cells a metabolic advantage over other bacteria relying solely on cytochromes or diffusible electron carriers, as it maximizes energy generation through extracellular electron transfer even in cells positioned at tens of micrometer distances from the electrode.

## **2.2 Materials and Methods**

### **2.2.1 Bacterial strains and culture conditions.**

The bacterial strains used in this study are described in (Table 1). The wild-type (WT) strain, *G. sulfurreducens* strain PCA, was kindly provided by Daniel Bond (University of Minnesota) and was used to construct three knock-out mutants: pilB (carrying a deletion in *pilB*, GSU1491), pilA

(carrying a deletion in the pilin gene *pilA*, GSU1496), and *omcZ* (carrying a deletion in *omcZ*, GSU2076). When indicated, the *pilB* mutation was complemented *in trans* by expressing a wild-type copy of *pilB* from the pRG5 plasmid (*pilB*<sup>+</sup> strain). The WT strain was also used to construct the *pilA*-E5A mutant (carrying a single alanine replacement of the glutamic 5 residue in the mature pilin PilA protein) and the Tyr3 mutant (carrying alanine replacements in the pilin's three tyrosine residues Y27, Y32, and Y57). The WT and mutant strains were routinely cultured anaerobically in NBAF, FWAF or DBAF media, which are NB medium<sup>5</sup>, modified freshwater FW medium<sup>13</sup>, and DB medium<sup>51</sup> supplemented with 15 mM (FWAF and NBAF) or 20 mM (DBAF) acetate as the electron donor and 40 mM fumarate as the electron acceptor. Na<sub>2</sub>SeO<sub>4</sub> (1 μM) was also added to NBAF and DBAF media to stimulate growth, as reported elsewhere<sup>122</sup>.

### **2.2.2 DNA manipulations and mutant construction.**

Deletions of the *pilB*, *pilA*, and *omcZ* genes were constructed using the *cre-lox* system<sup>52</sup> with the primers listed in Table 2. The general procedure included the PCR-amplification of the gentamycin (Gm) resistance cassette (*aaaC1*) flanked by *loxP* sites (*Gm-loxP*) from plasmid pCM351<sup>52</sup> using primer set RS21-RS22 and of the upstream/downstream target chromosomal regions using primer sets RS1-RS2/RS3-RS4 (*pilB*), RS5-RS6/RS7-RS8 (*pilA*), and RS9-RS10/RS11-RS12 (*omcZ*). The upstream region of the target gene, the *Gm-loxP* cassette, and the downstream region of each gene were then fused in that order by overlap extension PCR using the corresponding external forward and reverse primers and the Herculase II Fusion DNA Polymerase (Agilent Technologies). PCR conditions for this last amplification step were: 2 min of denaturation at 95°C; 35 cycles of 20 s at 95°C, 25 s at 54°C, and 2 min at 72°C; and a final 3-min extension at 72°C. The PCR products were then separated on an agarose gel, purified using the Zymoclean™ Gel DNA Recovery Kit (Zymo Research), and cloned into the pCR2.1 plasmid (Table 1) using the TOPO® TA Cloning kit (Life Technologies) for sequence

confirmation. The cloned fragments were then PCR-amplified with the external primers and the linear fragment, once purified from an agarose gel, was electroporated into electrocompetent cells of *G. sulfurreducens* by following a previously published procedure<sup>5</sup>. Selection of recombinant strains was performed on NBAF plates supplemented with 5 µg/ml of Gm. When indicated, the Gm cassette carried by the *pilB* mutant was excised from its chromosomal location by expressing the Cre recombinase from plasmid pCM158<sup>123</sup> and selecting for transformants on NBAF plates supplemented with 200 µg/ml of kanamycin. The excision of the marker was confirmed by PCR and the resulting mutant ( $\Delta pilB$ ) was transferred twice in NBAF medium without kanamycin and then plated on NBAF with and without kanamycin to confirm the loss of the plasmid. The  $\Delta pilB$  strain was used to construct the double *pilB gspE*, and *pilB mshE* mutants (Table 1) using the general PCR procedure described above but with primer sets RS9-RS12, RS13-RS16, and RS17-RS20 (Table 2), respectively.

I constructed the *pilA*-E5A and Tyr3 mutants by introducing one (E5A) or three (Y27A Y32A Y57A) alanine replacements, respectively, in targeted codons in the *pilA* gene (GSU1496). The primers used to construct these mutants are listed in Table 2. The general procedure was to PCR-amplify the *pilA* gene and the *pilA* downstream region using primer sets RS23-RS24 and RS25-RS26, respectively, as well as the spectinomycin (Sp) resistance cassette from plasmid pRG5<sup>124</sup> using primer set RS27-RS28. The three fragments were then fused by overlap extension PCR with the external RS23 and RS26 primers to generate a 1684-bp DNA construct (*pilA*-Sp) containing the *pilA* gene, the Sp resistance cassette (*aadA*), and the *pilA* downstream region. The construct was gel purified before cloning it into plasmid pCR®2.1-TOPO® TA vector (Invitrogen™) and introducing targeted nucleotide substitutions in the *pilA* gene using the QuikChange Lightning Site-Directed Mutagenesis kit (Agilent Technologies). The E5A substitution was generated with primers RS29 and RS30. Tyr3 was generated by sequentially introducing Y27A first (RS31-RS32), then Y32A (RS33-RS34) and, lastly, Y57A

(RS35-RS36). The mutated fragments were confirmed by sequencing before PCR-amplification using the external primers, gel purification, and electroporation into electrocompetent cells of *G. sulfurreducens*. Selection of recombinant strains was performed on NBAF plates supplemented with 75 µg/ml of Sp.

### **2.2.3 Microbial electrochemical cells (MECs).**

The growth and electrochemical activity of the WT and mutant biofilms were assayed in H-type MECs equipped with anode and cathode graphite rod electrodes and a 3 M Ag/AgCl reference electrode. The MECs were set up, inoculated with cell suspensions, and operated with a poised anode electrode (0.24 V versus reference electrode) as described previously<sup>122</sup>. The electron donor in the anode chambers was always acetate, provided in 1, 2, or 3 mM concentrations, as indicated. Supernatant samples were periodically removed from the anode medium broth, filtered (0.45 µm), and analyzed by high-performance liquid chromatography (HPLC), as described elsewhere<sup>54</sup>, to monitor electron donor removal. Current production was recorded with a VSP potentiostat (BioLogic). The ability of the cells to grow from the oxidation of acetate coupled to the reduction of the anode electrode was inferred from the rates of linear current increase (mA/day) before maximum current was reached and the deceleration phase in current production was initiated. The exponential phase of current production was also fitted statistically ( $R^2 > 0.98$ ) to an exponential curve and the exponent of the resulting formula was used to estimate the generation times of the anode biofilm cells.

At the end of the MEC experiment, when current had decreased to < 0.1 mA, the anode electrodes were removed from the chamber and the live and dead biofilm cells were differentially stained in green and red, respectively, with the SYTO 9 and propidium iodide dyes of the BacLight™ viability kit (Invitrogen). The anode electrodes with the stained biofilms were then immersed gently in a Lab-Tek® coverglass chamber (Nunc) filled with 3 ml of phosphate

buffered saline and examined using a FluoView FV1000 inverted microscope system (Olympus, Center Valley, PA) equipped with an Olympus UPLFLN 40X oil immersion objective (numerical aperture, 1.30). SYTO 9 was excited at 488 nm and propidium iodide was excited at 543 nm. Vertical 2D-images of the biofilms were collected every 1  $\mu\text{m}$  from approximately 10 random fields (1,024 by 1,024 pixels, 0.31  $\mu\text{m}/\text{pixel}$ ) per electrode, using a minimum of two biological MEC replicates. The biofilm thickness was then manually analyzed by averaging thickness measurements of 5 representative areas per field. When indicated, the COMSTAT software<sup>126</sup> was used to estimate the biofilm biomass based on the fluorescence emitted from the live cells, as described previously<sup>122</sup>.

#### **2.2.4 Static biofilm assays on plastic surfaces.**

When indicated, the biofilm phenotype of the WT and mutant strains was also investigated on plastic surfaces using a soluble electron acceptor (fumarate) essentially as described elsewhere<sup>15</sup>. Briefly, the strains were grown in FW medium with 30 mM acetate and 40 mM fumarate (FWAF) to mid-exponential phase and inoculated to a final OD<sub>600</sub> of 0.02 into 6 replicate wells, each with 150  $\mu\text{l}$  of FWAF, of a 96-well, polystyrene, tissue culture treated plate (Costar™, Corning® Life Sciences). After 48 h of incubation at 30°C, the culture broth was discarded and the biofilms were stained for 30 min with 150  $\mu\text{l}$  of a 0.01% (w/v) aqueous solution of crystal violet. After staining, the biofilms were washed with double distilled H<sub>2</sub>O and dried overnight before resolubilizing the biofilm-associated crystal violet with 33% (v/v) acetic acid. The optical density of the solution was read at 580 nm to estimate the biofilm biomass.

#### **2.2.5 Gene expression analyses by quantitative Real Time-PCR (qRT-PCR).**

The expression of key components of the biofilm matrix (pili, EPS matrix, and matrix-associated c-type cytochromes) was studied by measuring the transcript levels of selected genes by qRT-PCR. The gene targets were the pilin-encoding *pilA* (GSU1496) and its

downstream gene (GSU1497) in the *pilA* operon<sup>34</sup>, the gene encoding the ATP-dependent EPS exporter, *xapD* (GSU1501)<sup>30</sup>, and *omcZ* (GSU2078), which encodes for the precursor of the matrix-associated *c*-type cytochromes OmcZ<sub>S</sub><sup>20</sup>. The constitutive gene *rpoD* (GSU3089) was used as a control. WT, *pilB*, *pilA*, and *pilA*-E5A biofilms were grown for 48 h in the wells of 48-well polystyrene plates containing 600 µl of FWAf before decanting the culture broth and resuspending the biofilm cells in 50% (v/v) of ice-cold methanol to stop transcription. The cell suspensions were centrifuged to isolate the cells as pellets and trizol reagent (Invitrogen) was used to extract their RNA. Treatment of the RNA with RNase-free DNase (Promega) and reverse transcription (RT) with random primers (Promega) using the Super Script® III Reverse Transcriptase (Invitrogen) were carried out following the manufacturer's recommendations. qRT-PCR was performed with the rEVALuation qPCR Master Mix (Syzygy), as recommended by the manufacturer, using the primers listed in Table 2. The comparative C<sub>T</sub> method<sup>127</sup> was used to calculate the relative expression of each gene using *rpoD* constitutive expression as an internal control ( $\Delta C_T$  value or  $C_{T (target)} - C_{T (rpoD)}$ ) for each strain, and the average of the difference between each mutant strain  $\Delta C_T$  and the WT  $\Delta C_T$  was used to calculate the  $\Delta\Delta C_T$ . The relative fold change of expression for each target gene versus the *rpoD* internal control for each mutant strain versus the WT was then calculated with the formula  $2^{-\Delta\Delta C_T}$ .

### **2.2.6 Assays for *c*-type cytochrome content and profiling.**

The total (cells and biofilm matrix) *c*-type cytochrome content of biofilms of the WT, *pilB*, *pilA*, and *pilA*-E5A strains was estimated by redox difference spectroscopy. The biofilms were first grown for 48 h in 96-well plates, as described above for the biofilm assays on plastic surfaces, before discarding the culture broth and freezing the biofilms by storing the plates at -80 °C for a minimum of 24 h. The plates were thawed at room temperature for a minimum of 15 min before suspending the biofilms in FW medium at room temperature. For each strain, I pooled together biofilm samples from 96 wells and adjusted the biofilm suspension to an OD<sub>600</sub>

of 0.2 with FW medium. Sodium dodecyl sulfate (SDS) (final concentration of 0.1% w/v) and fresh 1 mM dithionite were then added to the suspension to lyse the cells and as a reducing agent, respectively. All of the steps were performed anaerobically inside a glove bag (Coy Laboratories). The ultraviolet-visible (UV-Vis) spectrum from 350-650 nm of the reduced biofilm cell extract was then collected before and after oxidation with 2 mM ferricyanide using a Shimadzu UV-2401 spectrophotometer. The difference between the reduced and oxidized spectra at 552 nm (the  $\alpha$  Soret band in the reduced state) of the biofilm cell extracts in the WT and pili-deficient mutants (pilB, pilA, and pilA-E5A) was used to estimate the overall biofilm c-type cytochromes content (cells and biofilm matrix)<sup>56</sup>. Spectra were also collected from cell extracts obtained from planktonic cells harvested from exponential (OD<sub>600</sub>. 0.4-0.5) cultures grown in FWAf at 30°C. The total heme content of the cells was analyzed using the alkaline pyridine hemochrome method as described previously<sup>129</sup>.

Proteins in the biofilm matrix in the WT and pili-deficient strains were also isolated using the procedure described by Rollefson *et al.*<sup>30</sup> and modified by Cologgi *et al.*<sup>15</sup>. The matrix-associate proteins were separated electrophoretically by SDS-PAGE as previously described<sup>30</sup> except that samples were loaded onto 12% Mini-Protean TGX gels (Bio-Rad) and Novex Sharp molecular weight markers (Invitrogen) were used as standards. Heme-containing protein bands were stained with 3,3',5,5'-tetramethylbenzidine (TMBZ), as previously described<sup>130</sup>. Replicate gels were run and stained with Coomassie Blue to ensure that the total protein content per lane was comparable. When indicated, SDS-PAGE and heme-staining were also used to profile all heme-containing proteins within planktonic cells grown in FWAf to mid-exponential phase, as reported elsewhere<sup>130</sup>.

### **2.2.7 Pili purification and conductivity measurements by CP-AFM.**

Pili from WT or the Tyr3 mutant strain of *G. sulfurreducens* were purified as SDS-insoluble fractions by preparative electrophoresis, as previously described<sup>13</sup> except that all

buffers contained 1 mM ethylenediaminetetraacetic acid (EDTA) and all drying steps were carried out under a constant flow of filter-sterilized (0.22  $\mu\text{m}$ )  $\text{N}_2$  gas. The pili were deposited on the surface of freshly cleaved highly oriented pyrolytic graphite (HOPG) for 30 min, then blotted dry, before probing their transversal conductivity by Conductive Probe-Atomic Force Microscopy (CP-AFM). The samples were scanned with the AFM tip in tapping mode to image the pili and to identify individual fibers. The CP-AFM tip was then positioned at different points along each pilus filament to measure its transversal conductivity while applying a bias voltage within the  $\pm 1$  V range (3 nN force, 1 Hz rate). Two to three current-voltage ( $I$ - $V$ ) curves were collected from each of at least three positions along each pilus filament and four to five pilus fibers were probed for each strain to account for technical and biological replication. During the measurements, the tip was periodically moved to the HOPG surface adjacent to the pili to control tip quality. The resistance ( $R$ ) values were calculated from the inverse of the linear portion of each  $I$ - $V$  curve and averaged for each strain (WT and Tyr3).

## **2.3 Results**

### **2.3.1 Inactivation of the *PilB* assembly motor does not affect *c*-type cytochromes expression.**

The assembly of type IVa pili on the bacterial inner membrane is mediated by a protein apparatus involving three interacting subcomplexes: the pilus subcomplex (major pilin and minor pilins, if present), the motor subcomplex (containing several proteins, including the PilB and PilT ATPases that power pilus polymerization and retraction, respectively), and the alignment subcomplex (which properly aligns the assembled pilus through the outer membrane PilQF secretin complex)<sup>131</sup>. As mutations that render the pilus and motor subcomplexes inoperative also prevent pili expression<sup>131</sup>, I constructed mutants of *G. sulfurreducens* carrying deletions in the genes encoding the PilA pilin subunit (pilA mutant) and the PilB ATPase (pilB mutant),

respectively. Additionally, I constructed a pili-deficient mutant (*pilA-E5A*) carrying an alanine substitution in the conserved E5 amino acid required for proper alignment and assembly of pilins<sup>52,66</sup>.

Two of the pili-inactivating mutations, *pilA* and *pilA-E5A*, had pleiotropic effects in cytochrome expression. Differential redox spectroscopy of reduced-minus-oxidized UV-VIS spectra (Figure 6) revealed, for example, an increased expression of *c*-type cytochromes in the *pilA* and *pilA-E5A* biofilms compared to the WT biofilm (Figure 9 A). Similar increases were observed in planktonic cells of the *pilA* and *pilA-E5A* strains (Figure 7), ruling out any influence of the physiological state of the cells (planktonic or biofilm) in the phenotype. Some of the pleiotropic effects observed in these mutants were transcriptional in nature. For example, transcripts levels for the gene encoding the outer membrane *c*-type cytochromes OmcB were up-regulated in the *pilA* and *pilA-E5A* mutants (Figure 8). On the other hand, other pleiotropic effects were post-transcriptional. Transcripts for the matrix-associated cytochrome OmcZ were, for example, similar in the WT and the *pilA* and *pilA-E5A* mutants (Figure 8). Yet the small (~30-kDa), processed OmcZ<sub>s</sub> cytochrome that is released into the biofilm matrix<sup>30</sup> and is required for optimal biofilm electroactivity<sup>15,119</sup> was absent in the matrix of *pilA* and *pilA-E5A* biofilms (Figure 9). Interestingly, OmcZ<sub>s</sub> was detected in heme-stained preparations of planktonic cells (Figure 7), suggesting that the OmcZ<sub>s</sub> defect of the *pilA* and *pilA-E5A* mutant biofilms was related to the unique physiology of cells living within a surface-attached community.

The *xapD* gene, which encodes an ATP-dependent exporter required for the synthesis of the biofilm EPS matrix that anchors *c*-type cytochromes<sup>30</sup>, was also transcriptionally up-regulated in the *pilA* and *pilA-E5A* mutants (Figure 8). These mutants also formed dense biofilms on plastic surfaces under static conditions (Figure 9), a phenotype that has been linked to the overproduction of the biofilm EPS<sup>132</sup>.

In contrast with the pleiotropic nature of the *pilA* and *pilA-E5A* mutations, inactivation of the PilB motor to prevent pilin assembly had no effect on the overall *c*-type cytochromes content of the biofilms (Figure 9). Moreover, the mutation did not affect the transcription of the two genes of the pilin operon (*pilA* and GSU1497) or the genes encoding the outer membrane *c*-type cytochromes *omcB* and *omcZ* (Figure 8). The expression of OmcZ<sub>s</sub> in the *pilB* biofilm matrix was also unaffected (Figure 9). The synthesis of the biofilm EPS was not affected in the *pilB* mutant biofilms either, as *xapD* transcript levels were similar to those in WT biofilms (Figure 8). The pili deficiency of the *pilB* mutant also prevented the formation of dense biofilms on plastic surfaces but the biofilm defect was rescued in the genetically-complemented *pilB*<sup>+</sup> strain, which restored pili production through the expression of the *pilB* gene *in trans* from a medium-copy plasmid (Figure 9). Hence, the *pilB* strain provides the elusive genetic tool needed to assess the contribution of *Geobacter* conductive pili in the growth and electroactivity of anode biofilms.

### **2.3.2 Pili expression is required for optimal electrochemical activity of thin biofilms.**

I investigated the ability of the *pilB* mutant to generate current in an MEC containing 1 mM acetate in reference to the WT strain. Under these conditions, the WT biofilms grew reproducibly to a thickness (ca. 10 μm) that is not predicted to limit electron transfer to the electrode surface via *c*-type cytochromes<sup>37–39,133–135</sup>. As a control, I also constructed a null *omcZ* mutant (*omcZ*), which cannot produce the matrix-associated cytochrome OmcZ<sub>s</sub> required for electron transport to the underlying electrode<sup>119</sup>. Maximum current in the *pilA* and *pilA-E5A* mutant biofilms, which lack both pili and OmcZ<sub>s</sub> (Figure 10), was low (0.08 ± 0.05 and 0.14 ± 0.08 mA, respectively, for duplicate MECs) and required prolonged incubations to oxidize all the acetate in the anode chamber (Figure 10). The phenotype was similar to the *omcZ* control biofilms, which also produced low levels of current (0.11 ± 0.07 mA for duplicate MECs) and required lengthy incubation times (Figure 10). The defect of the *pilA* and *pilA-E5A* mutants in the

MECs cannot be attributed to a reduced number of cells growing on the electrode, because the biofilms eventually reached WT thickness (ca.  $13.5 \pm 3.5$  and  $11.6 \pm 1.9$   $\mu\text{m}$  respectively, for duplicate MECs), they just grew slower. Hence, the results indicate that the inability of the *pilA* and *pilA-E5A* mutant biofilms to produce pili and the matrix-associated OmcZ<sub>s</sub> c-type cytochromes limited their electroactivity.

The *pilB* mutant, which has WT levels of c-type cytochromes and expresses OmcZ<sub>s</sub> in the biofilm matrix (Figure 9) grew biofilms on the anode electrode with WT thickness ( $9.6 \pm 1.4$   $\mu\text{m}$  for triplicate MECs). However, the maximum current harnessed from the anode biofilms was approximately half of that measured in the WT biofilms (Figure 10). Such low levels of current are still significantly higher than those measured in the other pili-deficient mutant strains *pilA* and *pilA-E5A*, which, in addition to the pili deficiency, failed to express OmcZ<sub>s</sub> in the biofilm matrix (Figure 9). The partial restoration of biofilm electroactivity in *pilB* did not result from functional complementation of the *pilB* mutation by functionally homologous genes, because deletion of the two *pilB* homologues of *G. sulfurreducens* (*mshE* and *gspE*, encoding putative ATPase motors of type II secretion systems) generated double mutants that were phenotypically indistinguishable from the *pilB* single mutant (Figure 10 inset). Hence, the *pilB* mutant phenotype is consistent with reductions in biofilm electroactivity caused by the inability of the mutant cells to assemble the pili. It is interesting to note that the pili defect of the *pilB* mutant could not be complemented by the co-inoculation of *omcZ* with *pilB* mutant cells (Figure 10 inset). I did observe a delay in electrode colonization in the co-culture-driven MECs, which was similar to the delay experienced by single mutants that failed to express OmcZ<sub>s</sub> (*omcZ*, *pilA* and *pilA-E5A*) (Figure 10). However, once the electrode was colonized, the biofilms produced current similarly to the *pilB* single mutant. Hence, the results suggest that biofilm cells need to express both pili and OmcZ<sub>s</sub> for optimal biofilm growth and electroactivity.

In addition to a 2-fold reduction in current maxima, the rates of current increase, which correlate well with the rates of exponential growth of the biofilm cells on the anode<sup>136</sup>, measured in the MECs driven by the pilB mutant were reduced in half ( $0.61 \pm 0.15$  mA/d) compared to the WT biofilms ( $1.45 \pm 0.06$  mA/d). Coulombic efficiencies in the pilB-driven MECs ( $96.6 \pm 3.1$ ) were similar to the WT ( $94.6 \pm 4.1$ ), indicating that, on average, the pilB biofilms converted the same amount of acetate to electricity as the WT biofilms, they just did so at slower rates. The pilB defects cannot be attributed to a reduction in the number of cells actively contributing to electron transfer or structural variations of the biofilms either. Confocal micrographs of WT and pilB biofilms collected at the end of the experiment, when all of the acetate had been depleted, and stained with fluorescent viability dyes showed predominantly live cells and similar biofilm structure (Figure 10). Furthermore, the biofilm biomass estimated from the fluorescence emitted by the biofilm cells was similar in both strains ( $10.05 \pm 1.00$  in WT and  $9.06 \pm 1.46$   $\mu\text{m}^3/\mu\text{m}^2$  in pilB). The pilB phenotypes are therefore consistent with reductions in the respiratory rate of individual cells, which is expected in a mutant with defects in extracellular electron transfer.

### **2.3.3 The expression and conductivity of the pili are required to grow thick biofilms.**

The genetic and MEC data presented thus far indicate that optimal electroactivity of thin (ca. 10- $\mu\text{m}$ ) biofilms of *G. sulfurreducens* requires both the matrix-associated c-type cytochromes OmcZ<sub>s</sub> and the pili. As the biofilms grow thicker, cytochromes become progressively reduced and unable to accept electrons from cells in the distal layers. To test if the pili could be the charge carriers in this distal biofilm stratum, I grew the pilB mutant in MECs fed with 2 and 3 mM acetate, which are concentrations of electron donor that support the growth of thicker (ca. 15 and 20  $\mu\text{m}$ , respectively) WT biofilms (Figure 11). In contrast to the linear increases in biofilm thickness observed in the WT-driven MECs as a function of acetate concentration, the pilB biofilms remained thin (ca. 10  $\mu\text{m}$ ) under all the conditions tested (Figure

11). Furthermore, whereas the rates of current increase during the linear phase of current production and current maxima increased proportionally to acetate availability in the WT MECs, they were unaffected in the pilB MECs (Figure 11).

To rule out a structural role for the pili, where their absence could have prevented the pilB biofilms from growing beyond 10  $\mu\text{m}$ , I constructed a mutant strain (Tyr3) that produced pili carrying alanine replacements in the pilin's three tyrosines (Y27, Y32, and Y57). The tyrosine residues are predicted by *ab initio* calculations to contribute greatly to the unique electronic structure and low electron band gap of the pilin without interfering with pilin assembly<sup>45</sup>. Furthermore, the structure of the pilus fiber revealed in molecular dynamics simulations supports a model of multistep hopping involving tyrosines<sup>137</sup>. Supporting this model, the Tyr3 mutant produced pili at WT levels (Figure 12) and formed biofilms as dense as the WT on plastic surfaces (Figure 12) which are conditions that only require pili expression to provide structural support to grow multilayered biofilms<sup>32</sup>. However, pili purified from the Tyr3 mutant were poorly conductive, having more than 5-fold greater resistance to the passage of electrons than the WT pili (Figure 12). The reduced conductivity of the Tyr3 pili also reduced the electroactivity of the Tyr3 anode biofilms in MECs fed with 3 mM acetate and prevented the growth of the biofilms beyond the threshold 10  $\mu\text{m}$  thickness, as observed in the pili-deficient strain pilB (Figure 11). Hence, the conductive properties of the pili, rather than their expression to provide structural support, are required to build thick (> 10  $\mu\text{m}$ ) biofilms and maintain optimal biofilm electroactivity in the distal biofilm layers where the cytochrome pathway is inoperative. Hence, the results support the notion that the pili function as electronic conduits in the upper biofilm strata of thick biofilms as well.

## 2.4 Discussion

The studies described herein provide the elusive genetic evidence supporting the role of *Geobacter* pili as electronic conduits in electroactive biofilms, but also reveal novel insights into how *Geobacter* cells coordinately export *c*-type cytochromes and assemble pili in the biofilm matrix to establish an electronic network that maximizes long-range electron transfer. Part of the difficulty in interpreting earlier genetic studies of pili function<sup>31,34,77</sup> stemmed from the pleiotropic effects that mutations in pilin expression have in *c*-type cytochromes required for optimal extracellular electron transfer<sup>13,15</sup>. Supporting these findings, I show that mutations in the pilin gene (*pilA* and *pilA-E5A*) have numerous pleiotropic effects in cytochrome expression and that such effects are likely exerted through diverse regulatory mechanisms, both transcriptional and post-transcriptional. Furthermore, as observed in other bacteria<sup>138,139</sup>, the pilin gene mutations were epistatic to EPS synthesis, at least at the transcriptional level. By contrast, inactivation of the gene encoding PilB, the ATPase that powers pilin assembly, prevented pili formation without disrupting the expression of other components of the biofilm matrix (*c*-type cytochromes and EPS). The lack of multiple phenotypes in the *pilB* mutant contrasted with those observed in the *pilA* or *pilA-E5A* strains and adds to the growing body of evidence indicating that type IV pili play multiple roles in bacteria. In *Pseudomonas aeruginosa*, for example, the PilA pilin<sup>140</sup>, but not the pilin assembly motor PilB<sup>141</sup>, is essential for efficient protein secretion. This is because PilA, in addition to functioning as the structural subunit of the pilus fiber, also interacts with components of the general secretion pathway to promote the export of proteins across the outer membrane<sup>140</sup>. As a result, mutations that inactivate PilA in this bacterium also affect the secretion of numerous proteins and lead to mutant strains with multiple phenotypes. By contrast, the function of PilB is restricted to pilus biogenesis, and strains of *P. aeruginosa* carrying inactivating mutations in *pilB* do not display export defects<sup>141</sup>. Interestingly, the PilA pilin protein of *G. sulfurreducens* is translated as both short and long prepilin isoforms<sup>142</sup>. Interactions

between the two isoforms promote the processing of the short pilin and its assembly to form the conductive pilus fiber but also influence the secretion and localization of *c*-type cytochromes, such as OmcZ, to the outer-membrane<sup>142</sup>. Hence, pilin-inactivating mutations such as *pilA* and *pilA-E5A* likely interfere with the pilin's role in secretion, thus causing defects in cytochrome expression and localization. However, as in *P. aeruginosa*<sup>141</sup>, the PilB motor of *G. sulfurreducens* is only involved in pilus formation. Hence, inactivating *pilB* prevents pilin assembly and has no effect in the secretion and processing of other biofilm components such matrix-associated *c*-type cytochromes.

The clean phenotype of the *pilB* mutant provided the elusive genetic tool needed to investigate the role of pili as biofilm electronic conduits and to study the interactions between pili and cytochrome electron carriers in electroactive biofilms. By controlling the amount of electron donor added to the anode chamber of the MECs (1, 2, or 3 mM acetate), I restricted the growth of the anode WT biofilms to *ca.* 10, 15, and 20  $\mu\text{m}$  and was able to study the contribution of the pili to the biofilm electroactivity in multilayered communities where all of the biofilm cytochromes are predicted to function as electron carriers (10- $\mu\text{m}$  thick biofilms) or become progressively reduced in the distal biofilm layers (15- and 20- $\mu\text{m}$  thick biofilms). The electroactivity of thin (*ca.* 10  $\mu\text{m}$ ) biofilms of the *pilB* mutant was reduced approximately in half, as indicated by the 2-fold reductions measured in the rates of current production and the maximum current by *pilB* biofilms grown in MECs fed with 1 mM acetate (Figure 9). Such defects cannot be attributed to decreases in the number of biofilm cells contributing to electron transfer, because the thickness and the number of viable cells in the *pilB* biofilms were comparable to the WT. Hence, even in thin biofilms, where the efficiency of the cytochrome pathway is not distance-limited, pili expression is required for optimal electroactivity. Furthermore, biofilms permeated by the poorly conductive Tyr3 pili remained thin and were phenotypically indistinguishable from the pili-deficient *pilB* biofilms, producing current at rates half of those measured in WT biofilms as well

(Figure 12). Hence, even with a structural network of pili, the electroactivity of Tyr3 biofilms was limited by the pili's reduced conductivity. The results therefore argue against the model that the pili's role is restricted to providing structural support needed for cytochrome organization<sup>42</sup>. Rather, the genetic evidence indicated that the pili and cytochrome electronic pathways may work coordinately in thin biofilms.

Our results also add to the growing evidence that OmcZ<sub>s</sub>, the processed and predominant extracellular form of the outer membrane c-type cytochromes OmcZ<sup>20</sup>, is essential for optimal electron transfer across anode biofilms. Pili-deficient strains (pilA and pilA-E5A) with OmcZ<sub>s</sub> defects had a more pronounced defect in current production than the pilB strain (Figure 10), whose EPS matrix contains OmcZ<sub>s</sub> (Figure 9). Furthermore, the defect of the pilA and pilA-E5A strains was similar to the omcZ strain, which carries a deletion in the *omcZ* gene that prevents it from expressing the cytochrome. Given the preferential localization of OmcZ<sub>s</sub> in the biofilm stratum closer to the anode electrode<sup>36</sup> and the dramatic effect of inactivation of the *omcZ* gene on the growth and electroactivity of the anode biofilm<sup>119</sup>, it is likely that OmcZ<sub>s</sub> is the primary electron carrier of the cytochrome pathway in the regions of the biofilm matrix closer to the electrode.

While it was possible to grow thicker (ca. 15 and 20 μm) WT biofilms, preventing the assembly of the pilins (pilB mutant) or reducing the conductivity of the assembled pili (Tyr3 mutant) effectively prevented the biofilms from growing more than 10 μm away from the electrode (Figure 12). Hence, the expression and conductive properties of the pili are required to maintain optimal electrical connectivity as the biofilms grow in thickness and electron transfer via the cytochrome pathway becomes limited<sup>38,39</sup>. The fact that cytochromes in the upper biofilm strata remain reduced even when a positive voltage is applied to the biofilm<sup>38</sup>, suggests that they do not have a primary role as electron carriers in these regions. Paradoxically, these are also the regions where electron donor (acetate) availability is highest<sup>40</sup>. Studies show that *G.*

*sulfurreducens* can continue to metabolize acetate in the absence of an electron acceptor by overexpressing its extracytoplasmic c-type cytochromes and using them as a capacitor to store up to  $10^6$  electrons per cell<sup>143</sup>. In support of this, the expression of the outer membrane c-type cytochromes OmcB is transcriptionally up-regulated under conditions of electron acceptor limitation<sup>144</sup> and levels of OmcB protein increase in biofilm cells located more than 10  $\mu\text{m}$  from the electrode<sup>54</sup>. The capacitor role of cytochromes in these upper biofilm regions could allow cells to continue to metabolize acetate and generate a proton motive force for energy generation. The pilus apparatus is anchored in the cell envelope of Gram-negative bacteria; hence, it could potentially accept electrons from the extracytoplasmic cytochromes, promoting their discharge from the cell to the biofilm matrix. Furthermore, pili can grow several  $\mu\text{m}$  in length and intertwine to form a complex web of nanowires that could electronically connect the strata of the biofilm distal and proximal to the electrode, effectively bypassing the limitation of the cytochrome pathway in the electron acceptor-limited regions. This pili network may also be required as cytochrome electron acceptors in the distal strata of a biofilm; as the observed electron gradient leads these cytochromes to constantly be in a reduced state, making diffusion based mechanisms too slow to support growth

Taken together, the results support a model of mechanism-based stratification in electroactive biofilms. The pili electronic network is essential for charge transport in all the biofilm strata, working coordinately with the matrix-associated cytochrome carriers to transfer electrons in the stratum closest to the electrode. It has been previously proposed that electron transfer across electroactive biofilms may require the expression of both cytochromes and pili to promote short-distance, electron transfer reactions<sup>146</sup>. For example, electron transfer out of a pilus (i.e. pili-to-pili or pili-to-electron acceptor) may be facilitated by cytochromes bound to the pilus fibers<sup>42</sup>. Of note, no additional cytochromes are currently known to be necessary for

efficient current production, and it is unknown what role, if any, the cytochromes play in the distal strata.

As the biofilm thickness increases, a pH gradient is established whereby the pH is lower in the regions closer to the anode<sup>147</sup>. The accumulation of protons in the regions of the biofilms proximal to the electrode could limit the efficiency of the pili pathway locally if proton-coupled electron transfer (PCET) reactions influence pilus conductivity, as previously shown for other proteins relying on tyrosines for electron transfer<sup>148</sup> and proposed for the *Geobacter* pili<sup>137</sup>. In PCET, tyrosine residues simultaneously transfer a proton and an electron, thus lowering the amino acid's oxidation potential to the low potentials required for electron transfer in biological systems<sup>92</sup>. Thus, the efficiency of the pili pathway and its electronic interactions with cytochromes may be influenced by the local pH. Nutrient gradients also form in thick biofilms, which can influence the cell physiology, the expression of biofilm components, and the biofilm electroactivity<sup>37,134</sup>. Such regulatory networks may be responsive to more than one biofilm parameter, such as pH, nutrient availability, and redox potential, allowing cells to control the composition of the biofilm electron carriers to maximize the rates of electron transfer. Biofilms of oxygen-respiring bacteria are, for example, responsive to redox potentials and use redox cues from their microenvironment to alter the biofilm structure, maximize O<sub>2</sub> diffusion, and maintain redox homeostasis<sup>149</sup>. Similar mechanisms could control the expression of cytochromes and pili to facilitate their coordinated interactions and redox homeostasis in *G. sulfurreducens* biofilms. Thus, understanding the multiple functions that pili play in *G. sulfurreducens* and their regulation may prove instrumental to improve the performance of *Geobacter*-driven electrochemical systems for applications in bioenergy.

**CHAPTER 3. SITE-DIRECTED MUTAGENESIS REVEALS THE ROLE OF AROMATIC  
AMINO ACIDS AND LOCAL ELECTROSTATICS IN PILUS CONDUCTIVITY AND  
EXTRACELLULAR ELECTRON TRANSFER**

Parts of this chapter were published previously and have been reprinted with permission.

Copyright © Royal Society of Chemistry, Feliciano, G. T., Steidl, R. J. & Reguera, G. Structural and functional insights into the conductive pili of *Geobacter sulfurreducens* revealed in molecular dynamics simulations. *Phys. Chem. Chem. Phys.* **17**, 22217–22226 (2015).

Reguera, G., R. Steidl, Microbial nanowires. U.S. Patent Application Serial No. 13/221,495, filed August 30, 2011, claiming priority to U.S. Provisional Patent Application Serial No. 61/378,188, filed on August 30, 2010.

### 3.1 Introduction

In Chapter 2 I demonstrated that the conductive pili of *Geobacter sulfurreducens* are required for the efficient electron transfer (ET) through anode biofilms in a microbial electrochemical cell (MEC). Furthermore, I also demonstrated that removing the pilin's three tyrosines (Tyr3 mutant) reduced the pilus conductivity and electrochemical activity of the anode biofilms. In this chapter, I focused on gaining insights into the role of tyrosines in these functions and, more generally, about the role of pili as electronic conduits in the biofilms. It has been proposed that electron transfer across anode biofilms has metallic features and these properties are due to the intrinsic metallic-like conductance of the pili<sup>77</sup>. The metallic model of pilus conductance relies heavily on the assumption that aromatic amino acid residues of the pilin cluster together in the pilus fiber promoting  $\pi$ -stacking and metallic regimes<sup>77</sup>. As I describe in this chapter, this type of stacking requires very short inter-aromatic distances and specific (sandwich type) aromatic dimer configurations. Such geometric configurations are rare in proteins compared to the parallel-displaced or T-shaped ring conformations, which are prevalent in proteins due to their superior stability<sup>150</sup>.

Charge transfer in proteins is only known to proceed via two mechanisms: tunneling and hopping<sup>85,151</sup>. In tunneling, electrons travel through the medium (e.g., the proteins matrix) from donor to acceptor without residing in relay stations. As a result, tunneling rates are inversely and exponentially proportional to the distance the electron travels and become too slow to be biologically relevant at distances greater than 20 Å<sup>84,86</sup>. Electron hopping, on the other hand, is the sequential transfer of charges in various steps using intermediates such as redox active amino acids and cofactors, which act as relay stations<sup>151</sup>. As a result, this mechanism of ET is faster than tunneling over longer distances (ca. 25 Å) and is only weakly dependent on distance<sup>151</sup>.

As the pili are often several micrometers long, tunneling alone cannot explain why the *G. sulfurreducens* pilus transport charges. Long-range charge hopping, on the other hand, is possible if amino acids with oxidizable side chains are clustered sufficiently in the pilus so as to maintain side chain distances (ca. 25 Å) that permit successive short and fast electron transfer steps<sup>152</sup>. The hopping of electrons in proteins is mediated by redox-active amino acids such as tryptophan, tyrosine, and cysteine, which function as relay stations or “stepping stones” in the ET pathways<sup>92,153,154</sup>. The *G. sulfurreducens* pilin does not contain any tryptophans, cysteines, or methionines but does have three tyrosines (Figure 2). Multistep hopping via tyrosines has been demonstrated in some well-studied protein systems such as ribonucleotide reductase<sup>96</sup> and photosystem II<sup>155</sup>. In these systems, electron transfer via tyrosines is coupled to the transfer of the tyrosine’s hydroxyl proton to a nearby negatively-charged residue (thus, it is a proton-coupled electron transfer). The transfer of a proton decreases the reduction potential of the tyrosine and facilitates electron transfer at the low potentials that operate in biological systems<sup>92</sup>.

The pilin also has three phenylalanines (Figure 2). Phenylalanines have too high a redox potential to be oxidized during multistep hopping. However, the presence of phenylalanine residues in several cytochrome c proteins increases the ET rates compared to those without phenylalanines<sup>100,101</sup>. Electronic structure calculations also predicted the conserved phenylalanine residues of bacterial NADH:ubiquinone oxidoreductase to be involved in electron transfer<sup>102</sup>. One phenylalanine in particular, F328, was involved in all fast paths of electron transfer calculated in the analyses. Although the exact mechanism of ET mediated by phenylalanines *in vivo* is not fully understood, studies with small peptides have demonstrated that phenylalanines act as an electron “stepping stone” in the ET pathway and are required for optimal ET rates<sup>103</sup>.

In addition to specific amino acids in proteins acting as sites of electron hopping, peptide studies have demonstrated that charge transfer via hopping can happen along the amide groups of the peptide backbone particularly in helical peptides<sup>156</sup>. Charge hopping by the amide groups is theorized to involve hole-hopping as opposed to electron hopping, meaning the electron first hops to the acceptor and then the “hole” left by the lack of an electron is filled by an electron from another amide group. In these peptide systems, electrons hopped along lengths significantly longer than the *G. sulfurreducens* pilin peptide<sup>68,88</sup>. The rate of charge transfer via this backbone hopping method is increased by the natural dipole moment of the helical peptide<sup>67,108,109</sup>, from positive N-terminus to negative C-terminus. The natural dipole of *G. sulfurreducens* pilin is accentuated due to the placement of acidic and basic residues (Figure 2). Hydrogen bonding naturally present in  $\alpha$ -helices (Figure 5) is also thought to increase ET through the peptide<sup>112,113</sup>. Furthermore, the movement and flexibility of organic structures, such as DNA and peptides, is predicted to increase polymer charge transfer rates<sup>115,116,157,158</sup>.

As a first step in understanding how electrons move through the pilus and what amino acids could be implicated, we first sought to construct a high resolution structural model of the pilus fiber. The model would not only identify residues that may be involved in ET, but could also predict the distances and orientations of these amino acid residues. Thus it can both predict the potential for those amino acids to participate in multistep hopping and discern whether the residues are aligned and clustered to promote metallic regimes. As with other insoluble peptide assemblies such as amyloid fibers, atomic resolution structures of pili are difficult to attain because of the difficulty in preparing suitable crystals or applying liquid-state NMR. To date, the only published pseudoatomic model of a type IV pilus is that of *N. gonorrhoea* (gonococcus or GC)<sup>66</sup>. This model was derived from cryo-EM data of the pilus fibers with a 12.5 Å resolution, which was used as a template to superimpose the crystal structure of the GC pilin. Similar approaches were used to construct three different homology models of the *G. sulfurreducens*

pilus fiber<sup>58,79,83</sup>. However, there are many discrepancies in the predictions inferred from these models, which likely reflect differences in the structural assumptions used to construct them. The first homology model, for example, superimposed a computational homology model of the *G. sulfurreducens* pilin or PilA onto the GC pilus template and reported the clustering of aromatic amino acids of the pilin within a 15-21 Å range<sup>83</sup>. These inter-aromatic residue distances are still optimal for charge hopping, but are too large to promote the  $\pi$ -stacking required for metallic conductance. A second model also used the GC pilus template, but inserted an atomic resolution NMR structure of the *G. sulfurreducens* pilin<sup>58</sup>. This approach generated a structural model in which the aromatic residues clustered as 15 Å-wide bands along the pili, which were separated by aromatic ring-free regions. The model fails to explain how charges would move from one aromatic ring-dense band to another. A third homology model used the *G. sulfurreducens* NMR pilin model, but superimposed the structure into computationally generated *P. aeruginosa* or PAK pilus fiber template, which was inferred from diffraction data for the pilus<sup>50</sup>. This study reported a path of aromatic residues 3-4 Å apart from each other, which are inter-aromatic residue distances that could support metallic conductance. However, the aromatic ring residues are not face-centered (sandwich conformation), which is required for metallic regimes to operate. Furthermore, some of the reported 3-4 Å distances involved the peptide backbone rather than the aromatic ring itself. Other deficiencies were noted in this homology model, particularly the fact that the phenylalanine F1 is bonded to the F24 of an adjacent pilin in the lower portion of the pilus fiber. Inter-aromatic residue distances in the upper portion of the fiber, where the F1-F24 bond is not present, exceed 3-4 Å.

Key to constructing a reliable homology model is to minimize the number of structural assumptions by using experimentally validated structures for both the pilin and the pilus fiber used as template. To date, the only validated structures are the NMR-derived structural model of the pilin resolved in lipid micelles<sup>58</sup> and the GC pilus structure derived from cryo-EM data<sup>66</sup>.

Our collaborator Dr. Gustavo Feliciano used molecular dynamics (MD) to optimize the NMR pilin structure in solution and superimpose it into the GC pilus template. This allowed him to generate a homology model of the *G. sulfurreducens* pilus with minimal structural assumptions. He then improved the accuracy of the homology model by refining it to higher resolution in MD simulations<sup>137</sup>. My role in this project was to test the model predictions by introducing targeted amino acid replacements in residues of the pilin predicted to have a direct role in electron transfer (tyrosines) and those influencing the electrostatic environment around the tyrosines (charged amino acids), which can affect the redox potential, configuration and distances of the aromatic residues and, indirectly, the rates of electron transfer. I also performed independent analyses of the model to interpret the phenotypes of some pilin mutants and develop a model for ET along the pilus and to external electron acceptors such as insoluble Fe(III) oxides or the soluble uranyl cation. When indicated, I worked with other members of the Reguera lab (Dr. Sanela Lampa-Pastirk and Krista Cosert) to measure the conductivity of purified pili carrying selected mutations.

## **3.2 Materials and Methods**

### **3.2.1 Growth conditions**

The bacterial strains used in this study are described in Table 3. The wild-type (WT) strain, *G. sulfurreducens* strain PCA, was kindly provided by Daniel Bond (University of Minnesota) and was used to construct the amino acid replacement mutants. To distinguish this strain from the laboratory strain routinely used by other members of my lab, I designated it strain DB (for Daniel Bond). The WT and mutant strains were routinely cultured anaerobically in NBAF, FWAF or DBAF media, which are NB medium<sup>5</sup>, modified freshwater (FW) medium<sup>13</sup>, and DB medium<sup>122</sup> supplemented with 15 mM (FWAF and NBAF) or 20 mM (DBAF) acetate as the electron donor

and 40 mM fumarate as the electron acceptor.  $\text{Na}_2\text{SeO}_4$  (1  $\mu\text{M}$ ) was also added to NBAF and DBAF media to stimulate growth, as reported elsewhere<sup>122</sup>.

### **3.2.2 Mutant construction**

I constructed the amino acid replacement mutants by introducing alanine or phenylalanine replacements in targeted codons in the *pilA* gene (GSU1496). The primers used to construct these mutants are listed in Table 4. Amino acid replacements were generated by introducing targeted nucleotide substitutions in the *pilA* gene using the QuikChange Lightning Site-Directed Mutagenesis kit (Agilent Technologies) and the appropriate primers (and pCR2.1-*pilASpec*, as described in Chapter 2). The mutated fragments were confirmed by sequencing before PCR-amplification using the external primers, gel purification, and electroporation into electrocompetent cells of *G. sulfurreducens*. Selection of recombinant strains was performed on NBAF plates supplemented with 75  $\mu\text{g}/\text{ml}$  of spectinomycin.

### **3.2.3 Pili purification and conductivity analyses.**

Pili from the WT or the Y27A mutant strains of *G. sulfurreducens* were purified to homogeneity as previously described<sup>13</sup>, except that all the buffers used during the purification contained 1 mM ethylenediaminetetraacetic acid (EDTA) and all drying steps were carried out with a constant flow of filter-sterilized  $\text{N}_2$  gas, rather than in a SpeedVac, to prevent contamination. Samples were stored on ice for short-term use or flash frozen in liquid nitrogen and stored at  $-80^\circ\text{C}$  for long-term use.

The transversal conductivity of purified pili deposited on graphite was measured with a conductive probe-atomic force microscope (CP-AFM), as described in Chapter 2. When indicated, charge transport along pili purified from the WT and a Y27A mutant was also measured by Dr. Sanela Lampa-Pastirk. For these experiments, pili were deposited on patterned gold electrodes nanofabricated onto a silicon chip by Dr. Lampa-Pastirk, as described

elsewhere<sup>159</sup>. After pili deposition, the electrodes were stored in an air-tight container under a flow of N<sub>2</sub> gas for 1 h and immediately probed for axial conductivity.

CP-AFM was performed with Ti/Ir-coated silicon cantilevers having a nominal spring constant 2 N/m (ASYELEC-01, Asylum Research) and using a Cypher scanning probe microscope (Asylum Research). Pilus fibers lying across the gold-SiO<sub>2</sub> interface were first identified in non-contact amplitude modulation (tapping or AC) imaging mode and then probed with the conductive tip (3 nN force, 1 Hz rate) at different points along the pilus fiber starting at regions further apart from the electrode to those closest. The region of the pilus in direct physical contact with gold (designated as 0 nm) was also probed as well as positive (bare gold) and negative (SiO<sub>2</sub> substrate) controls. The resistance ( $R$ ) at each position along the pilus fibers was calculated from the inverse slope of the regression line that fit the portion of the  $I$ - $V$  curve exhibiting the most significant ohmic dependence of current on voltage (usually within the  $\pm 0.5$ - $0.7$  V range). When indicated,  $I$ - $V$  curves were smoothed using the 75 point Savitzky-Golay smooth function prior to fitting using the IgorPro software (WaveMetrics).

Several pili purified from 4 WT or 2 Y27A independent cultures were used to collect  $I$ - $V$  curves for several regions per pilus fiber. Each pilus region was probed at several bias voltages (often 0.1, 0.5-0.7 and 0.9-1 V) to account for technical replication and the average resistance,  $R$ , for each pilus region was calculated from inverse slope of the linear portion of the  $I$ - $V$  curves. The resistance values were then plotted as a function of the distance (pilus length from the point of probing to the gold edge) using the Microsoft Excel software and the best fit was selected based on the trendline correlation coefficient ( $R^2$ ). The equation obtained for the best fit in the lower linear fit range (ca. 600 nm and below) was used to calculate the average resistance ( $R$ , in  $\Omega$ ) of a 1- $\mu$ m long pilus and this value was used to estimate the current ( $I$ , in amps) along the pilus at an applied voltage ( $V$ , in volts) of 100 mV and 450 mV using Ohm's law ( $I = \frac{V}{R}$ ). As one

amp represents the flow of 1 coulomb of electrical charge per second, I calculated the electron transport rates by multiplying the current value ( $I$ ) along a 1- $\mu\text{m}$  long pilus by the number of electrons in one coulomb ( $6.2415 \times 10^{18}$ ).

The average resistance value of a 1- $\mu\text{m}$  long pilus was also used to calculate the resistivity ( $\rho$ , in  $\Omega\cdot\text{cm}$ ) of the pilin assembly using the equation:

$$r = R \frac{A}{L}$$

where  $L$  is the nanowire length (in cm) and  $A$  is the cross-sectional nanowire area (calculated in  $\text{cm}^2$  using the 2 nm height measured by AFM for a cylindrical pilus nanowire).

#### **3.2.4 Calculation of Fe(III) oxide respiratory rates.**

The conductivity of the pili was interpreted in the context of the respiratory rates of the cells expressing pili during the reduction of Fe(III) oxides. I used the previously reported<sup>34</sup> rates of Fe(II) accumulation from the reduction of poorly crystalline Fe(III) oxide reduction and cell growth (measured as number of cells from cultures doubling every 15 h) to infer the amount of Fe(II) (in mol) solubilized per cell. The moles of Fe(II) per cell were then used to estimate the electron transport rate per cell by multiplying the moles of Fe(II) per cell by  $6.0221413 \times 10^{23}$  (Avogadro's number) (the reduction of Fe(III) to Fe(II) is a one-electron reaction). The electrons exported to the Fe(III) oxides per cell during the exponential phase of growth are shown. From the linear fit of this plot, I estimated transport rates of  $9 \times 10^6$  electrons per cell per sec.

#### **3.2.5 Electrochemical activity of anode biofilms in MECs**

The growth of cells and electroactivity of the biofilms from WT and mutant cells were assayed as in Chapter 2. HPLC and CSLM were also performed as in Chapter 2. I estimated the respiratory rates of anode biofilms as electrons per cell by dividing the current maxima of

WT anode biofilms grown in MECs fed with 1 mM acetate by the biofilm biomass estimated from confocal micrographs using the COMSTAT software<sup>126</sup> as described in Chapter 2. Electrons transferred per cell per sec were calculated as for the cells grown with Fe(III) oxides. The surface area of the electrode (1235431  $\mu\text{m}^2$ ) and previously reported cell dimensions<sup>19</sup> were used to determine the approximate number of cells in the anode biofilm.

### **3.3 Results and Discussion**

#### **3.3.1 Modeling the structure of the Geobacter pilus at high resolution via molecular dynamics**

There is currently a lot of debate in the field about the mechanism that enables the *Geobacter* pili to transfer electrons. Homology models take structural assumptions that lead to various interpretations and added to the controversy. Our approach has been to work synergistically with Dr. Gustavo Feliciano at the University of Sao Paulo in Brazil to couple theoretical and experimental studies that provide novel insights into the correlation between structure and function in this complex system. To this end, Dr. Feliciano constructed a high resolution structural model of the *G. sulfurreducens* pilus via molecular dynamics (Figure 14). My goal was to test the model predictions experimentally by constructing mutants with targeted amino acid replacements in amino acids predicted by the model to influence electron transfer through the pilus.

As reported for other type IV pili<sup>6</sup>, the MD model revealed the tight packing of pilins via hydrophobic interactions among neighboring  $\alpha$ -helices, which formed a central fiber core *ca.* 35 Å in diameter. The flexible C-t random coils from each pilin protruded at a 40 ° angle from the fiber core, extending the fiber's volume to a diameter of 47 Å. Such diameters are within the ranges (2-5 nm) estimated by atomic force microscopy<sup>34,43</sup> and scanning tunneling microscopy<sup>43</sup>. The rise of adjacent pilins in the fiber (*ca.*10.5 Å) was also similar to that reported

for other bacterial pili<sup>66</sup> and aligned residues F1 of one pilin with the E5 residue of the next. I demonstrated these interactions are required for *in vivo* pilin assembly in *G. sulfurreducens* in Chapter 2. Positively and negatively charged amino acids on one pilin and those of four neighboring pilins also interacted, forming salt bridges (D53 with K30 and D54 with R28) that have been proposed to strengthen pilin-pilin contacts.<sup>66</sup> The salt bridges also maintain the bend in the pilin's mid-region, where a proline residue (P22) increases the flexibility of the peptide, and allow for exposure of residues of the fiber core to the solvent for increased flexibility and dynamics (Figure 14). The model also revealed the clustering of aromatic residues, which formed a continuous helical region of high aromatic ring density along the length of the pilus model (Figure 14). This result is consistent with the idea that these residues are directly involved in electron transfer.

### 3.3.1.1 Potential ET pathways via aromatic residues

I analyzed the MD modeling data in order to identify possible ET paths involving aromatic residue contacts (Figure 15). Several ET steps are possible but two provide the shortest routes for electrons to move (Figure 16):

- 1) I identified a path for electrons involving two amino acids of the fiber core (Y27 and F24). The path has both intra and intermolecular dimers of these amino acids, with inter-aromatic ring distances averaging  $4.2 \pm 2.5 \text{ \AA}$  and  $14.4 \pm 2.4 \text{ \AA}$ , respectively. Thus, according to this model replacement of Y27 with an alanine should reduce ET rates significantly because the distance between the two closest F24 residues is too large ( $19.7 \pm 3.1 \text{ \AA}$ ).
- 2) A second path is also possible involving four amino acids of the fiber core (F24, Y27, Y32, and F51) and the only aromatic residue (Y57) of the C-t random coil. Inter-aromatic distances between F24 and Y27 average  $4.2 \pm 2.5 \text{ \AA}$ . In addition to the F24

to Y27 dimer, electrons can also move from F24 to Y32 ( $10.4 \pm 2.5 \text{ \AA}$ ). The same F24 can also pass electrons to a Y57 from the neighboring pilin, which is located  $14.2 \pm 3.1 \text{ \AA}$  apart. Y27 and Y32 can also pass electrons to Y57 inasmuch inter-aromatic distances between dimers are  $12.6 \pm 2.5 \text{ \AA}$  and  $17.6 \pm 2.7 \text{ \AA}$ , respectively. From Y57 electrons can move to F51 intramolecularly ( $9.1 \pm 2.7 \text{ \AA}$ ) and from F51 electrons move to the F24 of the neighboring pilin ( $7.3 \pm 2.5 \text{ \AA}$ ), repeating the path to Y27, Y32, and Y57. Distances of residues to the Y57 in particular may vary greatly in the pilus due to the highly flexible nature of the C-t random coil (Figure 2).

Inter-aromatic residue distances in both pathways are within the ranges reported for multi-step hopping pathways in other biological systems. In photosystem II, for example, tyrosine  $Y_z$  transfers electrons to  $P_{680}$ , which is positioned  $13.8 \text{ \AA}$  apart<sup>94</sup>.

The first path involves amino acids (F24 and Y27) that are buried in the fiber core. Thus, the path is unlikely to participate in the discharge of electrons to external electron acceptors such as Fe(III) oxides and uranium. By contrast, the second path includes amino acids (Y32 and Y57) with sufficient exposure to transfer electrons externally. Tyrosine 32 is located near a putative heme-binding motif (S25, R28, V29, K30, A31, S37, R41, L47, A50)<sup>83</sup> and could transfer electrons to *c*-type cytochromes. Such reactions are particularly relevant for the pili in the matrix of anode biofilms, which contains abundant *c*-type cytochromes required for ET to the underlying electrode. Y32 could bind the matrix-associated cytochromes, as it is located on the external surface of the pilus, and discharge electrons to them (Figure 17).

Y57 is also located on the external surface of the pilus. Y57 appears to be integral to pilus electron transfer by our model unless ET occurs in the core between Y27 and F24 residues (F24  $\rightarrow$  Y27 *ca.*  $4.2 \pm 2.5 \text{ \AA}$  and Y27  $\rightarrow$  F24 *ca.*  $14.4 \pm 2.4 \text{ \AA}$ ), but it may also play a role similar to Y32. Y57 is also surrounded (*ca.* 3-10  $\text{ \AA}$  radius) by negatively charged residues (D39, D53, D54, E60) as well as the C-terminal carboxyl group of the terminal serine S61

residue. The negative charges surrounding Y57 and exposure on the pilus surface could promote the binding of positively charged electron acceptors (e.g., Fe(III) oxides and the uranyl [U(IV)] cation). In particular D39, the carboxyl group of S61 and Y57 could form a cage of oxygen atoms all ca. 2-8 Å from each other (Figure 15). Studies of the human apotransferrin<sup>160</sup> show the uranyl ion bound by carboxylic acid groups from two amino acids and an oxygen from a tyrosine, with oxygen-to-uranium bond lengths of 1.8 – 2.5 Å. Given that the uranyl cation is ca. 2 Å in diameter, bond lengths in this range could be achieved in the pocket containing Y57. Consistent with this hypothesis, an atomic model derived from the L<sub>III</sub>-edge Extended X-ray Absorption Spectroscopy (EXAFS) spectra of uranium bound to *Geobacter pili* revealed a U(IV) atom coordinated by two bidentate carboxyl ligands like those found in the carboxyl groups of acidic amino acids<sup>13</sup> as well as a monodentate carbon ligand. Thus, the most exposed tyrosine, Y57, may be the terminal relay amino acid in the ET pathway to electron acceptors such as the uranyl cation, which are likely bound with great affinity by nearby negatively-charged ligands. This mechanism allows the pili to bind and reduce U(VI) extracellularly, preventing the toxic uranium from permeating the cell envelope and killing the cell<sup>13</sup>.

### **3.3.1.2 Potential ET pathway via the amide backbone**

In an  $\alpha$ -helix, the polypeptide backbone follows a helical path of 3.6 amino acid residues per turn of the helix, which aligns the backbone of amino and carbonyl groups and promotes hydrogen bonding (Figure 5). The natural hydrogen bonding found in  $\alpha$ -helices has been theorized to increase ET rates<sup>112,113</sup>. Hence, the possibility exists that ET through the pilus also involves a path through the amide backbone. A hybrid pathway containing a path through the amide backbone and short distance hopping between peptides was identified in the pilus structure (Figure 18). Charge hopping is possible between the F51 of one pilin subunit and the F24 of another, which are positioned 7.3 Å ( $\pm 2.5$ ) apart. Given the flexible nature of both  $\alpha$ -

helices and pili, it is possible that these residues could periodically be drawn within 3-4 Å of each other to create a  $\pi - \pi$  three electron bond<sup>106</sup>. The possibility of this shortening process is increased by the prediction that an adjacent hole draws the rings close to each other. The transient nature of this close distance would then cause the hole relay to continue<sup>106</sup>. The electron hole would then hop from F51 along the amino acid backbone via the amide groups until it reaches the next F24, and the path will repeat itself.

### 3.3.1.3 Contribution of the pilin's charged amino acids to ET

The inherent dipole of the pilin's  $\alpha$ -helix, which is accentuated by the unique distribution of charged amino acids, has been proposed to promote ET along the pilus<sup>45</sup>. The accentuated charge dipole created by the presence of these charged amino acids (Figure 2) could potentially contribute to charge hopping along the amide backbone<sup>67,108-110</sup>. Negatively charged amino acid residues can also act as proton acceptors for the pilin's tyrosines, enabling proton coupled electron transfer (PCET)<sup>92</sup>. As mentioned in Chapters 1 and 2, the oxidation potential of tyrosine is greatly reduced if it is first deprotonated, allowing it to mediate charge hopping at the low potentials that operate in biological systems. Not surprisingly, PCET is the major mechanism of ET in many well studied protein systems<sup>92</sup>. Consistent with a PCET mechanism, the helical band of high aromatic density revealed in the MD model of the *G. sulfurreducens* pilus is interspersed with the regions of the pili of highest negative potential. Furthermore, the tyrosine fluorescence emission spectrum of isolated *G. sulfurreducens* pili demonstrated that most of the tyrosines were in the deprotonated form (tyrosinate)<sup>159</sup>. Hence, the theoretical and experimental evidence supports the notion that acidic residues near tyrosine residues could facilitate PCET. As tyrosine residues have been more thoroughly studied in electron transfer through proteins, I focused on investigating the effects of tyrosine removal on ET first.

### 3.3.2 The role of tyrosine residues in biofilm electroactivity and Fe(III) oxide reduction

In chapter 2, I demonstrated that Tyr3, a mutant that carries alanine substitutions in the pilin's 3 tyrosines produces pili with increased resistance to the passage of electrons. Furthermore, Tyr3 biofilms grown in MECs had a reduced electrochemical activity and were phenotypically indistinguishable from a pilB mutant, which does not produce pili. To gain further insights into the role of tyrosines in ET through the pili, I constructed single alanine replacements in each of the pilin's tyrosines (Y27A, Y32A, and Y57A) and investigated the effect of the mutations in the electroactivity of anode biofilms in MECs fed with 3 mM acetate. Strains carrying the Y57A pili or Y32A mutations had defects in current production similar to the Tyr3 mutant (Figure 19Figure 12). However, no defect was observed for the strain producing Y27A pili (Figure 20) which is buried in the pilus core, Y32 and Y57 are exposed on the pilus surface. Hence, the exposed tyrosines are more likely to transfer electrons to external electron acceptors in the biofilm matrix such as *c*-type cytochromes, other pili, and other cells. Y32, in particular, forms a heme-binding motif with other amino acids of the pilus surface<sup>83</sup>, which could facilitate ET from the pili to *c*-type cytochromes. Y57, on the other hand, is in the flexible C-t random coil surrounded by negatively-charged amino acids and could bind ligands of the biofilm matrix via electrostatic interactions.

Similarly, I observed no significant differences in Fe(III) oxide cultures, with generation times for all strains tested averaging  $2.7 \pm 0.5$  days. These results indicate that ET pathways relying on Y27 as a keystone residue such as ET through the core via Y27->F24->Y27 hopping cannot be the sole pathway for ET. The lack of phenotype in the Y27A mutant strain indicates that pathways such as Y27->F24->Y27 hopping, where Y27 is key to the formation of intermolecular and intramolecular (highlighted in gray) are not essential. Therefore the pathways such as the one that includes the tyrosine on the C-t random coil (Y57) are operational for long distance charge transfer. The Y27 is not essential to this pathway due to the ability of F24 to

transfer electrons to Y57 (at a slightly farther average distance away). Therefore, the lack of a phenotype in the Y27A mutant strain does not dispute this model.

Interestingly, there were no intermediate phenotypes for current production in the MECs. As current is directly proportional to biofilm thickness<sup>31</sup> and it was found in Chapter 2 that strains that were defective only in pilus production were unable to grow beyond 10  $\mu\text{m}$ , this makes sense. If pili of a certain conductivity are required to grow beyond this threshold thickness, then the current will increase proportionally with biofilm thickness as they do although intermediate phenotypes may still be possible.

### ***3.3.3 The effect of alanine replacement of Y27 on pilus conductivity***

To test the correlation between pilus conductivity, current production in the MEC, and the predictions made by our model, I purified the Y27A pili and Dr. Sanela Lampa-Pastirk measured their transversal conductivity with a CP-AFM. As a control, the conductivity of the purified Y27F pili was also measured. As predicted by the model, the Y27A mutations had the most significant decreases in pilus conductivity, and genetically complementing the mutation with a phenylalanine in the Y27F culture partially restored the pilus conductivity to WT levels (Figure 21). The results thus support our earlier conclusion that Y27 is an important relay amino acid in the pilus' multistep hopping pathway. Furthermore, these findings indicate that the benzene ring rather than the hydroxyl group of the tyrosine is critical for optimal rates of ET. It is important to note, however, that the Y27A mutation could have caused a conformational change in the structure of the pilus such that the ET pathway was interrupted. However, the tight packing of pilins via hydrophobic interactions and salt bridges revealed in the MD model makes this interpretation less plausible.

To further investigate the effect of the Y27A in pilus conductivity, Dr. Sanela Lampa-Pastirk also measured charge transport along the pilus fibers in reference to the WT pili (Figure 22). For these experiments, the pili were deposited on the edge of a gold electrode

nanofabricated on an insulating SiO<sub>2</sub> substrate and the conductive tip of the CP-AFM was used to measure charge transport between the tip and the gold electrode through the pilus fiber while applying a bias voltage. Charge transport along the WT pilus was measured at distances of up to 1.5 μm away and revealed linear increases in pilus resistance with the distance of probing (Figure 22). Significantly, the resistance of the Y27A sample was greater at all the distances probed.

In analyzing the data, I identified two different correlations between distance and resistance in both the WT and Y27A pili (Figure 21). While the average resistance of the Y27A pili was 4.5-fold greater than the WT for distances of 500 nm or less, they were 5.5-fold greater beyond this threshold distance. For example, the average resistance of a 1 μm long WT pilus was *ca.* 430 MΩ or 720 MΩ depending on whether the slope of the first (less than 500 nm) or second (more than 500 nm) portions of the plot were considered. Similarly, the average resistance for a 1 μm long Y27A pilus was *ca.* 1.99 MΩ or 3.96 MΩ, respectively.

Even when using the greatest resistance values, I calculated a pilus resistivity of 0.23 Ω.cm and 1.25 Ω.cm for the WT and Y27A pili, respectively. The calculation of these resistivities assumed a pilus diameter of 2 nm estimated or the pilus height AFM. As the AFM tip can flatten the sample during probing and underestimate the pilus height, I also calculated the resistivity of the pilus using the 47 Å diameter estimated for the preferred MD pilus conformer, which has the C-t random coils at a 40 ° angle from the pilus core<sup>137</sup>. This diameter also matches the diameter of the pilus estimated by scanning tunneling microscopy (*ca.* 5 nm)<sup>43</sup>. The resistivity of a pilus with a 47 Å diameter was 1.25 Ω.cm for the WT and 6.88 Ω.cm for Y27A pili. All of these values are within the lowest ranges reported for moderately doped nanowires<sup>161</sup>.

I also calculated the average electron transport rate for the WT and Y27A pili using the lower and upper ranges of resistance described above. For the WT pilus, I estimated electron transport rates between 9 x 10<sup>8</sup> to 1 x 10<sup>9</sup> electrons per sec at a potential of 100 mV. For the

Y27A pilus, I estimated electron transport rates between  $1.5 \times 10^8$  to  $3 \times 10^8$  electrons per second at the same potential. These rates of electron transfer are much higher than the cellular rate of respiration of Fe(III) oxides, which I estimated to be ca.  $9 \times 10^6$  electrons per cell per sec (Figure 23). This result helps explain why there was no significant difference between the WT and Y27A during the reduction of Fe(III) oxides (Figure 20).

I also calculated a cellular rate of respiration of anode electrodes of ca.  $2\text{-}3 \times 10^8$  electrons per cell per sec using the maximum current and biofilm biomass measured experimentally in MECs fed with 1 mM acetate (Chapter 2). This rate is within the ranges calculated for electron transport rates for both the WT and Y27A pili. Hence, as observed for the Fe(III) oxide cultures, the Y27A variant does not reduce charge transport through the pili sufficiently to limit optimal current production in MECs. The increased resistance along the pili maybe be due to the closer proximity of Y27 to Y57 (the next aromatic in the ET chain). It may also be due to the loss of a  $\pi\text{:}\pi$  bond slowing the rate of electron hole transfer. This is supported to the close proximity of Y27 to F24. F24 is part of the phenylalanine dimer predicted to be used for intermolecular pilin transfer in the case of amide bond hopping (Figure 18 Amide electron hole hopping and phenylalanine dimer intermolecular transfer pathway). Y27 is also six  $\alpha$ -helical hydrogen bonds away from the other half of this dimer, F51 and could therefore affect transfer between these two aromatic residues.

### **3.3.4 Effect of phenylalanine replacements of the pilus tyrosines**

Though the role of phenylalanines in protein ET is not fully understood, phenylalanine residues have been reported to influence and even mediate charge transfer in proteins and peptides<sup>103</sup>. Hence, I investigated the effect of phenylalanine replacements of the pilin's three tyrosines on the electrochemical activity of anode biofilms in MECs. I therefore constructed a mutant carrying Y27F, Y32F, and Y57F substitutions in the pili (Tyr3-F) and compared its growth and electrochemical activity in MECs to the Tyr3 mutant, which carries alanine

replacements in the same tyrosines. Unlike the Tyr3 mutant, which has a defect in current production comparable to a non-piliated strain pilB (Chapter 2), the Tyr3-F mutant had no defect in current production (Figure 24). This suggests that the phenylalanine residues are able to participate in ET in the *G. sulfurreducens* pilus. Additionally, the phenotype of the Tyr3-F mutant also rules out a role for post translational modifications of the tyrosines (which target the residue's hydroxyl group) in ET through the pilus.

### **3.3.5 Effect of negatively-charged amino acids of the pilus**

The pilin's aspartic acid residues D53 and D54 are in close proximity to the pilus tyrosines and could serve as proton acceptors for PCET. In addition, the two aspartic acid residues are located in the C-t end of the  $\alpha$ -helix and contribute to the steep dipole of the pilin, which is predicted to promote ET<sup>45</sup>. Hence, I took a genetic approach to investigate the role of these residues in charge transfer through the pilus. I constructed a mutant carrying alanine substitutions in both D53 and D54 (Asp2 mutant) and compared its ability to produce current in a MEC to the Tyr3 mutant. As shown in Figure 25, the Asp2 culture produced current at rates ( $0.52 \pm 0.11$  mA/day) four-fold lower than the WT cells and also had two-fold decreases in current maxima ( $0.68 \pm 0.05$  mA). The Asp2 defect was similar to the Tyr3 mutant, indicating that both mutants have a reduced ability to discharge respiratory electrons in anode biofilms. Furthermore, the Asp2 cells initially colonized the electrode like the WT culture, but they required more time (~12 h) to begin the exponential phase of biofilm growth and current generation (Figure 25, inset). Hence, the *in vivo* studies support the model predictions that the local electrostatic environment around the aromatic residue contacts and the surface properties of the pilus influence the rates of electron transfer through the pili. Generation times for the Asp2 during growth with Fe(III) oxides were also two-fold greater in the Asp2 cultures compared to the WT controls, though the defect was not as pronounced as the Tyr3 mutant, but

supplementing the Asp2 cultures with the metal chelator NTA to alleviate the need of the cells to transfer electrons via pili<sup>34</sup> chemically rescued the growth defect (Figure 25).

It is unlikely that the only role of the aspartic acid residues is to deprotonate tyrosines for PCET because the Tyr3-F mutant had no defects in MECs (Figure 24). The MD model of the pilus does predict that an Asp2 mutation reduces the flexibility of the pilus because D53 and D54 form salt bridges with R28 and K30 with adjacent pilin monomers, and in the mutant new salt bridges form that make the pilus more rigid<sup>137</sup>. This effect could decrease the ability of the pilus to bind and transfer electrons to extracellular electron acceptors of the biofilm matrix such as c-type cytochromes. Furthermore, although the Asp2 pilus fiber maintained the same number of aromatic residue contacts as the WT pilus, the type of aromatic residues involved in the contacts and their configuration changed and average inter-aromatic residue distances increased<sup>137</sup>. Thus, the Asp2 phenotypes in MECs and Fe(III) oxide cultures indicate that the local electrostatic environment around the aromatic residue contacts influences the aromatic ring configuration so as to promote efficient ET.

### **3.4 Conclusions**

At the beginning of my graduate work, it was not known if the pili of *G. sulfurreducens* could transport electrons through the length of the pilus. My collaborative work with Dr. Sanela Lampa-Pastirk demonstrated that the pili are protein nanowires and utilize specific amino acids of the pilin (such as Y27) for long-range charge transport. Although this residue was not required for optimal electrochemical activity of anode biofilms, the other two tyrosines (Y32 and Y57) were required. These tyrosines, unlike Y27, are exposed on the pilus surface and may serve as terminal relay amino acids of the pilus pathway for the reduction of redox active components of the biofilm matrix such as c-type cytochromes.

Insights into the amino acids that mediate ET in the pilus also resulted from a collaborative effort with Dr. Feliciano, who constructed a high resolution model of the *G. sulfurreducens* pilus using molecular dynamics simulations<sup>137</sup>. The packing, alignment, and geometric configuration of aromatic residues in the MD model are consistent with a mechanism for charge transport dominated by multistep hopping and ruled out any  $\pi$ -stacking required for metallic conductance. I tested the model predictions about the role of tyrosines in the multistep hopping pathways by constructing a Tyr3 mutant and demonstrated its inability to discharge respiratory electrons to Fe(III) oxides or produce current in MECs optimally. However, the tyrosines could be replaced with phenylalanines without any defects in pili-functions, highlighting the importance of the electron rich  $\pi$ -bonds found in these aromatic side chains in ET through the pilus. I also constructed an Asp2 mutant and validated the model's predictions about the importance of the local electrostatic environment around the aromatic contacts to align the aromatic residues in configurations that promote optimal ET.

My studies also highlighted the role of tyrosines exposed on the pilus surface (Y57 and Y32) (Figure 17) on ET *in vivo*. Y57 is of particular interest in transversal ET as it is not only on the external face of the pilus, but is also in close proximity to several negatively charged amino acids (D39, D53, D54, E60) and the C-terminal carboxyl group of S61. The negatively charged residues position carboxyl ligands in close proximity to Y57, which could promote the binding of positively charged electron acceptors such as Fe(III) oxides and the uranyl cation (Figure 17). Experimental evidence exists in support of this model: the atomic environment of the pili-bound uranium modeled from the uranium L<sub>III</sub>-edge Extended X-ray Absorption Spectroscopy (EXAFS) spectra is that of a reduced U(IV) atom coordinated by two bidentate carboxyl ligands like those found in the carboxyl groups of acidic amino acids<sup>13</sup>. Furthermore, other proteins utilized carboxyl groups to coordinate uranium<sup>160,162</sup> as well as tyrosine residues<sup>160</sup>.

While the results presented in this chapter provide novel mechanistic understanding of ET through the *G. sulfurreducens* pilus, many questions still remain. Alanine replacements of all three tyrosine residues investigated in this study displayed negative ET phenotypes. This supports electron hopping via redox-active stepping stones; however, it does not dismiss the possible role of amide hopping to ET. Also, while the charged amino acid residues tested are required for both WT levels of Fe(III) oxide reduction and current production, this result could be indirect by the generation of the pilin dipole, as important structural components, by promoting binding to cationic electron acceptors, or as proton acceptors. Finally, the contribution of PCET to the pilus conductivity cannot be dismissed.

**CHAPTER 4. INTRAMOLECULAR CHARGE TRANSPORT IN PILUS NANOWIRES  
INVESTIGATED IN PILIN-ELECTRODE INTERFACES**

## 4.1 Introduction

The ability of *Geobacter sulfurreducens* to transfer electrons to external electron acceptors such as metals, radionuclides, or electrodes in microbial electrochemical cells (MECs) has applications in a variety of fields including bioenergy, bioremediation, and nanotechnology<sup>118,163</sup>. At the most fundamental level, these applications depend on the ability of the cells to transfer electrons to external electron acceptors using type IVa pili (T4P)<sup>13,32,34</sup>. The T4P of *G. sulfurreducens* are only 2-5 nanometers in diameter yet several micrometers in length<sup>34</sup>. In addition, the pili are conductive<sup>34</sup>, a property that is not mediated by bound metal ions or organic cofactors but, rather, depends on the ability of the protein fiber to conduct electrons (Dr. Sanela Lampa-Pastirk, unpublished data). These findings indicate that the conductive nature of the pili is due to the amino acids within the pilin subunits. Due to their conductive nature and geometry, pili have the potential to be used as nanowires in bioelectronic applications<sup>34,159,164</sup>.

Critical to the biotechnological applications of *Geobacter* pili is the elucidation of their mechanism of conductivity. In Chapters 2 and 3 I presented evidence supporting the role of tyrosines of the pili in charge transport and the contribution of the local electrostatic environment around the aromatic residues in pilus conductivity and biological functions. Furthermore, replacement of the two tyrosines with highest exposure on the pilus surface was sufficient to reduce the electrochemical activity of *G. sulfurreducens* anode biofilms (Figure 19). This result highlighted the importance of interactions between the pili and other redox-active components of the biofilm matrix such as *c*-type cytochromes in biofilm conductance. I also demonstrated that the loss of Y27, the tyrosine involved in the formation of an intramolecular contact in the pilin assembly<sup>137</sup>, decreased the pilus' ability to conduct electrons at long (> 500 nm) distances (Figure 22). These findings support the multistep hopping mechanism via tyrosines predicted in molecular dynamics (MD) simulations of the *G. sulfurreducens* pilus in solution<sup>137</sup>. In this model,

the assembly of the pilins clusters the aromatic residues (phenylalanines and tyrosines) of neighboring subunits with inter-aromatic distances and dimer configurations optimal for multistep hopping. The aromatic contacts were between aromatic residues of the same or adjacent pilins, consistent with a mechanism that integrates intra- and inter-molecular pathways for electron transfer through the pili<sup>137</sup>.

Evidence for intramolecular charge transport also comes from *ab initio* studies of the *G. sulfurreducens* pilin, PilA<sup>45</sup>. The *G. sulfurreducens* pilin is significantly truncated compared to the typical type IVa pilin, lacking the conserved large globular head domain of other bacterial pilins and reducing the *Geobacter* pilin to a small (61-aa) and predominantly  $\alpha$ -helical peptide (Figure 1). Helical structures accelerate electron transfer reactions due to the hydrogen bonding and natural dipole moment inherent in the structure<sup>67,112,113,165</sup>, even at lengths significantly longer than the *G. sulfurreducens* pilin<sup>68</sup>. As such, the predominantly helical structure of the *G. sulfurreducens* pilin is predicted to create a peptide environment optimal for electron transfer<sup>45</sup>. In addition, the dipoles of the peptide bonds align in the  $\alpha$ -helix and polarize the pilin (Figure 2). Such dipole moments have been previously found to enhance electron transfer in helical peptides<sup>67</sup> and are predicted to lower the electron band gap of the *G. sulfurreducens* pilin<sup>45</sup>. Furthermore, specific amino acids of the pilin enhance the natural dipole and contribute to the electrostatic effects that reduce the electronic band gap of the pilin<sup>45</sup>. Among the amino acid acids predicted to contribute to the unique electronic structure of the pilin are several charged and aromatic residues. Hence, the results indicate that the divergent structure and amino acid composition of the pilin favor electron transfer (ET) reactions. Furthermore, they also suggest that intramolecular charge transfer is possible through the pilin. As the pilin is 61 amino acids long and therefore too long for electron tunneling to occur, it is likely that this charge transfer would occur via electron or hole hopping via the amine backbone of the pilin as seen in other  $\alpha$ -helical peptides<sup>68,88</sup>.

Given the multimeric nature of T4P, it is challenging to determine the contribution of the predicted intramolecular conductivity to the pilus conductivity. To address this limitation, I used recombinant technologies to mass-produce a truncated PilA peptide that could be assembled *in vitro* into fully functional protein nanowires, in a collaborative effort between myself and Dr. Angelines Castro-Forero, a student in the laboratory of Dr. R. Mark Worden (Chemical Engineering Department, Michigan State University). As a team we sought to mass-produce protein nanowires for biotechnological applications. Individually, I aimed to develop hybrid pilin-electrode systems for the interrogation of the pilin's conductive properties and the contribution of intramolecular charge transport. To this end, I constructed genetic systems for the large-scale recombinant production of truncated pilin monomers, which retained the pilin's  $\alpha$ -helical structure and amino acids critical to electron transport. My collaborator Dr. Castro-Forero screened some of the recombinant systems, and developed protocols for the purification of pilin monomers at high yields and their *in vitro* self-assembly<sup>166</sup>. I then functionalized one of the truncated peptides (PilA<sub>19</sub>) with an amino-terminal (N-t) cysteine residue (PilA<sub>19</sub>-A20C) to chemically attach the pilins to gold electrodes and electrochemically interrogate the intramolecular pathway of electron transfer in pilin-electrode interfaces. I also constructed PilA<sub>19</sub>-A20C derivatives carrying alanine replacements in the Y27, Y32, and Y57 residues in order to characterize the role that these amino acids play in pilus conductivity. Elucidating the method of pilin ET will not only enable us to understand protein-dependent long distance ET in organisms like *Geobacter*, it will allow us to manipulate this system for producing wires with differing electronic capabilities.

## **4.2 Materials and Methods**

### **4.2.1 Construction of Expression Strains**

#### **4.2.1.1 QIAexpress™ system (His-tagged pilins)**

Primers were design to generate both the full length protein and various truncation variants to determine the minimum number of hydrophobic amino acids on the pilin N-terminus required to enable efficient expression and purification of the protein (Table 6). The QIAexpress™ expression system (Qiagen) was used to generate N-terminal hexapolyhistidine-tagged (6×His-Tag) truncations of the PilA peptide to facilitate purification. PCR amplification of purified *G. sulfurreducens* genomic DNA (gDNA) was performed (denaturation time of 5 min at 95 °C, 30 cycles of 30 s at 95 °C, 20 s at 50.7 °C, 1 min at 72 °C followed by an extension time of 5 min at 72 °C) with 100 ng of gDNA and Platinum® Taq DNA Polymerase High Fidelity (Invitrogen). PCR products were gel purified using the Zymoclean™ Gel DNA Recovery Kit (Zymo Research). The products were then ligated into the pQE-30UA (Table) expression vector and transformed into *E. coli* M15[pREP4] cells (Table 5).

#### **4.2.1.2 pMAL™ system (MBP-tagged pilin)**

The pMAL™ protein fusion and purification system (New England Biolabs Inc.) was used to generate N-t maltose binding protein (MBP) fusions of the PilA peptide. PCR amplification of purified *G. sulfurreducens* genomic DNA was performed as described above with the use of Herculase II Fusion DNA Polymerase (Agilent Technologies) using primers (Table 6). PCR products were gel purified using the Zymoclean™ Gel DNA Recovery Kit (Zymo Research). Plasmids were digested with HindIII and XmnI (NEB) and the PCR products with HindIII. The digested plasmids and PCR products were purified and ligated using T4 DNA ligase (New England Biolabs Inc.) and transformed into DH5α (

Table 5). For protein expression experiments the recombinant plasmids were transformed into K12 TB1 cells (Table 5).

#### **4.2.1.3 IMPACT™ system (CBD-tagged pilins)**

The IMPACT™-CN protein expression system was used to generate N-t and C-t fusion proteins containing the PilA peptide (full length) or truncated derivatives (PilA<sub>10</sub>, PilA<sub>19</sub>, PilA<sub>20</sub>, and PilA<sub>22</sub>) and a chitin binding domain (CBD)-intein fusion (New England Biolabs Inc. Incorporated). PCR amplification of purified *G. sulfurreducens* genomic DNA was performed as described above with the use of Herculase II Fusion DNA Polymerase (Agilent Technologies) using primers (Table 6). PCR products were gel purified using the Zymoclean™ Gel DNA Recovery Kit (Zymo Research). The pTYBII plasmid and PCR products were subsequently digested with SapI and PstI (Life Technologies). The digested plasmid and PCR products were purified, ligated using T4 DNA ligase (New England Biolabs Inc.), and transformed into DH5α. The resulting plasmids were then transformed into Rosetta™ 2 (DE3) pLysS cells (Table 5) for protein expression experiments.

#### **4.2.1.4 Mutagenesis of codons for pilin amino acids**

All amino acid replacements were made with the DNA encoding the 19-amino acid truncation variant. I first constructed a PilA<sub>19</sub> derivative carrying a cysteine tag (PilA<sub>19</sub>-A20C) for utilization in gold electrode experiments. Then, several PilA<sub>19</sub> derivatives carrying either: amino acid substitutions in all of the pilin's tyrosine residues (Y27A, Y32A, and Y57A), two of the aspartic acid residues (D53 and D54), and R28 were generated in this strain. All mutations were introduced using the QuikChange Lightning Site-Directed Mutagenesis kit (Agilent Technologies). To generate the triple tyrosine variant (Tyr3) after the first mutation of the DNA was confirmed, the process was repeated two times, each time with a different primer set. The

double aspartic acid variant (Asp2) was generated with a single mutagenesis run with a primer containing both mutations. Primers carrying the desired point mutations (Table 6) were used to PCR-amplify the pTYB11::*pilA*<sub>79</sub> plasmid (Table 6) (denaturation time of 2 min at 95 °C, 18 cycles of 20 s at 95 °C, 10 s at 60 °C, 6 min 30 s at 68 °C followed by an extension time of 5 min at 68 °C). Methylated DNA was then digested with DpnI (Agilent Technologies) and the plasmids were transformed into XL10-Gold cells (Table 5) following the manufacturer's recommendations. Plasmids were isolated from ampicillin resistant colonies using the ZR Plasmid Miniprep™-Classic kit (Zymo Research) and sequenced to confirm the mutations. Confirmed plasmids were transformed into Rosetta™ 2 (DE3) pLysS cells (Table 5) for protein expression experiments.

#### **4.2.2 Expression of recombinant pilins**

The expression efficiency in *E. coli* of recombinant pilins tagged with a 6xHis region was first assessed in small-scale (50 ml) cultures grown in lysogeny broth (LB) medium. Antibiotics were added at the following concentrations: ampicillin (Amp) 100 µg/mL and kanamycin (Kan) 25 µg/mL. Cells were grown at 37 °C aerobically with agitation (250 rpm) and recombinant protein expression was induced with 1 mM isopropyl-1-thio-D-galactopyranoside (IPTG) once the cultures reached an OD<sub>600</sub> between 0.5 and 0.7. Cells were harvested 5 h post-induction by centrifugation (4,000 x *g* for 20 min at 4 °C), suspended in 20 mM Tris-HCl pH 7, and sonicated on ice 3 times (duty cycle 30%, output 3, for a total of 10 pulses) using a Branson sonifier 450. Supernatant fluids were recovered by centrifugation and 4x Tris-glycine loading buffer was added. The pellets were suspended in Tris-glycine loading buffer (62.5 mM Tris-HCl, pH 6.8, 25% glycerol, 2% SDS, 0.01% Bromophenol Blue, 5% β-mercaptoethanol). Approximately 10 µg of protein from supernatant fluids or pellet samples was loaded onto a 12% Tris-Glycine acrylamide gel (Bio-Rad Laboratories, Inc.) which was run at 100 V for 70 min. Proteins were transferred to a Hybond-ECL nitrocellulose membrane (Amersham Biosciences) using a Mini

Trans-Blot cell<sup>®</sup> (Biorad) over 1.5 h at 170 mA. The membrane was blocked with 5 % (w/v) non-fat dry milk in Tris-buffered saline (20 mM Tris, pH 7.4, 0.9% NaCl) for 3 h. The membrane was incubated with the primary antibody ( $\alpha$ -PilA serum or  $\alpha$ -His tag (Qiagen); 1:100 or 1:2,000 dilution, respectively) overnight. The membrane was incubated with the secondary antibody (anti-rabbit IgG-AP conjugated (Sigma) 1:2,000 dilution). Visualization was performed at room temperature using nitro-blue tetrazolium and 5-bromo-4-chloro-3'-indolyphosphate (NBT/BCIP) solution (Sigma-Aldrich).

Expression studies of MBP- and CBP-tagged pilins were performed by collaborator Dr. Angelines Castro-Forero and have been described in detail elsewhere<sup>166</sup>.

#### **4.2.3 Purification of recombinant pilins carrying a Chitin-binding domain protein tag**

The IMPACT<sup>™</sup> expression system was selected for the large-scale production of pilins. The recombinant strains were grown to mid-exponential phase ( $OD_{600}$  of 0.4–0.5) in one liter of LB medium at 37 °C with shaking (250 rpm). Protein production was induced with 0.5 mM IPTG at 16 °C overnight. The cells were harvested by centrifugation and the cell pellets were frozen at -80 °C for at least one day. The cell pellets were suspended in 30 ml of lysis buffer (Table 8) and lysed by sonication (see above) in an ice bath. The soluble fraction was recovered by centrifugation at 110,000 x  $g$  for 30 min at 4 °C and passed through an affinity column containing ca. 30 ml of chitin beads (New England Biolabs Inc.) previously washed with 4 column volumes of column buffer (Table 8) and equilibrated for 30 min. Non-specifically bound proteins were removed from the column with 4 column volumes of wash buffers 1 and then 2 (Table 8), containing increasing concentrations of NaCl. Recombinant pilins, which bound the chitin resin in the column beads, were subsequently removed from the column after self-cleaving the peptides from the chitin-binding domain with 50 mM dithiothreitol (DTT) dissolved in elution buffer (Table 8). On-column cleavage was allowed to proceed at room temperature for 24 h. Cleaved recombinant pilins were eluted from the column with elution buffer (containing 5

mM DTT for the cysteine-modified pilins) and fractions containing protein were identified by their absorbance at 280 nm and pooled.

The buffer solution containing recombinant pilins was exchanged after passing it through a Waters Sep-Pak 3 cc C18 vac cartridge. The C18 cartridge was first wet with 1.5 column volumes of acetonitrile and then equilibrated with 1.7 column volumes of ddH<sub>2</sub>O. Eluted pilin samples were then loaded onto the column and washed with ddH<sub>2</sub>O (6x column volumes). Protein was eluted in 1.7 column volumes of acetonitrile and stored in a 5 ml serum vial to prevent oxygen contamination. The same procedure was used for solutions containing recombinant pilins functionalized with an N-terminal cysteine amino acid, but inside an anaerobic glove bag to prevent oxidation of the cysteine tag. For dialysis experiments recombinant pilins were dialyzed overnight two times in anaerobic elution buffer (without DTT) at 4 °C. The purified recombinant pilins were stored on ice, or flash-frozen in liquid N<sub>2</sub> and stored at -80 °C for long-term storage.

#### **4.2.4 Electrochemical characterization of Pila<sub>19</sub>-A20C monolayers on gold electrodes**

Gold electrodes (LGA Thin Films, Santa Clara, CA) were cut into small pieces and cleaned with piranha solution (7 parts by volume concentrated sulfuric acid to 3 parts by volume 30% aqueous hydrogen peroxide)<sup>a</sup>. Each piece was then washed copiously with ddH<sub>2</sub>O, dried with N<sub>2</sub> and placed in a separate plastic scintillation vial. A 1:2 dilution of the recombinant Pila<sub>19</sub>-A20C pilin suspended in acetonitrile or elution buffer (Table 8) was added to each vial with an electrode and incubated for various periods of time (48 h ended up the standard deposition time to ensure coverage) at room temperature inside an anaerobic chamber containing a H<sub>2</sub>:CO<sub>2</sub>:N<sub>2</sub>

---

<sup>a</sup> Caution: piranha solution is an extremely strong oxidant and potentially explosive; it must be handled with extreme care.

(7:10:83) atmosphere. The pilin-electrode interfaces were washed with 100% ethanol and incubated with 1 mM 1-undecanethiol (in ethanol) for 48 h at room temperature in the anaerobic chamber. When indicated, controls of electrodes covered with 1-undecanethiol were generated by incubation of a clean gold electrode with a 1 mM 1-undecanethiol solution for 48 h at 25 °C. 1-undecanethiol was also used to cover any gaps in pilin coverage on the electrode. Gold electrode controls were incubated in the solvents without recombinant pilins or 1-undecanethiol for use as a positive control.

The thicknesses of the pilin monolayer that formed on the electrode was measured with a M-44 rotating analyzer ellipsometer (J.A. Woollam Co., Inc., Lincoln, NE) controlled by WVASE32 software. The incident angle was set at 75° using 44 wavelengths of light between 414.0 and 736.1 nm. The refractive index (n) and extinction coefficient (k) were assumed to be  $n = 1.5$  and  $k = 0$ , respectively. Thickness measurements were averaged from measurements of 3 random spots taken from each of five electrodes.

Before the electrochemical experiments, the pilin-electrode interfaces were rinsed with ethanol and dried under N<sub>2</sub>. Cyclic voltammetry measurements used a conventional three-electrode cell consisting of the pilin-functionalized working electrode, a platinum auxiliary electrode, and a 3M silver/silver chloride (Ag/AgCl) reference electrode. Measurements were performed in a 100 mM phosphate buffer, pH 7.0 containing 100 mM NaCl and 5 mM potassium ferricyanide (K<sub>3</sub>[Fe(CN)<sub>6</sub>]). The electrochemical experiments were performed using a CHI660 potentiostat (CH Instruments, Austin, TX).

## **4.3 Results**

### **4.3.1 Rationale for partially truncating the N-terminal hydrophobic pilin region**

The heterologous expression of the *G. sulfurreducens* pilins in a recombinant host such as *Escherichia coli* is necessary for their mass-production, yet is challenging due to the

hydrophobicity of the pilin peptides. Expression in the native host is possible because the pilin protein is expressed as precursor containing an N-t leader peptide containing a large number of charged amino acids. The polar leader peptide of type IV pilins effectively decreases the peptide's hydrophobicity to prevent intracellular aggregation and is also recognized and cleaved by a dedicated signal peptidase, which also methylates the phenylalanine F1 of the processed pilin to prepare it for assembly<sup>50</sup>. Once assembled, the pilin subunits of T4P are held together predominantly by interactions within the hydrophobic  $\alpha$ -helical region, which spans more than 50 amino acids at the N-terminus<sup>66</sup>. Such hydrophobic interactions can promote the aggregation of recombinant proteins inside the expression host and the formation of inclusion bodies. The latter make purification of the target protein challenging and time intensive which is undesirable in an industrial setting. Furthermore, at the high levels of expression required for our project, proteins containing hydrophobic regions often insert into host membranes, killing the recombinant host cell and reducing expression yields.

One way to address the challenges associated with the recombinant expression of hydrophobic pilins is to truncate the most N-terminal (N-t) amino acids. These amino acids include F1 and E5, which, as I showed in Chapter 2, are required for the recognition and assembly of the pilins in the native host, but they are not required for the *in vitro* assembly. N-t truncations thus make the pilin less hydrophobic, thereby enabling both their recombinant expression and purification. Truncation of 35 amino acids of the N-t region of the pilin of *Pseudomonas aeruginosa* was used, for example, to produce recombinant PA pilins at high yields and assemble them into fibers in the presence of a hydrophobic matrix<sup>57</sup>. These studies thus demonstrated that it is possible to assemble pilins carrying truncations of more than half of the  $\alpha$ -helix region. This is because the truncated pilins retain charged amino acids involved in the formation of salt bridges, which align the pilins in the proper orientation, and strengthen the hydrophobic interactions between adjacent helices<sup>57</sup>. Such truncations are not desirable in the

*Geobacter* pilin because several aromatic amino acids predicted to be critical to electron transport (F24, Y27, and Y32) and the formation of salt bridges (R28 and K30) are located in this N-t region<sup>137</sup>. Hence, ideally, the truncations of the pilin of *G. sulfurreducens* had to be of 23 amino acids or less.

The truncation design involved first an analysis of the hydrophobic regions and aggregation potential of the mature PilA peptide (i.e., the pilin without its signal peptide) using the AGGRESCAN, GRAVY, and a Kyte Doolittle plot servers. AGGRESCAN<sup>167</sup> uses an algorithm that predicts “hot spots” of aggregation by assigning each amino acid an aggregation-propensity value (a positive value indicates a propensity for aggregation). This approach identified two hot spots of aggregation in the PilA peptide spanning residues 1-22 and 25-31 (Figure 27). The average aggregation-propensity value for the protein remains positive until the truncation of the first 10 amino acids. To corroborate the AGGRESCAN analysis, I used GRAVY<sup>168</sup> to analyze the average hydrophobicity of the PilA protein. GRAVY calculates the average hydropathy value of the amino acids in a protein, with positive values indicating overall hydrophobicity. The analysis of the PilA peptide using this approach indicated that a truncation of 11 amino acids within the N-t region is necessary before the GRAVY value becomes negative. By contrast, a Kyte Doolittle plot<sup>168</sup>, which calculates the localized hydrophobicity along the length of the protein, shows the portion of the peptide containing the first 21 amino acids is considered hydrophobic (Figure 27). All together, the computational predictions indicated that a truncation of at least 10–20 amino acids is necessary to solubilize the pilin peptide and facilitate its recombinant production. Truncations within this range also retain the amino acids predicted to serve as relay stations for multistep hopping pathways through the pilus<sup>137</sup>. Furthermore, the truncations do not remove charged amino acids of the pilin, which are required to form salt-bridges between neighboring pilins and influence the local electrostatic

environment around the aromatics that is critical to maintain proper inter-aromatic distances and configurations for electron transfer<sup>137</sup>.

### **4.3.2 Construction and heterologous expression of recombinant pilins**

#### **4.3.2.1 Recombinant production of pilins carrying an N-t His-Tag**

I first explored the possibility of heterologously expressing truncated pilins fused to an N-t hexa polyhistidine tag (6×His-Tag) using the QIAexpress<sup>TM</sup> expression system. The 6×His-Tag increases the solubility of the recombinant protein and capitalizes on the metal binding affinity of the histidine residues for nickel and cobalt to purify them in a metal-containing matrix.

Furthermore, the small size of the 6x-His-tag has been reported to not interfere with protein stability or folding. As the expression of large quantities of foreign proteins, especially those that are hydrophobic, can often be cytotoxic, the M15[pREP4] (Table 5) host strain was used for expression. This host strain permits high levels of expression for the recombinant proteins when induced, but permits the culture to grow normally up to high cell densities before induction due to strong repression of the heterologous gene. Therefore, in case of toxicity, the culture is already at densities sufficient for large amounts of protein production prior to induction. Full-length pilin as well as sequential 5-amino acid truncations (up to 20) were successfully fused to the 6xHis tag.

Despite the LacI repression of pilin transcription expected before IPTG induction, each trial expression study showed protein expression in both induced and un-induced cultures (Figure 28). Furthermore, Western blots revealed multiple protein bands in all of the samples when using either an  $\alpha$ -PilA antibody or an  $\alpha$ -His6x antibody (Figure 28). This result suggested that the recombinant peptides were aggregating. Consistent with this proposal, the majority of the protein bands were identified in the insoluble fraction, regardless of truncation length. The results indicated that even with substantial truncations (up to 20 amino acids) to decrease the

hydrophobicity of the pilin, larger tags are needed to increase the solubility of the peptides to levels such as that recombinant expression yields are high and aggregation is minimized.

#### **4.3.2.2 Recombinant production of pilins carrying a MBP**

I chose the pMAL<sup>TM</sup> protein fusion and purification system because it allowed me to fuse the pilin to a large globular protein, the maltose binding protein (MBP), which is expected to increase the pilin's solubility. This tag has previously been shown to effectively solubilize hydrophobic proteins, including other bacterial pilins<sup>61</sup>. Additionally, the MBP tag can be cleaved by the protease Factor Xa at a specific recognition site (I-E/D-G-R) introduced before the pilin. Thus, cleavage removes the tag in its entirety and does not leave non-native amino acids in the recombinant protein. For these experiments, I first cloned the *pilA*<sub>20</sub> pilin gene into the XmnI restriction site of the plasmid, which is located directly after the region encoding a Factor Xa recognition sequence that separates the MBP region from the target protein and allows for the cleavage of the full tag with the Factor Xa protease. My collaborator, Dr. Angelines Castro Forero, tested the expression system and demonstrated its suitability to express the PilA<sub>20</sub>-MBP fusion protein and its purification using an amylose affinity column<sup>166</sup>. Furthermore, she was able to recover the PilA<sub>20</sub> peptide upon protease cleavage (Figure 31).

Another advantage of this system is that it allows for the periplasmic expression of the recombinant fusion. Periplasmic expression of recombinant proteins has been shown to provide many benefits including increased solubility, decreased production of inclusion bodies, increased protein stability, and a decreased cellular protein contamination<sup>169</sup>. The recombinant fusions can be purified by the use of an amylose resin, which binds MBP, and eluted by the addition of maltose to the column. Hence, I constructed both cytoplasmic and periplasmic expression systems for PilA<sub>20</sub> and cloned the plasmids into *E. coli* K12 TB1 (Table 4.1). As shown in (Figure 29) and (Figure 30), the MBP-PilA<sub>20</sub> fusion protein were successfully expressed and purified by amylose affinity purification by Dr. Castro Forero using the

periplasmic and cytoplasmic recombinant systems, respectively. Expression yields were lower in the periplasmic system compared to that observed in the cytoplasmic system. Furthermore, MALDI-TOF analysis of the periplasmically-expressed fusion protein indicated that the mass of the fusion protein was 43,031.9 Da. This value is significantly lower than the predicted molecular weight of the MBP-PilA<sub>20</sub> protein (46,902.6 Da), suggesting that proteolytic cleavage occurred. By contrast, a protein with a mass (47,042.6 Da) similar to that predicted for the MBP-PilA<sub>20</sub> protein expressed with the cytoplasmic system (47,033.9 Da) was detected by SDS-PAGE, Western blot and MALDI-TOF analyses (Figure 4.6). However, a small band was also observed in Western blots of the cytoplasmically-expressed fusion proteins, whose mass, as estimated by MALDI-TOF analysis, was 43,671 Da (Figure 29). Hence, as in the periplasmic system, proteolytic cleavage likely occurred that truncated the fusion protein.

Despite the non-specific proteolysis observed in the cytoplasmic system, Dr. Angelines was able to cleave the MBP tag at 23°C after a 48 h incubation of the MBP-PilA<sub>20</sub> fusion protein(s) (Figure 30). MALDI-TOF analyses revealed the presence of two peptides in the protease-cleaved samples: one at 4,527.4 Da and the other at 3,563.3 Da. The larger peptide matches well the expected fragment size for the PilA<sub>20</sub> (4,523.9 Da). The smaller peptide, on the other hand, is consistent with a PilA<sub>20</sub> peptide that has lost 8 amino acids at the N-t (Figure 31) hence, a PilA<sub>28</sub> peptide, which has a predicted molecular weight of 3,560.8 Da). This result suggests that the Factor Xa protease cleaved after the arginine in the recognition site as well as after the pilin's native arginine which is located in the eighth position of the PilA<sub>20</sub> peptide. This was confirmed by peptide sequencing of the first 5 amino acids, which produced the sequence V-AYN from the N-terminal end of the cleaved peptide (the lysine in position 2 was not found). Thus, Factor Xa successfully cleaved PilA<sub>20</sub> from the MBP domain but also produced a PilA<sub>28</sub> peptide, which removes amino acids of the pilin critical for electron transfer. Though the two peptides could be separated by HPLC and other techniques, such approaches are time-

consuming, costly, and reduce the yields of the recombinant pilins. Hence, as an alternative approach, I developed a third pilin expression system as described below.

#### **4.3.2.3 Recombinant production of pilins carrying a chitin-binding domain (CBD)**

Similar to the MBP fusion system described above, the Impact™ system utilizes a chitin binding domain (CBD) tag. This protein tag, like MBP, increases the solubility of the recombinant protein and allows for its selective purification using a column packed with a proprietary chitin resin. An advantage of the Impact™ system is that it incorporates an intein in the fusion protein for self-cleavage of the target protein from the CBD tag. Self-excision is induced in the presence of a reducing agent such as DTT and is highly specific to the intein sequence, thereby minimizing the chance for non-specific cleavage at other sites. Self-cleavage with reducing agents also decreases the cost of purification of the recombinant pilins, a factor to consider for applications in industrial settings. In addition, this method produces a recombinant protein free of non-native amino acids due to the utilization of the Sapl enzyme which results in a start codon directly behind the cleavage site.

Thus, I used the Impact system to construct CBD fusion proteins of the PilA peptide (full length) and several truncated pilins (PilA<sub>10</sub>, PilA<sub>19</sub>, PilA<sub>20</sub>, and PilA<sub>22</sub>). The genetic constructs were cloned into plasmid pTYB11 (Table 4.2) and transformed into Rosetta 2(DE3)pLysS *E. coli* cells (Table 4.1). The Rosetta 2 (DE3) cells contain a plasmid, pRARE, that encodes tRNAs for 7 codons rarely used in *E. coli*: AUA, AGG, AGA, CUA, CCC, GGA, and CGG. This strain background is therefore suitable for the efficient expression of foreign proteins. Rosetta 2(DE3)pLysS also contains a plasmid, pLysS, which encodes a T7 lysozyme to decrease the un-induced expression of the fusion construct which is under the control of the T7 promoter.

Dr. Castro-Forero tested the efficiency of the system by comparing the protein profiles of cell extracts from induced and un-induced cultures by SDS-PAGE gels of proteins to demonstrate the expression of the fusion protein for all the recombinant pilins (Figure 32).

Except for the full-length CBD-PilA fusion protein, which was not detected in the induced cultures, all of the truncated pilins fused to the CBD were expressed upon induction (Figure 32). Cultures expressing the CBD-PilA fusion protein also grew to a cell density half that of cultures producing fusions of CBD and truncated pilins. This finding suggests that, even with a large protein tag to increase its solubility, expression of the full-length pilin was toxic to the cells. As such, expression of the full-length pilin was not pursued further.

All of the fusion proteins of CBD and truncated pilins were purified by affinity chromatography using a chitin resin column and the recombinant pilins were subsequently cleaved on the column with the addition of DTT to yield pure recombinant pilins. The cleaved peptides that eluted from the column were examined by Tris-tricine SDS-PAGE, which is better suited to the resolution of small molecular weight peptides and their separation from SDS micelles<sup>170</sup> (Figure 33). Highest yields for recombinant pilins were obtained when cleavage was performed at 23 °C compared to 4 °C (Figure 33). Yields of the 19- and 22-residue truncations (PilA<sub>19</sub> and PilA<sub>22</sub>) were highest, with nearly 100 % of the recombinant pilins being recovered after only 24 h of incubation at 23 °C in the presence of DTT. By contrast, the 10-residue truncation (PilA<sub>10</sub>) was not eluted after 24 h at 23 °C (Figure 33) and it took 72 h of cleavage to recover *ca.* 50% of the truncated pilin from the column. Such prolonged incubation with DTT also led to the clogging of the chitin column, suggesting that once the PilA<sub>10</sub> peptide was cleaved from the CBD tag it aggregated inside the column, preventing its efficient elution and recovery. Recovery of PilA<sub>10</sub> improved when cleavage was performed at 4 °C but additional bands were also observed (Figure 33), indicative of non-specific cleavage. Hence, although computational predictions of the aggregation factor and total hydrophobicity of the PilA<sub>10</sub> suggested it was a suitable truncation for efficient purification, the experimental evidence suggests otherwise. The 20-residue truncation (PilA<sub>20</sub>) could not be recovered at any temperature (Figure 33). Analysis of the amino acid sequence of the PilA<sub>20</sub>, which could not be

cleaved from the CBD domain, revealed an isoleucine in the most N-t position of this pilin, a residue that the manufacturer of the expression system (New England Biolabs Inc.) reports to inhibit DTT-induced cleavage.

#### **4.3.3 Electrochemical characterization of recombinant PilA<sub>19</sub>**

The results presented above indicated that both PilA<sub>19</sub> and PilA<sub>22</sub> pilins can be efficiently expressed as fusion proteins with a CBD tag and recovered as soluble pilin monomers in the presence of DTT (Figure 34). As the PilA<sub>19</sub> pilin is the one with the shortest truncation and therefore carries more of the native amino acids of the PilA pilin, we chose it for further studies. My collaborator, Dr. Angelines Castro-Forero also demonstrated that PilA<sub>19</sub> retains the predominantly  $\alpha$ -helical structure of PilA using circular dichroism<sup>166</sup>, which is required for assembly and conductivity of the pilin assembly<sup>45</sup>. Furthermore, she demonstrated that this truncated pilin can be assembled *in vitro* into pilus fibers that are otherwise indistinguishable from the native fibers by both transmission electron microscopy (TEM) and atomic force microscopy (AFM)<sup>166</sup>. Furthermore, scanning tunneling microscopy (STM) demonstrated that PilA<sub>19</sub> fibers are conductive and have topographic and electronic features similar to those observed in the native pili<sup>18</sup>. Hence, I used PilA<sub>19</sub> as a model pilin to investigate the intramolecular charge transport of the pili.

##### **4.3.3.1 Functionalization of PilA<sub>19</sub> with a cysteine tag and construction of pilin-electrode interfaces**

Addition of a cysteine residue to a protein enables its attachment to gold surfaces via interaction with the sulfhydryl group<sup>171</sup>. Therefore, an amino acid replacement was introduced into a PilA<sub>19</sub> construct, whereby the codon for the N-t alanine (A20) was mutated to encode a cysteine (A20C), thus generating a PilA<sub>19</sub> peptide carrying an N-t cysteine (PilA<sub>19</sub>-A20C). My collaborator, Dr. Castro-Forero, confirmed that the functionalized pilin can be expressed as a

fusion protein with a CBD in *E. coli*, as described above, and purified from a chitin column after inducing self-cleavage with DTT (Figure 34). Furthermore, MALDI—TOF MS analysis confirmed the presence of a 4,632.3 Da peptide, similar to the predicted molecular weight of 4,627.1 Da. Furthermore, she also confirmed that the PilA<sub>19</sub>-A20C monomers can be assembled *in vitro* into pilus fibers<sup>166</sup>.

I used the PilA<sub>19</sub>-A20C monomers to develop protocols for their deposition as a monolayer on gold electrodes. The pilin monolayer formed on gold electrodes had an average thickness of 37.11 ( $\pm$  7.89 Å) as measured by ellipsometry. As the predicted length of the PilA<sub>19</sub>-A20C pilin is approximately 55 Å, the thickness of the peptide monolayer is consistent with a peptide tilt angle of 42° with respect to the gold support, which is similar to the values reported for other  $\alpha$ -helical peptides attached to gold electrodes<sup>172,173</sup>.

#### 4.3.3.2 Cyclic voltammetry of pilin-electrode interfaces

The ability of the pilin (PilA<sub>19</sub>-A20C) monolayer to transfer electrons between a soluble mediator (ferricyanide) and the underlying electrode was investigated by cyclic voltammetry (CV) (Figure 35). For these experiments, I used pilin samples directly eluted from the chitin columns, which contained DTT and pilin samples dialyzed to remove the DTT. This allowed me to assess if the DTT in the solution affected the formation of sulfhydryl bonds between the pilin and the electrode, which could potentially reduce the monolayer coverage and leave areas of gold exposed to the solution and electrochemically interacting with the ferricyanide. As controls, I also obtained cyclic voltammograms for bare gold electrodes (positive control) and gold electrodes coated with an insulating layer of an undecanethiol self-assembled monolayer (SAM), which insulates the electrode (negative control) (Figure 35). Cyclic voltammograms for electrodes with PilA<sub>19</sub>-A20C were similar to those with bare gold, consistent with a conductive peptide monolayer. However, incubation of the PilA<sub>19</sub>-A20C monomers and the electrode in the presence of the reducing agent DTT, prevented the attachment of the pilins to the gold

electrode. This was demonstrated by the decrease of current density when 1-undecanethiol was layered on top of the pilin monolayer. This decrease was comparable to levels of a gold electrodes coated with 1-undecanethiol (Figure 35). This result demonstrates that a complete pilin monolayer was not achieved. Less of an effect upon 1-undecanethiol addition was observed when the recombinant pilins were dialyzed two times anaerobically to remove the DTT (Figure 35). Furthermore, a buffer exchange into acetonitrile resulted in a CV curve that was of similar height and shape to one with 1-undecanethiol added, demonstrating a fully established SAM (Figure 36). However, the current density of the pilin monolayer formed on the gold electrode did not decrease after adding the insulating 1-undecanethiol, indicating that the monolayer covered the electrode in its entirety. Hence, the results suggest that the PilA<sub>19</sub>-A20C peptide is conductive; consistent with computational predictions of an intramolecular electron transfer pathway in *G. sulfurreducens* nanowires<sup>45,137</sup>.

In all cases, pilin monolayer formation was completed after 48 h (Figure 37). Initial tests showed a decrease in current with longer incubation times, most likely due to oxygen leaking into the pressure vials over time, so further experiments were performed in an anaerobic chamber. The effect of mixing the PilA<sub>19</sub>-A20C solution during deposition on the electrodes was also investigated and found to have no effect (Figure 38). Cyclic voltammograms of 30-day old pilin-electrode interfaces were also similar to those formed after a fresh monolayer deposition (Figure 38). Similarly, lowering the concentration of the pilins in solution or depositing the pilins at lower (4 °C) temperatures did not affect the current response (Figure 39).

#### **4.3.3.3 CP-AFM probing of pilin-electrode interfaces**

As a complementary approach, I used conductive probe atomic force microscopy (CP-AFM) to directly measure the conductivity of the pilin monolayer formed on gold electrodes. Results were variable, but applying a high force allowed the conductive tip of the AFM to penetrate the pilin monolayer and directly transfer electrons to and from the gold electrode. At

very low pressures the pilin monolayer prevented the transfer of electrons, indicating that the monolayer was insulating the tip from the electrode. However, applying forces between these 2 extremes resulted in a current response from the pilin molayer, and resulted in sigmoidal current-voltage (*IV*) plots typical of semi-conductor materials (Figure 40).

The ability of the recombinant pilins to bind to gold electrodes shows promise for the study of pilin conductivity as well as serving as the starting point for the generation of new bioelectronics.

#### ***4.3.4 Intramolecular pilin pathway investigated in mutated pilin-electrode interfaces***

In order to investigate the roles of certain amino acid residues on the intramolecular conductivity of the pilin, I generated mutants encoding CBP fusions of PilA<sub>19</sub>-A20C carrying alanine replacements in amino acids that molecular modeling<sup>45</sup> as well as my previous studies implicated in the conductivity of the pilin. As mentioned previously, the pilin has a unique structure with a strong dipole across the length of the polypeptide. This charge differential contributes to the low electronic band gap estimated for the pilin<sup>45</sup>, increasing its conductivity. Also, aromatic residues located in the charged regions were implicated previously<sup>137</sup> (and in Chapters 2 and 3) in electron transfer. Thus, I constructed PilA<sub>19</sub>-A20C derivatives carrying alanine replacements in the pilin's three tyrosines (Tyr3) and the two aspartic acid residues that influence the aromatic residue configuration and electron transfer through the pili (Asp2)<sup>137</sup>. Additionally, I also constructed an R28A derivative, to investigate the role of positive charges in intramolecular electron transfer.

I expressed and purified the Tyr3, Asp2, and R28A PilA<sub>19</sub>-A20C pilins, as described for the PilA<sub>19</sub>-A20C peptide, and used them to form monolayers on a gold electrode. Undecanethiol was used to cover and insulate areas of the electrode that could have remained uncovered. Interestingly, cyclic voltammograms were similar for all the monolayers (Figure 41), indicating that all samples cycle electrons between the ferricyanide and the underlying gold electrode at

similar rates. This finding suggests that intramolecular electron transfer is not influenced by the tyrosines or the electrostatics contributed by the charged amino acids mutated in the Asp2 and R28A mutants. This does not rule out that intramolecular electron hopping operates in the pilins, because two aromatic residues (phenylalanines) are still present in the pilins. Furthermore, charged amino acids are still present in the mutated pilins, which still contribute to the peptide's dipole. Hence, more aggressive replacements may be needed to see an effect in electron transfer using this approach.

Additionally, charge transfer via hopping may be occurring across the amide groups of the peptide backbone particularly in helical peptides<sup>156</sup> and without contributions from specific amino acids, which only play a role once the pilins assemble and intermolecular electron transfer is necessary. Charge hopping has been demonstrated in  $\alpha$ -helical peptides significantly longer than the *G. sulfurreducens* pilin peptide<sup>68,88</sup>. The rate of charge transfer may increase beyond that observed with the natural dipole moment of the helical peptide<sup>67,108,109</sup>, due to the accentuated dipole in the geopilin (Figure 2). The hydrogen bonding as well as the natural flexibility of  $\alpha$ -helices is also predicted to increase charge transfer rates<sup>112,113,115,116,157,158</sup>.

Finally, it is important to note that the dipolar distribution of charges in the pilin, along with the flexible nature of a relatively long  $\alpha$ -helix that also contains a kink caused by a proline at position 22<sup>49,55</sup>, could have prevented the formation of a monolayer dense enough so as to prevent the penetration of the soluble ferricyanide and interactions with the underlying gold electrode.

#### **4.4 Conclusions**

A soluble, truncated pilin derived from the PilA peptide of *G. sulfurreducens* pilin and termed PilA<sub>19</sub> was successfully expressed in *E. coli* as a fusion protein with a chitin-binding domain using the Impact<sup>TM</sup> system. This expression system also enabled the purification of the

fusion protein in a chitin column and the cleavage and purification of PilA<sub>19</sub>. In collaboration with Dr. Castro-Forero, we used this pilin to assemble conductive pili *in vitro*.

I also constructed a PilA<sub>19</sub> derivative carrying a cysteine at the N-terminus and used it to deposit the PilA<sub>19</sub> as a monolayer on a gold electrode. The pilin monolayer was confluent and prevented the smaller, nonconductive 1-undecanethiol from attaching to the gold electrode. Due to the lack of a redox-active center in the pilin itself I was unable to measure current transferred directly through the pilin. Nevertheless, I demonstrated electron transfer between ferricyanide and the electrode mediated by the pilin monolayer. Though promising, more studies are needed to demonstrate that the PilA<sub>19</sub> monolayer is impermeable to solutes, such as ferricyanide, and to validate the CV approach as a method to measure pilin-mediated ET. Electrochemical techniques such as impedance spectroscopy could be used to test for the presence of pinholes or defects in the monolayers<sup>174</sup>. Similar approaches have been used to demonstrate, for example, that alkanethiol SAMs, such as the 1-undecanethiol preparation utilized in this study, limit access of molecules in solution to the electrode<sup>174</sup>. As the pilins are significantly larger and have a more complex structure than an alkanethiol, and are also charged, it is possible that pilin monolayers cannot be formed that are dense enough to exclude ferricyanide. If so, alternative approaches, such as the CP-AFM approach I used, may be needed to investigate the conductivity of the pilin monolayer and to assess the contribution of amino acid replacements to intramolecular ET.

Finally, the possibility of using PilA<sub>19</sub> to produce conductive fibers *in vitro* shows promise as a tool to investigate the contribution of specific amino acids of the pilin to charge transport. These experiments, coupled to CP-AFM measurements of intramolecular charge transport through the pilin monolayers could help dissect the electron transfer pathways that allow the pili to function as protein nanowires. ET through  $\alpha$ -helical peptides has been directly measured by molecular junction experiments where  $\alpha$ -helical peptides were similarly deposited on a gold

electrode<sup>87,172,173,175</sup>. A cysteine residing on the opposite end of this  $\alpha$ -helical peptide then interacts with the tip of the conductive probe of a scanning tunneling microscope or current-sensing AFM to measure electron transfer through the peptide. These studies have shown that small  $\alpha$ -helical peptides are often able to transfer electrons and that the transfer is favored in one direction<sup>175,176</sup>. This ET is thought to involve the transfer of electrons directly through the peptide backbone, and is facilitated by the secondary structure and the dipole created by the N-terminal amine and C-terminal carboxylic acid<sup>69</sup>. The use of these pilin monolayers in CV experiments may also be possible by directly binding a redox active ferrocene molecule to the peptide<sup>68,88</sup>. This would allow us to determine the conductivity of the pilin itself, and thus its intramolecular charge transfer capabilities. Since I am now able to produce a uniform monolayer with the PilA<sub>19</sub>-A20C pilins, the packing should be tight enough such that no ferrocene units will directly interact with the gold electrode. As a result, the only CV signal produced would be generated from the electrons moving from the ferrocene to the gold through the pilin backbone.

## **CHAPTER 5. Conclusions and Future Directions**

## **5.1 Review of project**

The elucidation of both the role of the conductive *G. sulfurreducens* pilus nanowires and the method of electron transfer (ET) are of great importance to the study of *Geobacteraceae* and their roles in dissimilatory metal reduction, performance of microbial electrochemical cells, and bioremediation of toxic metals and organic pollutants. Furthermore, the identification of conductive pili in these organisms provides a new paradigm in protein ET and may prove instrumental to discover other protein-mediated mechanisms for long distance ET in other organisms in the emerging field of electromicrobiology. From a practical point of view, studies such as those I presented in this dissertation provide the foundation for applications of protein nanowires in nanotechnology, sensor design, and bioremediation, for improving the performance of microbial electrochemical cells such as microbial electrolysis cells (MECs), and for developing more efficient schemes for the environmental restoration of environments impacted with metal contaminants.

### **5.1.1 Review of mechanistic stratification in electroactive biofilms of *Geobacter sulfurreducens* mediated by pilus nanowires**

In Chapter 2, I took a genetic approach to investigate the role of pilus nanowires in electroactive biofilms using the model representative bacterium *G. sulfurreducens*. I constructed several pilus-deficient mutants and identified one (pilB, which carried a deletion in the PilB ATPase that energizes pilin assembly) with no apparent defects in *c*-type cytochrome production or localization. This mutant provided the elusive genetic tool that prevented other studies from conclusively linking electrochemical signatures of anode biofilms of *G. sulfurreducens* to the pilus conductivity. The pilB mutant had, for example, a *ca.* 50 % reduction in current production in thin biofilms and was unable to grow biofilms thicker than *ca.* 10  $\mu\text{m}$ . The defect was the direct result of a reduced ability of the cells to efficiently transfer electrons

across the biofilms because a mutant that produced pili with increased resistance to the passage of electrons (Tyr3) had the same phenotype. I also demonstrated that thick anode biofilms are stratified in terms of their mechanism of ET, with the bottom stratum (ca. 10  $\mu\text{m}$  thick) requiring the coordinated activity of pili and matrix-associated *c*-type cytochromes such as OmcZ, and the conductive pili being essentially for growth and electrochemical activity of biofilm cells growing beyond this threshold thickness.

### ***5.1.2 Review of site-directed mutagenesis reveals a role of aromatic amino acids and local electrostatics in pilus conductivity and extracellular electron transfer***

I was able to identify amino acid residues of the pilin monomer that were essential for pilus conductivity *in vivo* and *in vitro*. Substitution of a single tyrosine residue, Y27, resulted in a 4.5 to 5.5 increase in resistance to the passage of electrons along the length of the pilus. This change in residue, however, did not affect the ability of Y27A mutant cells to produce current in acetate-fed MECs or reduce Fe(III) oxides. Hence, while Y27 is necessary for optimal charge transport *in vitro*, the defect is not rate-limiting *in vivo*, where the rates of acetate oxidation limit growth. However, substitution of each of the remaining tyrosine residues (Y32 and Y57) in the Y32A and Y57A variants reduced the performance of the anode biofilms in acetate-fed MECs to levels comparable to the Tyr3 mutant. The exposure of these two tyrosines on the pilus surface suggests that they play a critical role in ET to the matrix-associated *c*-type cytochromes. I also demonstrated that the phenotypic defects of the Tyr3 mutant in anode biofilms can be rescued when phenylalanines, rather than alanines, are used to replace the pilin's three tyrosines. This result suggests that phenylalanine residues can also transfer electrons between the pili and matrix-associated *c*-type cytochromes. Furthermore, the result suggest that post-translational modifications of the pilin's tyrosines, if they exist, are not essential for current production in MECs. By contrast, a double aspartic acid mutant (D53A D54A or Asp2) had a severe defect in ET to both Fe(III) oxides and across anode biofilms. The Asp2 phenotype thus validates

predictions from a molecular dynamics (MD) model of the pilus generated by our collaborator, Dr. Feliciano, which indicated that the local electrostatic environment around the aromatic ring contacts in the Asp2 pilus influences the packing and configuration of the aromatic residues and, in turn, ET.

### **5.1.3 Review of intramolecular charge transport in pilus nanowires investigated in pilin-electrode interfaces**

Analysis of the MD model of the pilus revealed intermolecular and intramolecular interactions between aromatic residues of the pilins and also identified pathways for intramolecular ET via the peptide's amide backbone<sup>137</sup>. Furthermore, the steep dipolar landscape of the pilin has been proposed to promote intramolecular ET as well<sup>45</sup>. Thus, in chapter 4, I tested the hypothesis that the pilin, by itself, conducts electrons. To test this hypothesis, I constructed pilin monolayers attached to gold electrodes and used cyclic voltammetry to investigate if the pilins could cycle electrons between the underlying gold electrode and ferricyanide in the medium. To do this, I first constructed truncations of the pilins and tested several expression systems to identify one that enabled its production and purification in the quantities needed for my experiments. This part of the work was part of a collaboration with Dr. Angelines Castro Forero, who used the truncated pilins to assemble protein nanowires *in vitro*<sup>166</sup>. Together, we selected a construct and expression system that allowed us to produce a recombinant PilA<sub>19</sub> pilin with high yields and assembled a set of these into conductive PilA<sub>19</sub> pili. I then constructed a PilA<sub>19</sub> derivative carrying a cysteine at the N-terminus (PilA<sub>19</sub>-A20C) for deposition on a gold electrode. In Chapter 4, I demonstrated that it is possible to deposit a confluent pilin monolayer on gold electrodes. Using insulating self-assembled monolayers (SAMs) of undecanethiol as controls, I demonstrated that the pilin monolayer functioned as a mediator for electrons between ferricyanide and the underlying electrode surface. I did not observe any change in electron cycling using pilin monolayers

carrying amino acid replacements in the three tyrosines (Tyr3 mutant), the two D53 and D54 residues (Asp2 mutant), or the positively-charged amino acid R28 (R28A mutant). The results thus indicate that the pilins have paths for intramolecular ET, but these pathways do not involve amino acids that are needed for ET once the pilins assemble to form the pilus fiber. This finding suggests that aromatic residues need to cluster in the pilin assembly to create paths for ET and charged amino acids influence the rates of ET via aromatic residues because they are positioned in the assembly close enough to the aromatic rings to provide the local electrostatic environment required for optimal ET. The results also indicate that charge hopping within the peptide backbone is the predominant mechanism for intramolecular ET.

## **5.2 Future directions**

### **5.2.1 Future directions for studying mechanistic stratification in electroactive biofilms of Geobacter sulfurreducens mediated by pilus nanowires**

In Appendix 1 I showed that it is possible to increase the thickness of pilB biofilms growing on anode electrodes after successive transfers of the anode biofilms into fresh medium. Furthermore, I also documented occasional increases in current production in this strain. This result suggests that compensatory mechanisms exist to overcome the pilus deficiency though they are not as efficient as those provided by the conductive pili. Future work could, for example, investigate if the type and/or quantity of c-type cytochromes in the biofilm matrix have changed so as to promote ET in thick biofilms despite the lack of pili. Alternatively, pili-like filaments may have been assembled that provide structural support to the biofilms, allowing them to grow in thickness and, perhaps, conduct electrons. Such compensatory mechanisms may be similar to those reported for a pilin-deficient strain, which appears to produce pili-like filaments at some low frequency<sup>177</sup> and can be adaptively evolved to grow in Fe(III) oxides by secreting a small c-type cytochromes that functions as an electron shuttle<sup>178</sup>. Finally, it is still not

clear how pili and *c*-type cytochromes coordinate their activities in the bottom stratum of the biofilm or what is the exact role of cytochromes in the outer layers of the biofilm; these questions should be further investigated. Electrochemical characterization of the pilB mutant and other mutants I constructed and characterized will prove instrumental to answering these outstanding questions.

### ***5.2.2 Future directions for site-directed mutagenesis to reveal the role of aromatic amino acids and local electrostatics in pilus conductivity and extracellular electron transfer***

In Chapter 3, I demonstrated that defects in pilus conductivity do not necessarily translate to changes in biological phenotypes associated with pilus function. Still, many questions remain unresolved. For example, why Y27 is not critical to current production in MECs but Y32 and Y57 are. The conductivity of the Y32A and Y57A mutant pili has never been examined and could help explain the observed phenotypes. Y27A pili on the other hand, were defective in charge transport but performed like the WT in the MECs. However, there may exist a minimum charge transfer rate that allows the pili to grow thick, electroactive biofilms that can only be achieved when certain amino acids are present in the pilus ET pathway. Increasing the sensitivity of the CP-AFM measurements to unmask phenotypes at the low voltages that operate in the cells may also prove instrumental to understand their role in ET. Furthermore, their role in ET to *c*-type cytochromes and other pili also needs to be evaluated.

Future work will also need to evaluate how these mutations affect the binding of metals such as oxidized iron and uranium. The MD model predicts that the tyrosines exposed on the pilus surface will be the ones mediating the final step in ET to external electron acceptors. Furthermore, negatively-charged ligands in the C-t random coils of the pilins could form a metal “cage” for efficient binding of the metals and positioning them close enough to the exposed aromatic residues for efficient ET. Finally, the role of post-translational modifications of the pilin warrants attention. Tyrosine residues are post-translationally modified in other bacterial pilins

and influence the binding properties of the pili<sup>70,73,179</sup>. I showed that phenylalanine replacements of the the pilin's three tyrosines (Tyr3-F mutant) do not affect the electrochemical activity of the anode biofilms. Hence, post-translational modifications of the pilin, if they exist, are not critical to pili functions in the electroactive matrix. However, post-translational modifications could influence the binding of metals such as iron and uranium. If so, Tyr3-F pili are expected to have defects in metal binding and perhaps also in their reduction.

Lastly, it is important to construct atomic or pseudoatomic structural models of the pili based on experimental validated structures or, in lieu of this, to further refine the MD pilus model to provide information about the electronic structure of the pili. An electronic structural model will allow one to make further predictions about the roles of specific residues in ET, which could be tested experimentally by *in vitro* and *in vivo* assays. The MD model that I experimentally tested in Chapter 3 suggests that small perturbations in protein structure, such as those resulting from the Asp2 mutation, influenced the configuration of the aromatics and ET. Phenylalanine residues are common replacements for tyrosine or tryptophan residues to minimize structural changes in proteins<sup>180,181</sup>. However, such substitutions also removed the hydroxyl group in tyrosines, which could have affected the structure of the pilin and the number and configurations of the contacts. Hence, it will be important to introduce the Tyr3-F mutation in the MD model and investigate how the pilus structure is affected.

The contribution of PCET to pilus ET also needs to be studied. While the Tyr3-F had no observable phenotype in the MECs, the pilus conductivity may have been affected, as we observed in the Y27A mutant. If so, the pH dependence of the conductivity of the Tyr3 and Tyr3-F pili *in vivo* and *in vitro* could elucidate whether the tyrosines are involved in PCET. In addition, chemical complementation of the mutant anode biofilms in MECs or in Fe(III) oxide cultures could be attempted. Chemical complementation of a histidine proton acceptor mutant with imidazole has been demonstrated previously<sup>95</sup>. Changing the buffering capacity of the medium

or directly measuring the pH in a biofilm would also help us to investigate the role of PCET<sup>182</sup>. Bulk conductivity measurements on the pili, such as CV, can be performed in solution, and therefore, direct effects on chemical complementation or buffering capacity on conductivity can be measured.

### **5.2.3 Future directions for examining intramolecular charge transport in pilus nanowires via pilin-electrode interfaces**

In Chapter 4, I demonstrated that it is possible to deposit confluent pilin monolayers of the PilA<sub>19</sub>-A<sub>20C</sub> peptide that prevent the small 1-undecanethiol molecule from attaching and insulating the electrode. Furthermore, thickness measurements consistently indicated that the pilins are packed at a 40 ° tilt in the monolayer. Hence, these nanostructured interfaces show promise as a tool to investigate intramolecular ET through the pilin peptide. Future directions could focus on improving the sensitivity of the assays so as to unmask potential conductivity changes in the peptide due to single amino acid replacements. One way to do this is to rule out that the soluble ferricyanide is not leaking through the pilin monolayer and artifactually enhancing the cyclic voltammograms. Similar to other small conductive peptides, the pilin does not produce its own redox peaks, and therefore, a direct measurement of the conductivity of the pilin is not possible. For this reason, my assays investigated the conductivity of the pilin monolayer through its ability to cycle electrons between ferricyanide and the gold electrode. However, ferrocene could be covalently attached to the pilin's C-terminus to sensitively measure ET across the pilin monolayer. In this interface, cyclic voltammograms would reflect direct ET from ferrocene to the electrode through the pilins only. This system could also be adapted to investigate the binding affinity of the pilins for metals such as iron and uranium and to test the effect of targeted amino acid replacements on ET to specific metals. Such interfaces could be the foundation of larger interfaces for the remediation and/or reclamation of metals and for the development of metal sensors.

Direct conductivity measurements of the pilin monolayers with CP-AFM also show promise as a tool to investigate intramolecular ET via pilins. AFM-based approaches or other methods also need to be developed to determine how tightly packed the pilins are, as the packing of peptides in a monolayer is predicted to affect charge transfer<sup>183,184</sup>.

Lastly, the possibility of assembling the same recombinant pilins as conductive pili can be used as a complementary tool. The conductivity of the synthetic pili produced with recombinant pilins integrates intermolecular and intramolecular ET pathways, whereas the pilin-electrode interfaces isolate the intramolecular path only. Furthermore, synthetic pili do not contain any post-translational modifications, whereas native pili (i.e., purified from *G. sulfurreducens*) do. Hence, the three systems are complementary and provide the necessary tools to dissect the complex pilus system and potential ET pathways.

## **APPENDICES**

***APPENDIX A***

MEC ADAPTATION IN PILB MUTANT STRAIN

## **Abstract**

The effect of nutrient availability and/or accumulation of toxic metabolic products was tested in pilB-driven microbial electrochemical cells (MECs) to rule out any influence in the mutant phenotype. I also performed adaptive evolution experiments to investigate the stability of the pilB mutant phenotype. The results suggest that the pilB mutant biofilms can grow to WT thicknesses after repeated transfers of the anode biofilms to MECs with fresh medium and even increase their current production, though never to the levels observed in the WT MECs.

## **Introduction**

In Chapter 2 I demonstrated that the pili-deficiency of the pilB mutant prevented it from growing biofilms beyond a threshold thickness (ca. 10  $\mu\text{m}$ ) and also reduced the rates of current increase and maximum current. Here, I describe experiments that tested whether growth was limited by a component of the media (i.e., nutrient availability and/or accumulation of toxic byproducts of the cells' metabolism). I also investigated the ability of the pilB mutant to adapt to and overcome the biofilm growth limitation in MECs.

## **Materials and Methods**

### **Testing media components in MECs**

MEC experiments were performed as in Chapter 2 and contained 1 mM acetate. The WT strain of *G. sulfurreducens* was grown on the anode electrode of the MECs until maximum current was reached and current began to decrease (deceleration phase), different media components were added to determine if their availability could restore maximum levels of current production. I tested acetate, vitamins, minerals, and salts.

## Sequential transfers of anode biofilms in MECs

Anode biofilms of the WT, pilB, and omcZ strains were grown in MECs with 3 mM acetate. Once all of the acetate was depleted and current had decreased to < 0.1 mA, the MECs were taken into an anaerobic chamber (COY Labs) to rinse the anode chamber with ddH<sub>2</sub>O, and replenish it with fresh media containing 3 mM acetate.

## Results

To determine if a component of the media was limiting in the pilB MECs, acetate, mineral mix, vitamins, or media salts were added to the MEC when current began to decrease (about 32 h) (Figure 42). Addition of the vitamin mix had no effect on current, but supplementing the anode medium with the electron donor (3 mM acetate) restored current production to the original maximum current levels. Current production plateaued at this level for a length of time similar to that of control pilB MECs fed 3 mM acetate from the beginning (Figure 42) Once current production declined, I supplemented the anode medium with a second dose of 3 mM acetate but the deceleration phase continued. Media supplementation with mineral mix, salts, or vitamins had no effect either, suggesting that other factors limited the growth and electroactivity of the biofilms.

To determine if the production of a waste product was participating in the pilB phenotype, the medium was replaced after the culture had consumed 3 mM acetate. With the media replacement, a slight increase in current was seen for the pilB strain; however with fresh media and the biofilm previously formed on the anode, the current still plateaued at a value considerably lower compared to the WT culture (which produce 2.3 mA of current).

It has been reported that pili-deficient strains of *G. sulfurreducens*, which cannot reduce Fe(III) oxides optimally, can bypass the limitation by adaptively evolving alternative mechanisms<sup>178</sup>. Thus, I investigated whether the pilB strain was able to adapt under selective pressure to form thick biofilms and produce current in MECs. To do this I sequentially replenish

the anode medium with fresh medium up to 10 times. Interestingly, both the WT and the pilB biofilms grew to more than 50  $\mu\text{m}$  thicknesses after 10 sequential media transfers. Hence, pilB biofilms can bypass the pilus deficiency and grow thicker biofilms under selective pressure to couple the oxidation of acetate to current production. As for the effect on current production, I observed two different phenotypes. Current in some of the pilB-driven MECs remained low (less than 1 mA) throughout the experiment, but increased above 1 mA in some of the MECs after multiple medium replacements (Figure 43). Such increases are still low compared to those observed in the WT strain, which reached ca. 5 mA of maximum current, and much higher than controls with the omcZ mutant (Figure 43). Yet they suggest that there are compensatory mechanisms that allow the cell to bypass the pili deficiency. If, as reported<sup>178</sup>, a soluble cytochrome can be produced to bypass the pilus deficiency and shuttle electrons between the cell and insoluble electron acceptors, pilB cells could grow in anode biofilms by discharging respiratory electrons to the shuttle. However, it is unlikely that this cytochrome can effectively shuttle electrons between the cells and the electrode, explaining the inability of the pilB mutant to produce current at WT levels.

## Conclusions

There are several reasons why *G. sulfurreducens* biofilms might stop producing current in an MEC (e.g., depletion of a required nutrient and buildup of a toxic byproduct). To determine if limitations in current production was due to acetate limitation or the buildup of waste productions, MEC experiments were performed in which the media in the MEC was replaced after the culture had stopped producing current. Initially, addition of acetate was sufficient to restore current production, but not to provide any increase in current, however, current production could not be rescued by addition of any media component. This result suggested that there was a buildup of a toxic byproduct that upon removal allowed the restoration of current production. Replacing the anode medium with fresh medium once acetate had been

depleted, allowed us to adaptively grow thicker (ca. 50  $\mu\text{m}$ ) biofilms of both the WT and pilB strains after 10 sequential media transfers. Current increased over 1 mA in some of the pilB-driven MECs but never to WT levels, supporting our model (Chapter 2) that the pili are required for optimal electron transfer in anode biofilms. The mechanism by which pilB mutants were able to grow thick biofilms without changing current production has yet to be determined.

***APPENDIX B***

TABLES

Table 1 Strains and plasmids used in Chapter 2

Bacterial strain or plasmid	Relevant genotype and properties <sup>a</sup>	Source or reference(s)
<b><i>Geobacter sulfurreducens</i></b>		
WT	Wild type strain PCA	19
pilA	$\Delta pilA::aaaC1$ , Gm <sup>r</sup>	This study
pilB	$\Delta pilB::aaaC1$ , Gm <sup>r</sup>	This study
omcZ	$\Delta omcZ::aaaC1$ , Gm <sup>r</sup>	This study
pilA-E5A	$pilA^{E5A}::aadA$ , Spec <sup>r</sup>	This study
$\Delta pilB$	$\Delta pilB::loxP$	This study
pilB+	$\Delta pilB$ complemented with pRG5- <i>pilB</i>	This study
pilB gspE	$\Delta pilB$ strain carrying the $\Delta gspE::aaaC1$ mutation, Gm <sup>r</sup>	This study
pilB mshE	$\Delta pilB$ strain carrying the $\Delta mshE::aaaC1$ mutation, Gm <sup>r</sup>	This study
Tyr3	$pilAY27,32,57A::aadA$ , Spec <sup>r</sup>	This study
<b>Plasmids</b>		
pCM351	Amp <sup>r</sup> , Tet <sup>r</sup> , Gm <sup>r</sup> , ColE1 <i>ori</i> , <i>oriT</i>	123
pCM158	Km <sup>r</sup> , <i>trfA</i> , <i>oriT</i> , <i>oriV</i> , ColE1 <i>ori</i> , <i>cre</i>	123
pCR2.1-TOPO	Amp <sup>r</sup> , Km <sup>r</sup> , ColE1 <i>ori</i>	Invitrogen
pRG5	Shuttle vector for <i>G. sulfurreducens</i> Spc <sup>r</sup> , P <sub>taclac</sub>	124
pRG5- <i>pilB</i>	pRG5 with <i>G. sulfurreducens pilB</i>	This study

Table 2 Primers used in Chapter 2

Primer	Sequence (5'-3')	Amplification	Use
RS1	GATCTGGTCGGATAACAACACC	<i>pilB</i> upstream	<i>pilB</i>
RS2	TTATGCGGCCGCCATATGCATCTGCTAGCCTGCATAGACTCTCC	<i>pilB</i> upstream	<i>pilB</i>
RS3	GTGTTAACCGGTCATATGCAGTGGCTGACGACTAAACAAAATGCC	<i>pilB</i> downstream	<i>pilB</i>
RS4	CTCTTGTGAGGATGCAGGTAC	<i>pilB</i> downstream	<i>pilB</i>
RS5	ATGGACCTCGAAGCCTACCT	<i>pilA</i> upstream	<i>pilA</i>
RS6	TTATGCGGCCGCCATATGCATCTGAAGCATAAGTG	<i>pilA</i> upstream	<i>pilA</i>
RS7	GTGTTAACCGGTCATATGCACGCCCGAAAGTTAA	<i>pilA</i> downstream	<i>pilA</i>
RS8	TCCATGCATCATTTTTCGATG	<i>pilA</i> downstream	<i>pilA</i>
RS9	ATATGGCGTTTACCGCAGAG	<i>omcZ</i> upstream	<i>omcZ</i>
RS10	TTATGCGGCCGCCATATGCAGCTCCGAAGAAAGTCAAACG	<i>omcZ</i> upstream	<i>omcZ</i>
RS11	GTGTTAACCGGTCATATGCAGATGCGCCAATCAGTACCTT	<i>omcZ</i> downstream	<i>omcZ</i>
RS12	CACAGCCAGGTACCATCTGA	<i>omcZ</i> downstream	<i>omcZ</i>
RS13	TTTCTCAGCAATCCATCGAG	<i>gspE</i> upstream	<i>pilB gspE</i>
RS14	TTATGCGGCCGCCATATGCAATCTGTTCCATGTCGTGTGC	<i>gspE</i> upstream	<i>pilB gspE</i>
RS15	GTGTTAACCGGTCATATGCAGTATGCCGACCTTCCGGTAT	<i>gspE</i> downstream	<i>pilB gspE</i>
RS16	AGTGATTTTGCTCCGAATGG	<i>gspE</i> downstream	<i>pilB gspE</i>
RS17	TTTCGGCCATGTA <del>CT</del> CCTTT	<i>mshE</i> upstream	<i>pilB mshE</i>
RS18	TTATGCGGCCGCCATATGCATCCTTGACGATGCTTTCCAT	<i>mshE</i> upstream	<i>pilB mshE</i>
RS19	GTGTTAACCGGTCATATGCACTCCTCCCTGCACGGTTGA	<i>mshE</i> downstream	<i>pilB mshE</i>
RS20	CGACATCTTGTTCTCGTGGA	<i>mshE</i> downstream	<i>pilB mshE</i>
RS21	TGCATATGGCGGCCGCATAA	<i>aaaC1 loxP</i>	Excible Gm marker
RS22	TGCATATGACCGGTTAACAC	<i>aaaC1 loxP</i>	Excible Gm marker
RS23	GTGGTGAAGGGGTAGGTTGA	<i>pilA</i> upstream	<i>pilA::aadA</i>
RS24	GTTAGGCGTCATCCTGTGCTTAAC <del>TT</del> TCGGGCGGATAGG	<i>pilA</i> upstream	<i>pilA::aadA</i>
RS25	CAAGCCGACGCCGCTTCTTGATTA <del>AA</del> TACATACTGGAGG	<i>pilA</i> downstream	<i>pilA</i> -Sp
RS26	GCGACTTCCACTCGGTACC	<i>pilA</i> downstream	<i>pilA</i> -Sp
RS27	GCACAGGATGACGCCTAAC	<i>aadA</i>	Sp marker
RS28	GAAGCGGCGT <del>CG</del> GCTTG	<i>aadA</i>	Sp marker
RS29	GGTTTACCCCTTATC <del>GG</del> CTGCTGATCGTCGTT	<i>pilAE5A::aadA</i>	<i>pilA</i> -E5A
RS30	AACGACGATCAGCAG <del>CG</del> CGATAAGGGTGAAACC	<i>pilAE5A::aadA</i>	<i>pilA</i> -E5A
RS31	TCCGCAGTTCTCGGCG <del>GCT</del> CGTGTCAAGGCGTAC	<i>pilA</i> Y27A:: <i>aadA</i>	Tyr3

Table 2 (cont'd)

RS32	GTACGCCTTGACACG <b>AGCC</b> GCCGAGAACTGCGGA	<i>pilA</i> Y27A:: <i>aadA</i>	Tyr3
RS33	GTATCGTGTCAAGGCG <b>GCC</b> AAACAGCGCGGCGTC	<i>pilA</i> Y32A:: <i>aadA</i>	Tyr3
RS34	GACGCCGCGCTGTT <b>GGC</b> CGCCTTGACACGATAC	<i>pilA</i> Y32A:: <i>aadA</i>	Tyr3
RS35	CCGCATTTGCTGATGATCAAACC <b>GCT</b> CCGCCCGAAAGTTAA	<i>pilA</i> Y57A:: <i>aadA</i>	Tyr3
RS36	TTAACTTTCCGGCGG <b>AGC</b> GGTTTGATCATCAGCAAATGCGG	<i>pilA</i> Y57A:: <i>aadA</i>	Tyr3
RS37	CCAACACAAGCAGCAAAAAG	<i>pilA</i>	qPCR
RS38	GCAGCGAGAATACCGATGAT	<i>pilA</i>	qPCR
RS39	ATGGGTGGCAAGGACTTTAC	GSU1497	qPCR
RS40	ACACCCGGTTACCAGAAGAG	GSU1497	qPCR
RS41	GTCCAACAAAGGGAAGTCTGCT	<i>xapD</i>	qPCR
RS42	CCTCCGCAGAGAGGTAATCA	<i>xapD</i>	qPCR
RS43	CACGAGCCTGACACTCACTC	<i>omcZ</i>	qPCR
RS44	AAGGTTGCTGACCTTGTTGG	<i>omcZ</i>	qPCR
RS45	GACACGGTCAACCAGAACAA	<i>omcB</i>	qPCR
RS46	GGTCCCAGTTTACGACAGGA	<i>omcB</i>	qPCR
RS47	AGTTCTCGACGTACGCCACT	<i>rpoD</i>	qPCR
RS48	TCAGCTTGTTGATGGTCTCG	<i>rpoD</i>	qPCR

---

Table 3 Bacterial strains and plasmids used in Chapter 4

Bacterial strain or plasmid	Relevant genotype and properties <sup>a</sup>	Source or reference(s)
<b><i>Geobacter sulfurreducens</i></b>		
WT	Wild type strain PCA	19
Tyr3	<i>pilAY27,32,57A::aadA</i> , Spec <sup>r</sup>	This study
Y27A	<i>pilAY27A::aadA</i> , Spec <sup>r</sup>	This study
Y27F	<i>pilAY27F::aadA</i> , Spec <sup>r</sup>	This study
Y32A	<i>pilAY32A::aadA</i> , Spec <sup>r</sup>	This study
Y57A	<i>pilAY57A::aadA</i> , Spec <sup>r</sup>	This study
Tyr3-F	<i>pilAY27,32,57F::aadA</i> , Spec <sup>r</sup>	This study
Asp2	<i>pilAD53,54A::aadA</i> , Spec <sup>r</sup>	This study
<b>Plasmids</b>		
pCR2.1-TOPO	Amp <sup>r</sup> , Km <sup>r</sup> , ColE1 <i>ori</i>	Invitrogen
pCR2.1-pilASpec	Amp <sup>r</sup> , Km <sup>r</sup> , ColE1 <i>ori pilA::aadA</i> Spec <sup>r</sup>	Chapter 2
pCR2.1-Tyr3	Amp <sup>r</sup> , Km <sup>r</sup> , ColE1 <i>ori pilAY27,32,57A::aadA</i> , Spec <sup>r</sup>	Chapter 2
pCR2.1-Y27A	Amp <sup>r</sup> , Km <sup>r</sup> , ColE1 <i>ori pilAY27A::aadA</i> Spec <sup>r</sup>	This study
pCR2.1-Y27F	Amp <sup>r</sup> , Km <sup>r</sup> , ColE1 <i>ori pilAY27F::aadA</i> Spec <sup>r</sup>	This study
pCR2.1-Y32A	Amp <sup>r</sup> , Km <sup>r</sup> , ColE1 <i>ori pilAY32A::aadA</i> Spec <sup>r</sup>	This study
pCR2.1-Y57A	Amp <sup>r</sup> , Km <sup>r</sup> , ColE1 <i>ori pilAY57A::aadA</i> Spec <sup>r</sup>	This study
pCR2.1-Tyr3-F	Amp <sup>r</sup> , Km <sup>r</sup> , ColE1 <i>ori pilAY27,32,57F::aadA</i> , Spec <sup>r</sup>	This study
pCR2.1-D5354A	Amp <sup>r</sup> , Km <sup>r</sup> , ColE1 <i>ori pilAD53,54A::aadA</i> Spec <sup>r</sup>	This study
pRG5	Shuttle vector for <i>G. sulfurreducens</i> Spc <sup>r</sup> , P <sub>taclac</sub>	124

Table 4 Primers used in Chapter 3

Primer	Sequence (5'-3')	Amplification	Use
RS31	TCCGCAGTTCTCGGCG <b>GCT</b> CGTGTCAAGGCGTAC	<i>pilA</i> Y27A:: <i>aadA</i>	Y27A
RS32	GTACGCCTTGACACG <b>AGC</b> CGCCGAGAACTGCGGA	<i>pilA</i> Y27A:: <i>aadA</i>	Y27A
RS33	GTATCGTGTCAAGGCG <b>GCC</b> AACAGCGCGGCGTC	<i>pilA</i> Y32A:: <i>aadA</i>	Y32A
RS34	GACGCCGCGCTGTT <b>GGC</b> CGCCTTGACACGATAC	<i>pilA</i> Y32A:: <i>aadA</i>	Y32A
RS35	CCGCATTTGCTGATGATCAAACC <b>GCT</b> CCGCCCGAAAAGTTAA	<i>pilA</i> Y57A:: <i>aadA</i>	Y57A
RS36	TTAACTTTCTGGGCGG <b>AGC</b> GGTTTGTATCATCAGCAAATGCGG	<i>pilA</i> Y57A:: <i>aadA</i>	Y57A
RS49	TCCGCAGTTCTCGGCG <b>TTT</b> CGTGTCAAGGCGTAC	<i>pilA</i> Y27F:: <i>aadA</i>	Tyr3-F, Y27F
RS50	GTACGCCTTGACACG <b>AAAC</b> CGCCGAGAACTGCGGA	<i>pilA</i> Y27:: <i>aadA</i>	Tyr3-F, Y27F
RS51	GTATCGTGTCAAGGCG <b>TTC</b> AACAGCGCGGCGTC	<i>pilA</i> Y32F:: <i>aadA</i>	Tyr3-F
RS52	GACGCCGCGCTGTT <b>GAAC</b> GCCTTGACACGATAC	<i>pilA</i> Y32F:: <i>aadA</i>	Tyr3-F
RS53	CCGCATTTGCTGATGATCAAACC <b>TTT</b> CCGCCCGAAAAGTTAA	<i>pilA</i> Y57F:: <i>aadA</i>	Tyr3-F
RS54	TTAACTTTCTGGGCGG <b>AAAG</b> GGTTTGTATCATCAGCAAATGCGG	<i>pilA</i> Y57F:: <i>aadA</i>	Tyr3-F
RS55	GAGTCCGCATTTGCT <b>GCTGCT</b> CAAACCTATCCGCC	<i>pilAD</i> 53,54A:: <i>aadA</i>	D5354A
RS56	GGGCGGATAGGTTT <b>GAGCAGC</b> AGCAAATGCGGACTC	<i>pilAD</i> 53,54A:: <i>aadA</i>	D5354A

Table 5 Strains used in Chapter 4

<b><i>E. coli</i> Strain</b>	<b>Genotype</b>	<b>Reference</b>
M15[pREP4]	Nal <sup>s</sup> , Str <sup>s</sup> , Rif <sup>s</sup> , Thi <sup>-</sup> , Lac <sup>-</sup> , Ara <sup>+</sup> , Gal <sup>+</sup> , Mtl <sup>-</sup> , F <sup>-</sup> , RecA <sup>-</sup> , Uvr <sup>+</sup> , Lon <sup>+</sup> , Kan <sup>R</sup>	Qiagen®
K12 TB1	<i>ara</i> Δ( <i>lac-proAB</i> ) [ <i>Φ80dlac</i> Δ( <i>lacZ</i> )M15] <i>rpsL</i> (Str <sup>R</sup> ) <i>thi</i> <i>hsdR</i>	New England Biolabs Inc.®
Rosetta™ 2 (DE3)pLysS	<i>ompT</i> <i>hsdS</i> <sub>B</sub> (r <sub>B</sub> <sup>-</sup> m <sub>B</sub> <sup>-</sup> ) <i>gal dcm</i> (DE3) pLysSRARE2 (Cam <sup>R</sup> )	Novagen®
DH5α	φ80 <i>lacZ</i> ΔM15 Δ( <i>lacZYA-argF</i> )U169 <i>recA1</i> <i>endA1</i> <i>hsdR17</i> (rk <sup>-</sup> , mk <sup>+</sup> ) <i>phoA</i> <i>supE44</i> <i>thi-1</i> <i>gyrA96</i> <i>relA1</i> λ	Life Technologies Co.®
XL10-Gold	Tetr Δ( <i>mcrA</i> )183 Δ( <i>mcrCB-hsdSMR-mrr</i> )173 <i>endA1</i> <i>supE44</i> <i>thi-1</i> <i>recA1</i> <i>gyrA96</i> <i>relA1</i> <i>lac Hte</i> [F' <i>proAB</i> <i>lacIqZ</i> ΔM15 Tn10 (Tetr)]	Agilent Technologies®

Table 6 Primers used in Chapter 4

Mutated codons are shown in bold whereas mutated nucleotides are underlined. Restriction sites are represented in italics.

Plasmid	Sequence	Restriction Site
All pQE-30:: <i>pilA</i>	ACTTTCGGGCGGATAGGTTT	-
pQE-30:: <i>pilA</i>	TTCACCCTTATCGAGCTGCT	-
pQE-30:: <i>pilA</i> <sub>5</sub>	CTGCTGATCGTCGTTGCGAT	-
pQE-30:: <i>pilA</i> <sub>10</sub>	GCGATCATCGGTATTCTCGC	-
pQE-30:: <i>pilA</i> <sub>15</sub>	CTCGCTGCAATTGCGATTCC	-
pQE-30:: <i>pilA</i> <sub>20</sub>	ATTCCGCAGTTCTCGGCGTA	-
pMAL-c2x:: <i>pilA</i> /pMAL-p2x:: <i>pilA</i>	CCCGAAGCCGTTTTCACCCTTATCGAGCTGCT	XmnI
	CCCAAGCTTTTAACTTTTCGGGCGGATAGGT	HindIII
pMAL-c2x:: <i>pilA</i> <sub>20</sub> /pMAL-p2x:: <i>pilA</i> <sub>20</sub>	CCC GAAGCCGTTT ATTCCGCAGTTCTCGGCGTA	XmnI
	CCCAAGCTTTTAACTTTTCGGGCGGATAGGT	HindIII
pTYB11:: <i>pilA</i>	GGTGGTTGCTCTTCCAACCTTACCCTTATCGAGCTGCT	SapI
	GGTGGTCTGCAGTCATTAACCTTTTCGGGCGGATAGGT	PstI
pTYB11:: <i>pilA</i> <sub>10</sub>	GGTGGTCTGCAGTCATTAACCTTTTCGGGCGGATAGGT	PstI
	GGTGGTTGCTCTTCCAACGCGATCATCGGTATTCTCGC	SapI
pTYB11:: <i>pilA</i> <sub>19</sub>	GGTGGTTGCTCTTCCAACGCGATTCCGCAGTTCTCGGC	SapI
	GGTGGTCTGCAGTCATTAACCTTTTCGGGCGGATAGGT	PstI
pTYB11:: <i>pilA</i> <sub>22</sub>	GGTGGTTGCTCTTCCAACAGTTCTCGGCGTATCGTGT	SapI
	GGTGGTCTGCAGTCATTAACCTTTTCGGGCGGATAGGT	PstI
pTYB11:: <i>pilA</i> <sub>19</sub> Y27A	TCCGCAGTTCTCGGCG <u>GCT</u> CGTGTCAAGGCGTAC	-
	GTACGCCCTTGACACGAGCCGCCGAGAAGTGC	-
pTYB11:: <i>pilA</i> <sub>19</sub> Y32A	GTATCGTGTCAAGGCG <u>GCC</u> AACAGCGCGGCGTC	-
	GACGCCGCGCTGTTGGCCGCCTTGACACGATAC	-
pTYB11:: <i>pilA</i> <sub>19</sub> Y57A	CCGCATTTGCTGATGATCAAACC <u>GCT</u> CCGCCCGAAAGTTAA	-
	TTAACTTTTCGGGCGGAGCGGTTTGTATCATCAGCAAATGCGG	-
pTYB11:: <i>pilA</i> <sub>19</sub> R28A	CCGCAGTTCTCG <u>GCG</u> TATGCTGTCAAGGCG	-
	CGCCTTGACAGCATACGCCGAGAAGTGC	-
pTYB11:: <i>pilA</i> <sub>19</sub> D53,54A	GAGTCCGCATTTGCT <u>GCTGCT</u> CAAACCTATCCGCC	-
	GGGCGGATAGGTTTGTGACAGCAGCAAATGCGGACTC	-

Table 6 (cont'd)

<b>pTYB11::pilA<sub>19</sub>A20C</b>	GGTTGTTGTACAG <u>AACT</u> GCATTCCGCAGTTCTCGG	-
	CCGAGAACTGCGGAATGCAGTTCTGTACAACAACC	-

---

Table 7 Plasmids used in Chapter 4

Amino acid position based on the mature *pilA* gene sequence (i.e., after processing of its leader peptide).

Plasmid	Genotype	Reference
<b>pQE-30 UA</b>	P <sub>T5</sub> His <sub>6</sub> -tag Amp <sup>r</sup>	Qiagen®
<b>pQE-30::pilA</b>	pQE-30 plus <i>pilA</i> Amp <sup>r</sup>	This study
<b>pQE-30::pilA<sub>5</sub></b>	pQE-30 plus $\Delta 1-5'$ <i>pilA</i> Amp <sup>r</sup>	This study
<b>pQE-30::pilA<sub>10</sub></b>	pQE-30 plus $\Delta 1-10'$ <i>pilA</i> Amp <sup>r</sup>	This study
<b>pQE-30::pilA<sub>15</sub></b>	pQE-30 plus $\Delta 1-15'$ <i>pilA</i> Amp <sup>r</sup>	This study
<b>pQE-30::pilA<sub>20</sub></b>	pQE-30 plus $\Delta 1-20'$ <i>pilA</i> Amp <sup>r</sup>	This study
<b>pMAL-c2x</b>	P <sub>tac</sub> MBD-tag <i>malE</i> signal sequence Amp <sup>r</sup>	New England Biolabs Inc.®
<b>pMAL-p2x</b>	P <sub>tac</sub> MBD-tag Amp <sup>r</sup>	New England Biolabs Inc.®
<b>pMAL-c2x::pilA<sub>20</sub></b>	pMAL-c2x plus $\Delta 1-20'$ <i>pilA</i> inserted into XmnI-HindIII Amp <sup>r</sup>	This study
<b>pMAL-p2x::pilA<sub>20</sub></b>	pMAL-p2x plus $\Delta 1-20'$ <i>pilA</i> inserted into XmnI-HindIII Amp <sup>r</sup>	This study
<b>pTYB11</b>	P <sub>T7</sub> Sce VMA intein CBD-tag Amp <sup>r</sup>	New England Biolabs Inc.®
<b>pTYB11::pilA</b>	pTYB11 plus <i>pilA</i> inserted into NdeI-SapI Amp <sup>r</sup>	This study
<b>pTYB11::pilA<sub>10</sub></b>	pTYB11 plus $\Delta 1-10'$ <i>pilA</i> inserted into NdeI-SapI Amp <sup>r</sup>	This study
<b>pTYB11::pilA<sub>19</sub></b>	pTYB11 plus $\Delta 1-19'$ <i>pilA</i> inserted into NdeI-SapI Amp <sup>r</sup>	This study
<b>pTYB11::pilA<sub>20</sub></b>	pTYB11 plus $\Delta 1-20'$ <i>pilA</i> inserted into NdeI-SapI Amp <sup>r</sup>	This study
<b>pTYB11::pilA<sub>21</sub></b>	pTYB11 plus $\Delta 1-22'$ <i>pilA</i> inserted into NdeI-SapI Amp <sup>r</sup>	This study
<b>pTYB11::pilA<sub>19</sub>A20C</b>	pTYB11::pilA <sub>19</sub> <i>pilA</i> <sub>A20A</sub> <sup>a</sup> Amp <sup>r</sup>	This study
<b>pTYB11::pilA<sub>19</sub>A20CY27A</b>	pTYB11::pilA <sub>19</sub> <i>pilA</i> <sub>A20CY27A</sub> <sup>a</sup> Amp <sup>r</sup>	This study
<b>pTYB11::pilA<sub>19</sub>A20CY32A</b>	pTYB11::pilA <sub>19</sub> <i>pilA</i> <sub>A20CY32A</sub> <sup>a</sup> Amp <sup>r</sup>	This study
<b>pTYB11::pilA<sub>19</sub>A20CY57A</b>	pTYB11::pilA <sub>19</sub> <i>pilA</i> <sub>A20CY57A</sub> <sup>a</sup> Amp <sup>r</sup>	This study
<b>pTYB11::pilA<sub>19</sub>A20CY27,32,57A</b>	pTYB11::pilA <sub>19</sub> <i>pilA</i> <sub>A20CY27,32,57A</sub> <sup>a</sup> Amp <sup>r</sup>	This study
<b>pTYB11::pilA<sub>19</sub>A20CR28A</b>	pTYB11::pilA <sub>19</sub> <i>pilA</i> <sub>A20CR28A</sub> <sup>a</sup> Amp <sup>r</sup>	This study
<b>pTYB11::pilA<sub>19</sub>A20CD5354A</b>	pTYB11::pilA <sub>19</sub> <i>pilA</i> <sub>A20CD53,54A</sub> <sup>a</sup> Amp <sup>r</sup>	This study

Table 8 Buffers used to purify recombinant pilins as fusion proteins with a Chitin-binding Domain (CBD) using the IMPACT™ system using a chitin resin column

<b>Buffer</b>	<b>Composition</b>
Column Buffer	20 mM Tris-HCl pH 7.4, 100 mM NaCl, 1 mM EDTA
Lysis Buffer	20 mM Tris-HCl pH 7.4, 100 mM NaCl, 1 mM EDTA, 2% CHAPS
Wash Buffer 1	20 mM Tris-HCl pH 7.4, 600 mM 1 M NaCl, 1 mM EDTA
Wash Buffer 2	20 mM Tris-HCl pH 7.4, 1 M NaCl, 1 mM EDTA
Cleavage Buffer	20 mM Tris-HCl pH 9.0, 100 mM NaCl 50 mM DTT
Elution Buffer	20 mM Tris-HCl pH 9.0, 100 mM NaCl

***APPENDIX C***

FIGURES

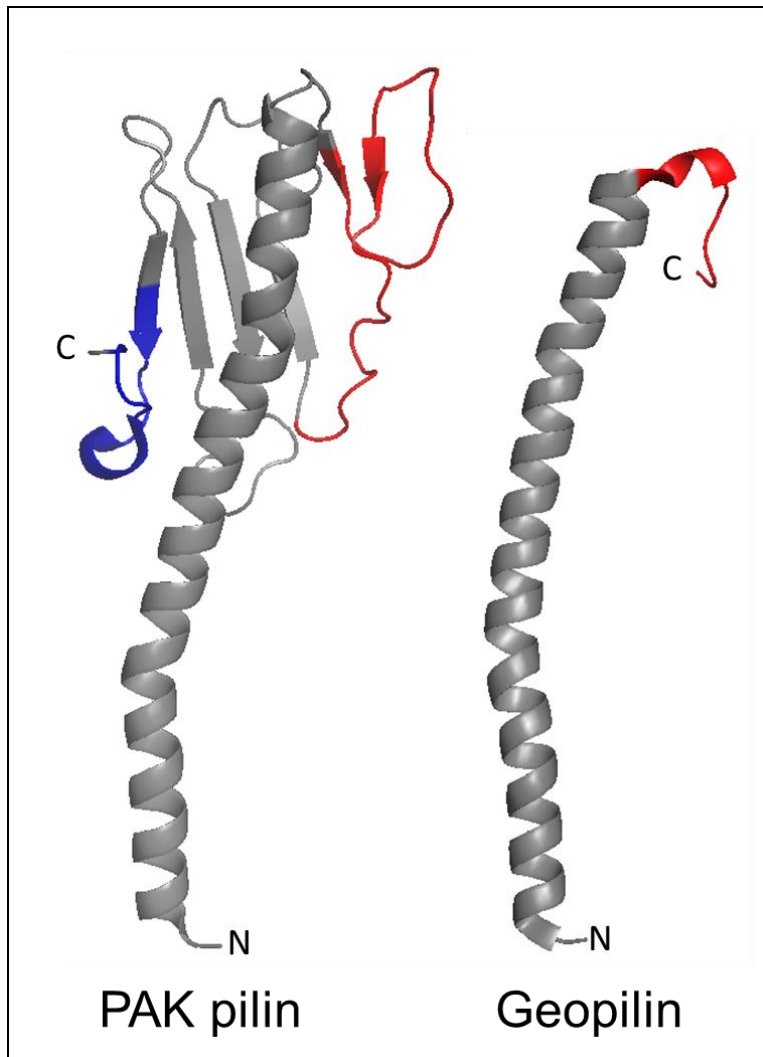


Figure 1 Structure of the PAK pilin and geopilin

Crystal structure of the *P. aeruginosa* strain K pilin<sup>49</sup> with the  $\alpha\beta$ -loop shown in red and the D region shown in blue. Representative NMR structure of the *G. sulfurreducens* pilin<sup>58</sup> with the random coil region shown in red

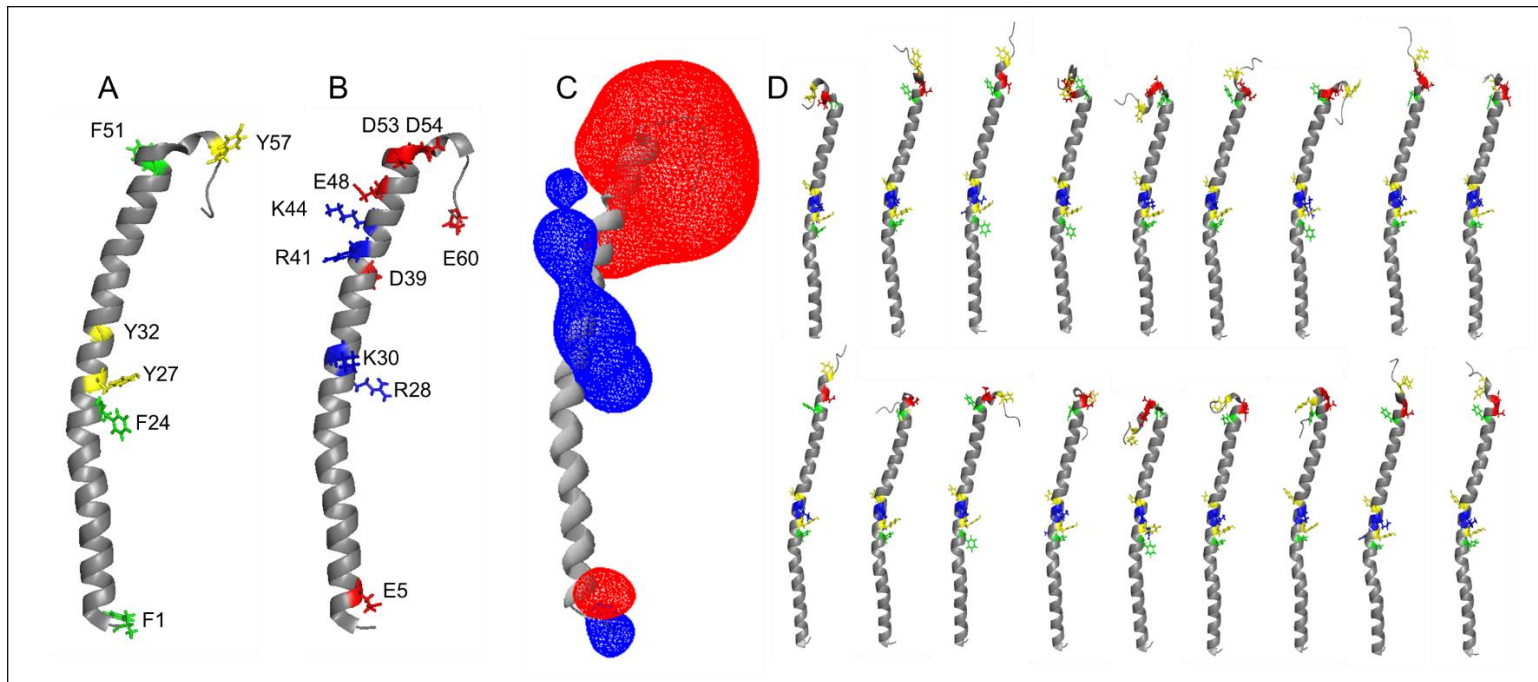


Figure 2 Properties of the *G. sulfurreducens* pilin

Representative NMR structure of the *G. sulfurreducens* pilin<sup>58</sup> showing: A) aromatic residues (phenylalanine in green and tyrosine in yellow) B) charged residues (negative residues in red and positive residues in blue) C) electrostatic potential calculated<sup>185</sup> for the pilin (positive potential in blue and negative potential in red). D) All NMR structures collected of the *G. sulfurreducens* pilin<sup>58</sup> showing the flexibility of the C-t random coil. Electrostatic potentials were computed for the *Geobacter sulfurreducens* NMR atomic structure<sup>58</sup> using Swiss-Pdb Viewer<sup>185</sup>.

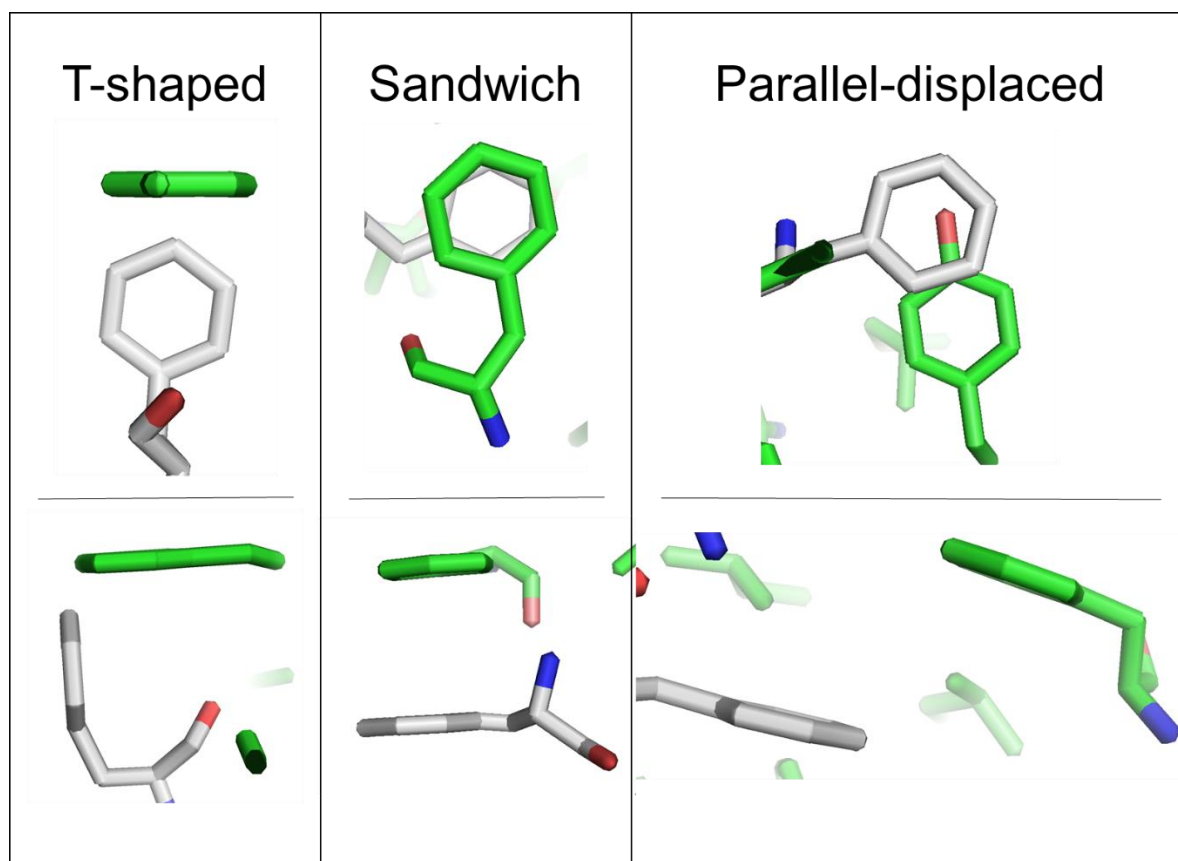


Figure 3  $\pi$ -stacking configurations

Images representing the three  $\pi$ -stacking configurations.

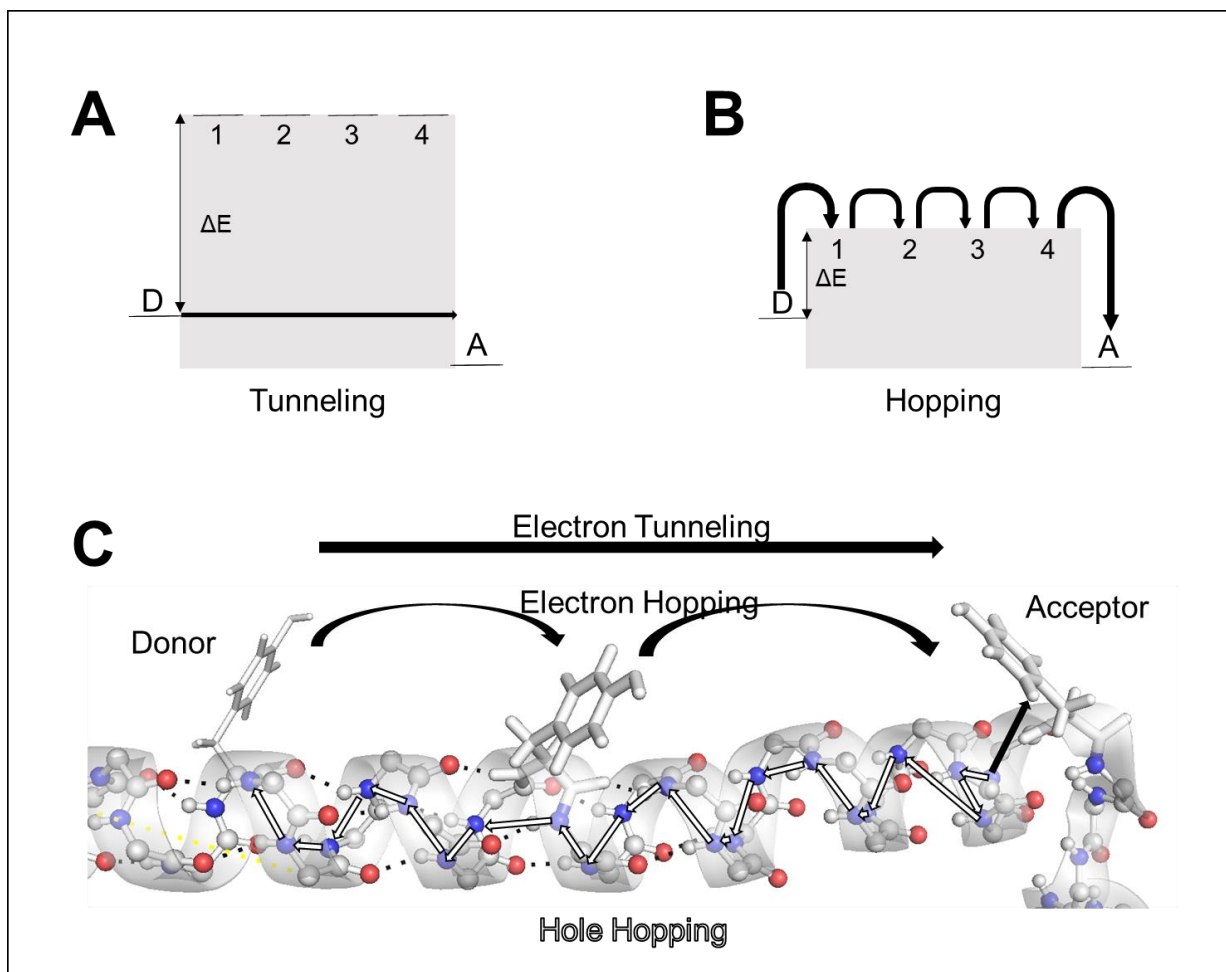


Figure 4 Charge transfer mechanisms

Depiction of tunneling (A) and hopping (B). Relay states are represented by 1, 2, 3, and 4.  $\Delta E$  is the barrier for movement into the relay state. (C) Representation of the possible mechanisms for charge transfer in an  $\alpha$ -helix (electron tunneling, electron hopping, and electron hole hopping through the amide groups of the peptide backbone). All black single headed arrows represent the movement of electrons. White single headed arrows represent the movement of electron holes.

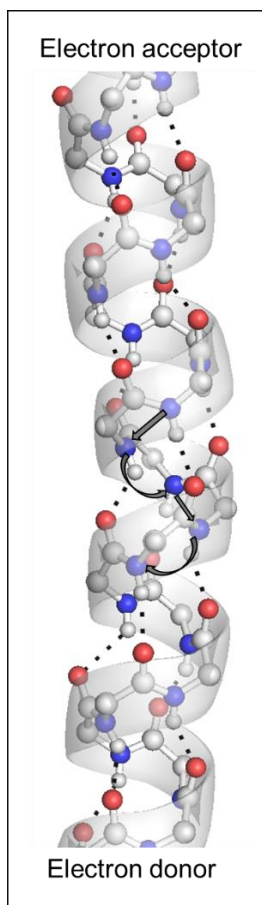


Figure 5 Amide backbone charge hopping

An image of the pilin  $\alpha$ -helical backbone (carbon and hydrogen in gray, oxygen in red, and nitrogen in blue). Hydrogen bonds are shown as dashed lines and the amide electron hole hopping pathway designated with arrows.

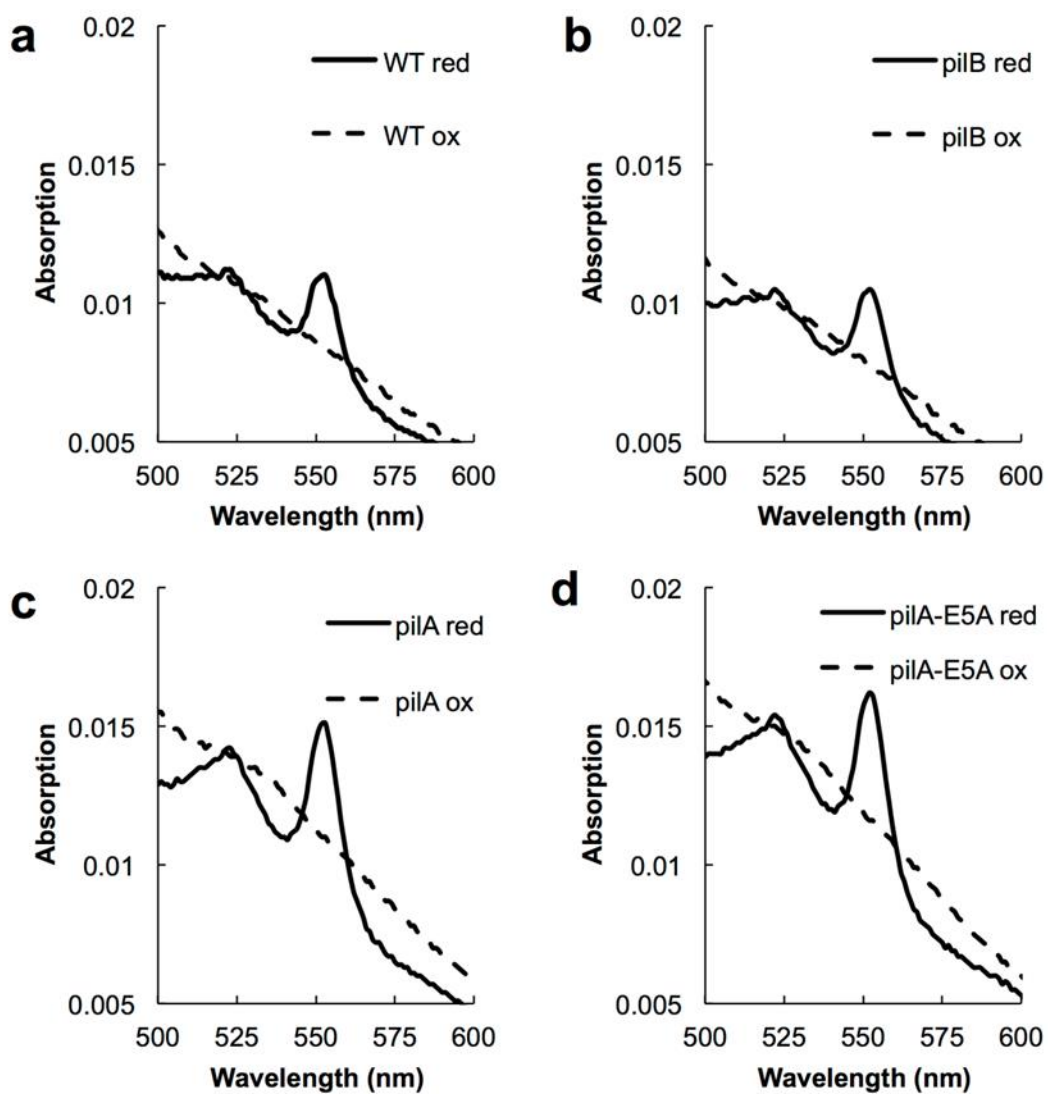


Figure 6 Absorption spectra of oxidize and reduced cell extracts

Absorption spectra of WT (a), pilB (b), pilA (c), and pilA-E5A (d) dithionite-reduced (solid) and then ferricyanide oxidized (dashed) and biofilm cell extracts, which were used to estimate the overall biofilm cytochrome contents.

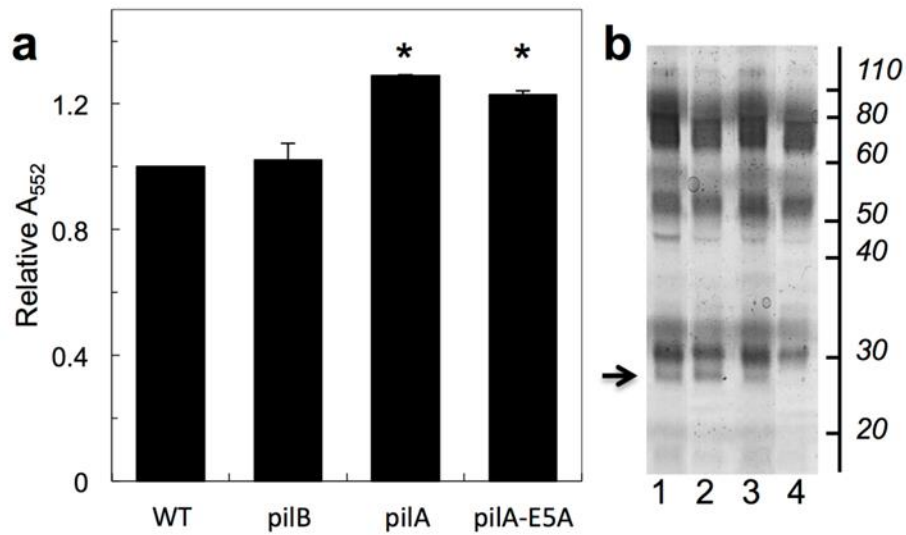


Figure 7 Characterization of cytochrome content in pili-deficient mutant cultures

(a) Cytochrome content (total cellular heme, measured with the pyridine hemochrome method) of planktonic cells of the pili-deficient strains *pilB*, *pilA*, and *pilA-E5A* relative to the WT. Significant changes relative to the WT values are indicated with stars (\*  $p < 0.05$ ) (b) Heme-stained proteins in whole-cell extracts of planktonic cells of WT (lane 1), *pilB* (lane 2), *pilA*, (lane 3), and *omcZ* (lane 4), which was used as negative control lane for the ~30-kDa *OmcZ<sub>S</sub>* band (arrow).

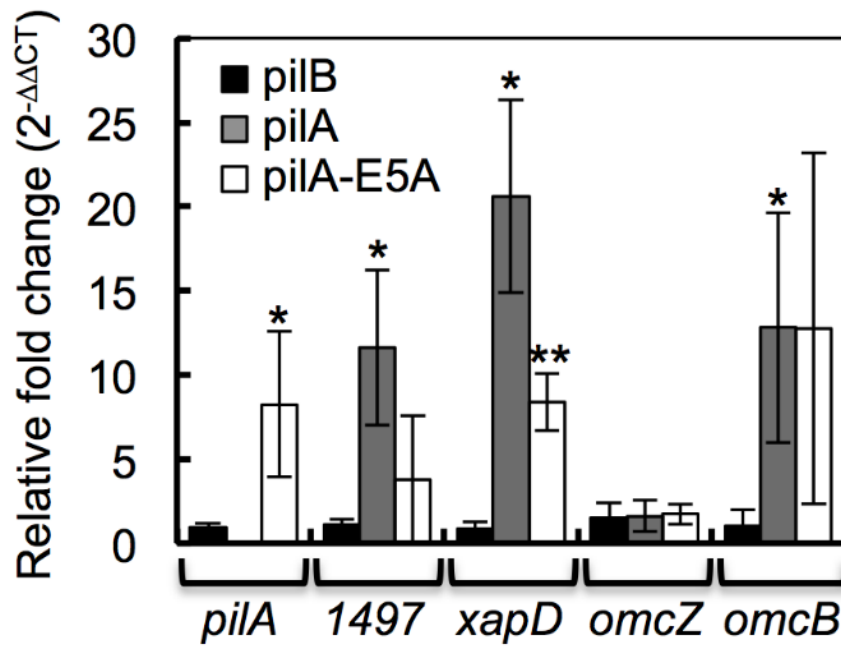


Figure 8 Expression of biofilm related genes in pilus deficient mutants

Expression of genes in the pilin operon (*pilA* and GSU1497), EPS synthesis (*xapD*), and outer membrane c-type cytochromes (*omcZ* and *omcB*) in 48-h old biofilms formed by the pili-deficient strains pilB (black), pilA (gray) and pilA-E5A (white) compared to WT. The constitutive gene *rpoD* was used as internal control. Significant changes relative to the pilB values are indicated (\* p <0.05; \*\* p <0.005).

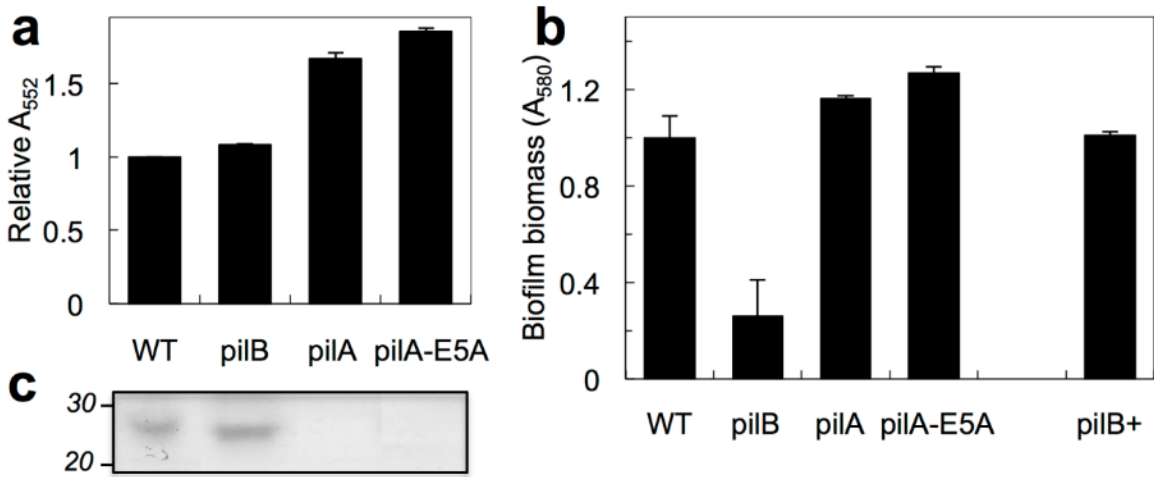


Figure 9 Phenotypic characterization of pili-deficient mutant (*pilB*, *pilA*, and *pilA-E5A*) biofilms (a) Relative *c*-type cytochromes content of the pili-deficient mutant strains in reference to WT cells (average and standard error of two biological replicates for each). (b) Biofilm biomass on plastic surfaces estimated from the  $OD_{580}$  of the biofilm-associated crystal violet solubilized with acetic acid (shown are averages and standard deviation of 8 biofilm replicates of the WT, pili-deficient mutants, and the genetic complemented *pilB+* strain). (c) Heme-containing protein bands isolated from the biofilm matrix of the WT and pili-deficient strains. Lanes were loaded with 20  $\mu$ g of protein. Numbers at left are relative molecular masses of protein standards in kDa.

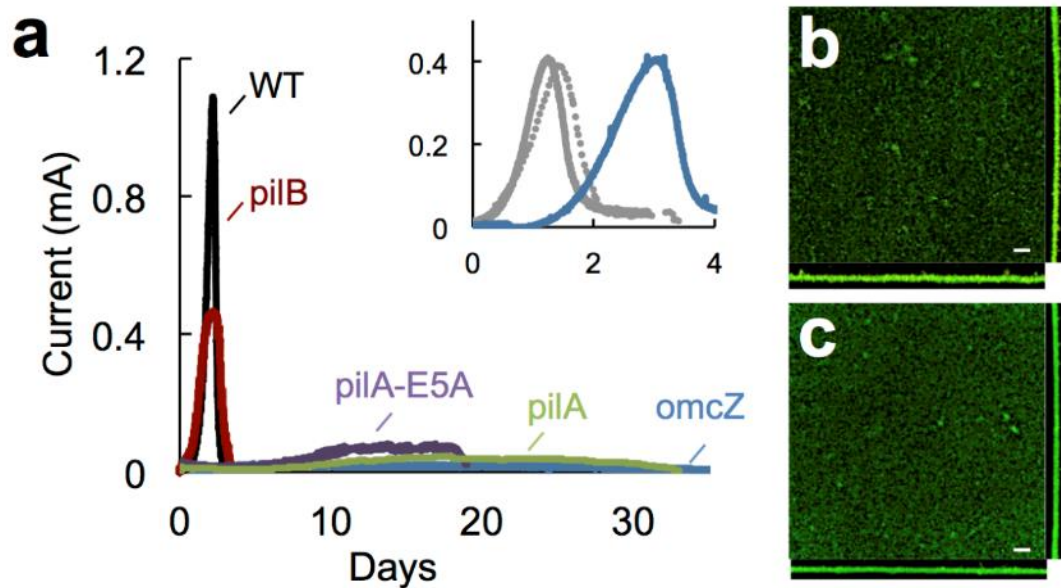


Figure 10 Biofilm electroactivity of selected mutants in MECs fed with 1 mM acetate

(a) Current generation by WT, pili-deficient strains (*pilB*, *pilA*, and *pilA-E5A*), and *omcZ* mutant in MECs fed with 1 mM acetate. Inset shows current generation (Y axis, in mA) over time (X axis, in days) by double mutants *pilB mshE* (solid gray), *pilB gspE* (dashed gray), and an equal mixture of *pilB* and *omcZ* cells (blue). (b and c) Confocal micrographs showing top and side views of biofilms of the WT (b) and *pilB* (c) strains stained with the BacLight viability kit (green, live; red, dead). Scale bar, 20 μm.



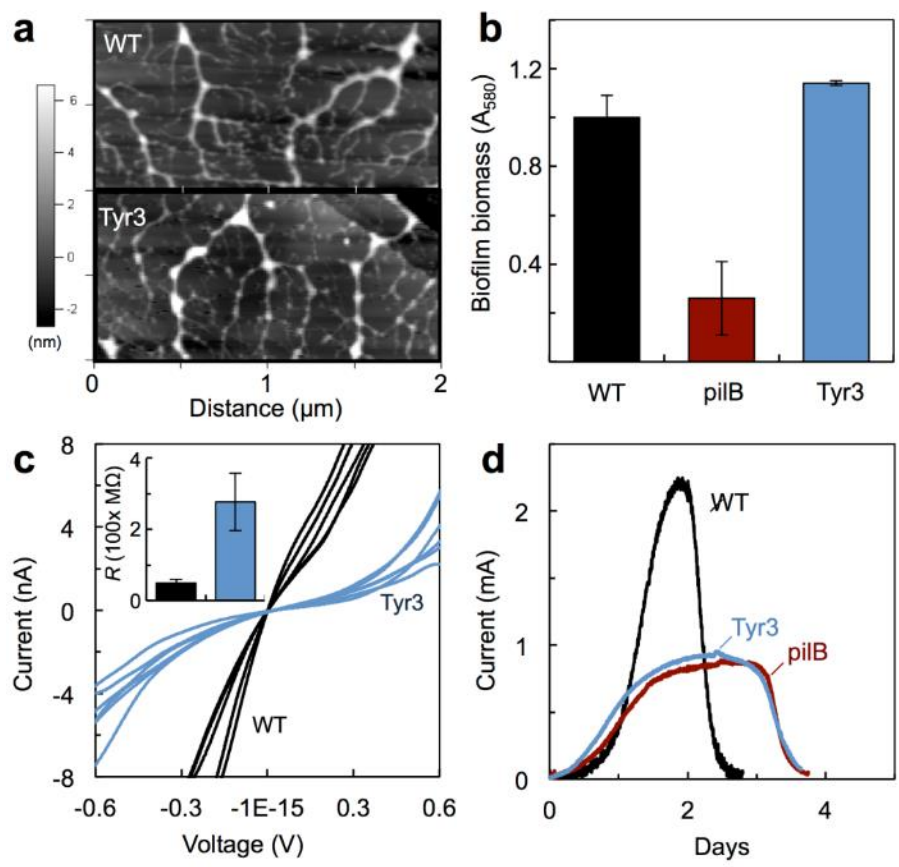


Figure 12 Role of pilus conductivity in the growth and electroactivity of anode biofilms

(a) AFM topographic images of pili purified from the WT and Tyr3 strains and deposited on a HOPG surface. (b) Biomass of 48-h old biofilms of the pilB and Tyr3 mutants relative to WT (shown are averages and standard deviation of 8 biofilm replicates for each strain). (c). Current-voltage ( $I-V$ ) plots obtained after probing the transversal conductivity of individual WT (black) and Tyr3 (blue) pili deposited on the HOPG surface as shown in (a). Inset shows the average resistance values obtained from the  $I-V$  plots and standard deviation. (d) Current production by WT, pilB, and Tyr3 biofilms grown in MECs fed with 3 mM acetate.

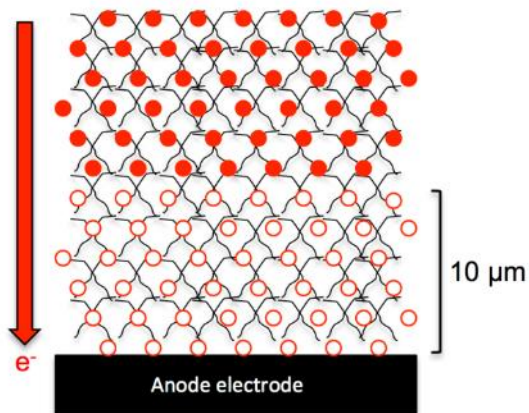


Figure 13 Model of mechanistic stratification of electroactive biofilms

Cytochromes (circles) and pili (crisscrossed lines) permeate the biofilm matrix and contribute to electron transfer in the layers of biofilm stratum proximal to the electrode. The efficiency of the cytochrome pathway is limited in the distal region of the biofilm (> 10 μm away from the electrode), resulting in the accumulation of reduced cytochromes (indicated by the solid circles) and leaving the pili network required as an electronic conduit.

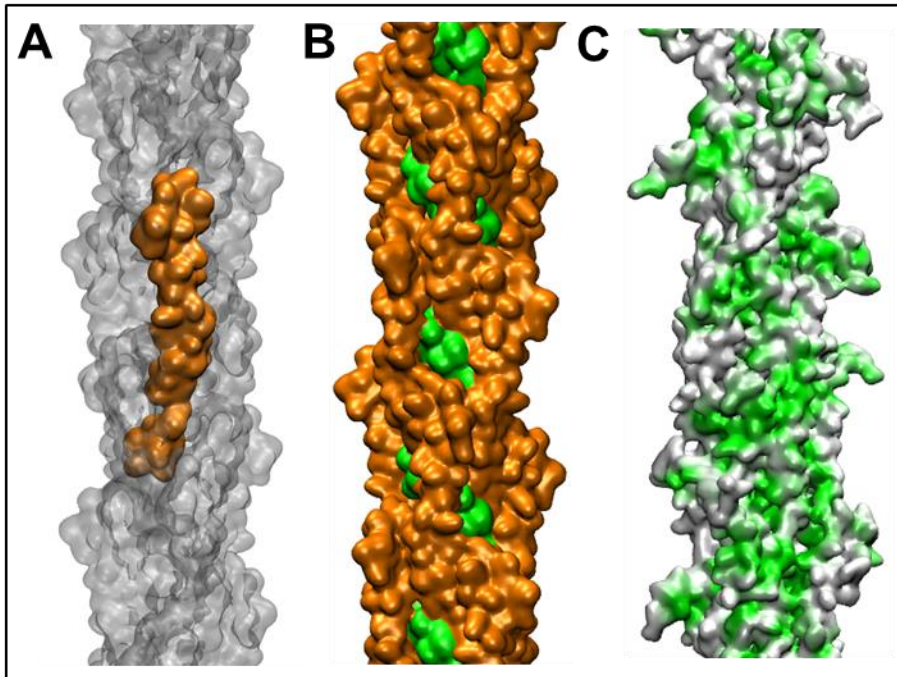


Figure 14 Surface maps of MS-optimized GS pilus

A) The position of one pilin in the optimized pilus structure, (orange), B) the exposed core amino acids (green), and C) the aromatic residue isodensity. Reprinted with permission<sup>137</sup>.

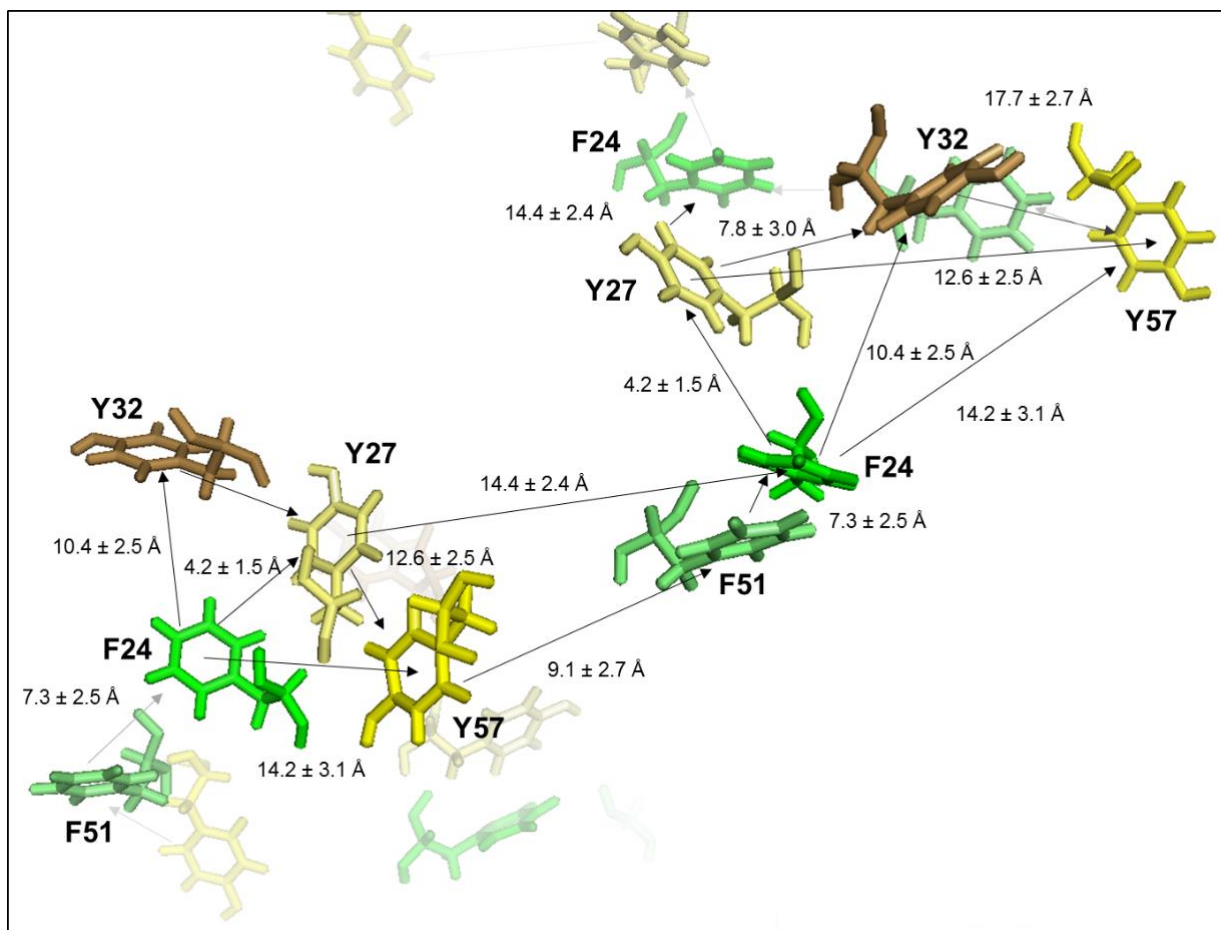


Figure 15 Potential charge transfer pathways identified in the MD model

Relationship of aromatic residues in the *G. sulfurreducens* MD pilus model. Average distances between the amino acids across the 19 subunit assembly are indicated (arrows).

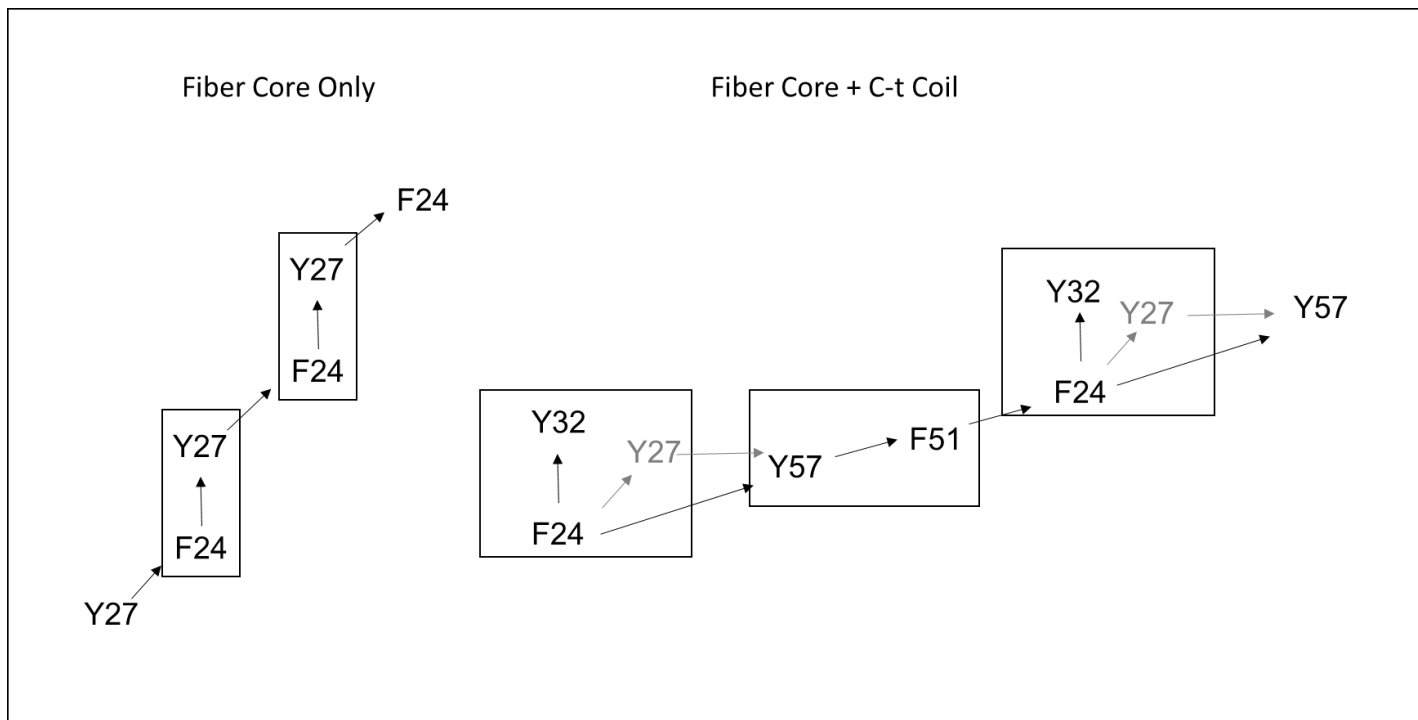


Figure 16 Electron transfer paths predicted in the *G. sulfurreducens* pilus from the MD-refined pilus model

The fiber core only path involves the electron hopping between two residues buried in the fiber core (F24 and Y27). The fiber core + C-t coil path involves both buried (F24 and Y27) and exposed aromatic residues (Y32 and F51) on fiber core as well as the C-t random coil (Y57). Y27 is in gray to indicate that it is an alternate path for ET. For each path, intramolecular transfers are enclosed in boxes.

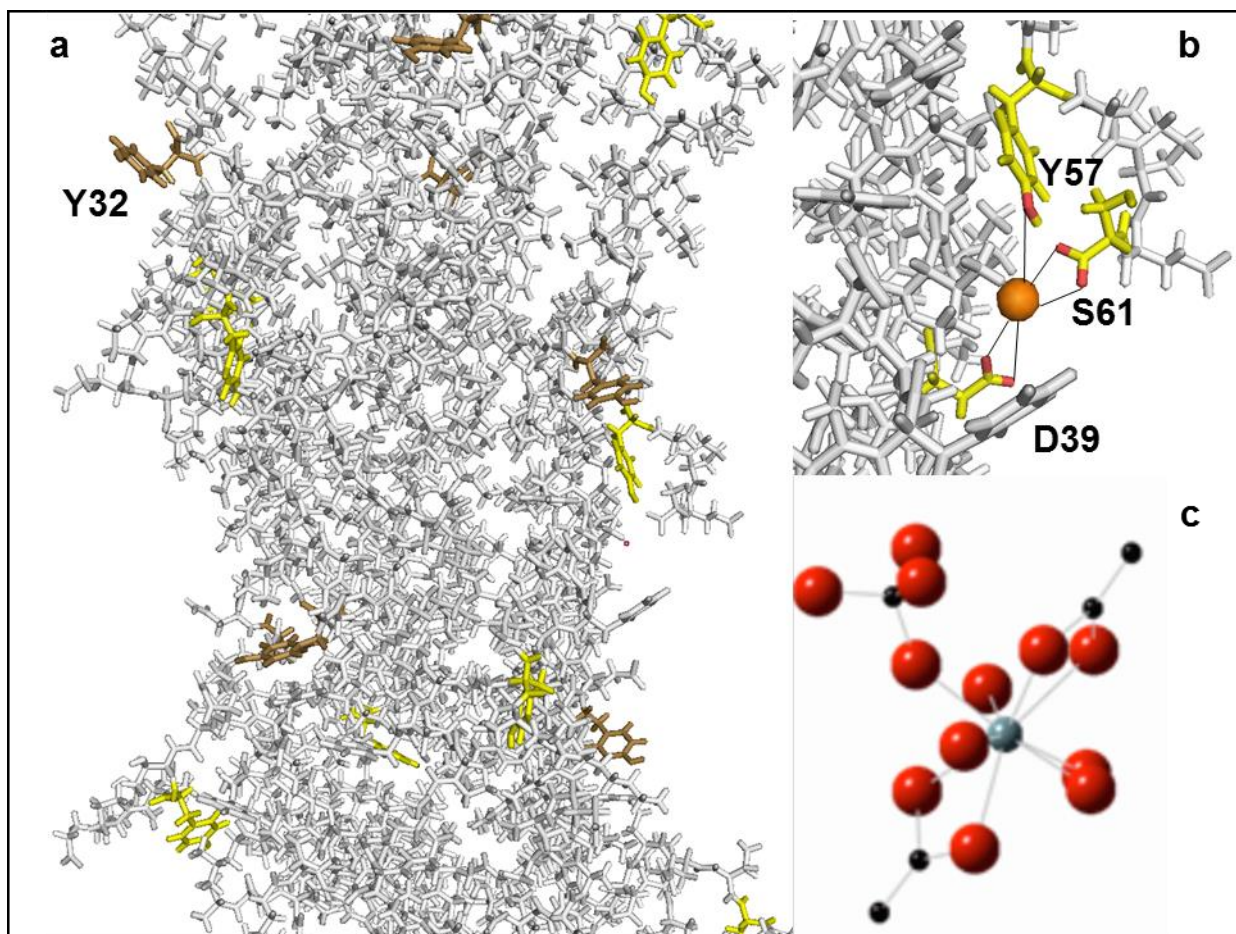


Figure 17 Surface exposure of Y32 and Y57

(a) MD-model of the *G. sulfurreducens* pilus fiber showing the surface exposure of tyrosine residues Y32 (bronze) and Y57 (yellow). (b) Close-up of Y57 interacting with an uranium atom (orange) through its hydroxyl group and coordinations by the carboxyl groups of D39 and the terminal S61 residues. (c) Atomic model showing the coordination of U(IV) with pili ligands (oxygen, red; U(IV), gray; carbon, black) showing two bidentate and one monodentate carboxyl linkages. Reproduced with permission from<sup>13</sup>.

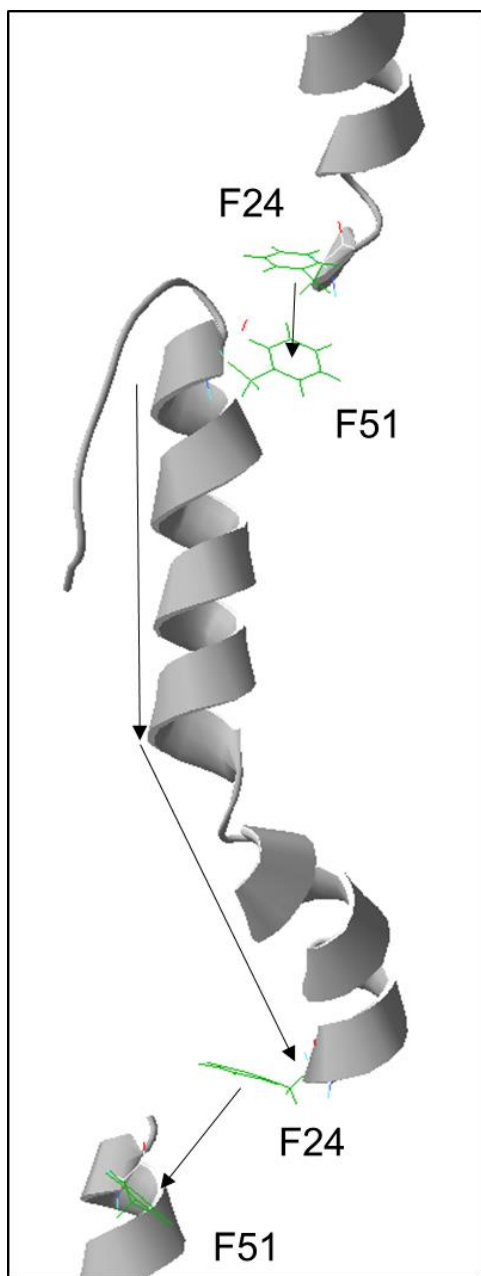


Figure 18 Amide electron hole hopping and phenylalanine dimer intermolecular transfer pathway

Direction of electron hole hopping indicated by arrows.

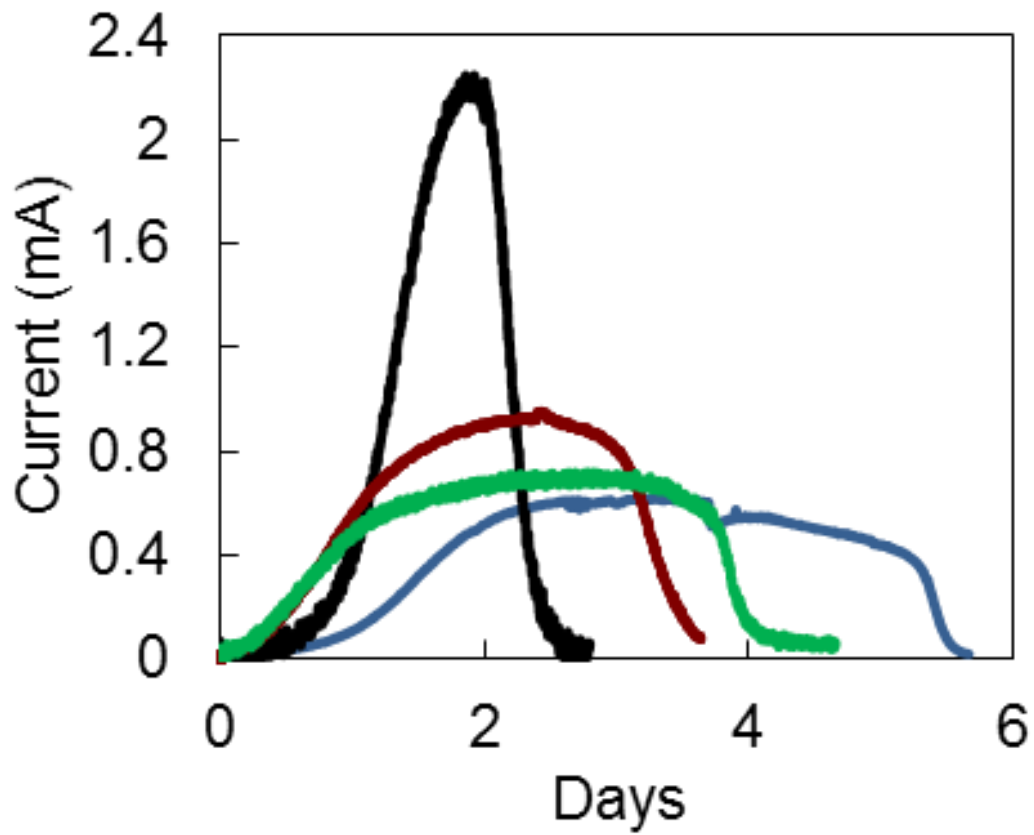


Figure 19 Biofilm electroactivity in MECs fed with 3 mM acetate for Y32 and Y57

Current generation by WT (black), Tyr3 (red), Y57A (green), and Y32A (blue) MECs fed with 3 mM acetate.

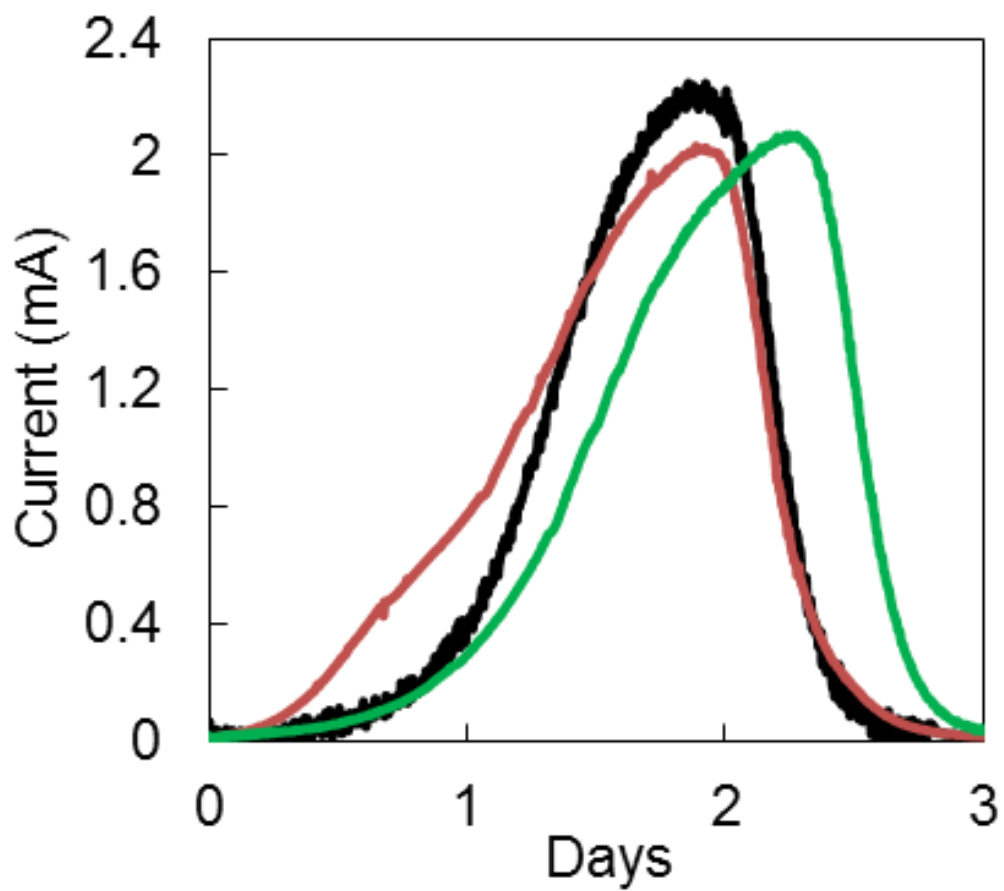


Figure 20 Biofilm electroactivity in MECs fed with 3 mM acetate for Y27 amino acid replacement mutants

Current generation by WT (black), Y27F (pink), and Y27A (green) in MECs fed with 3 mM acetate.

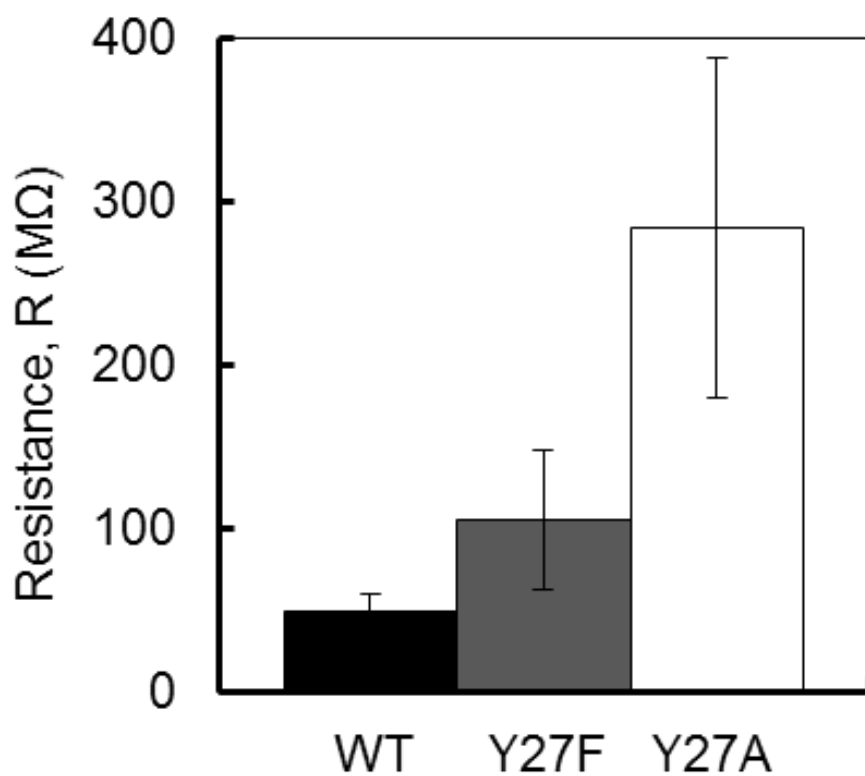


Figure 21 Transversal CP-AFM measurements of Y27 amino acid replacements

Average resistance values obtained from the *I-V* plots and standard deviation.

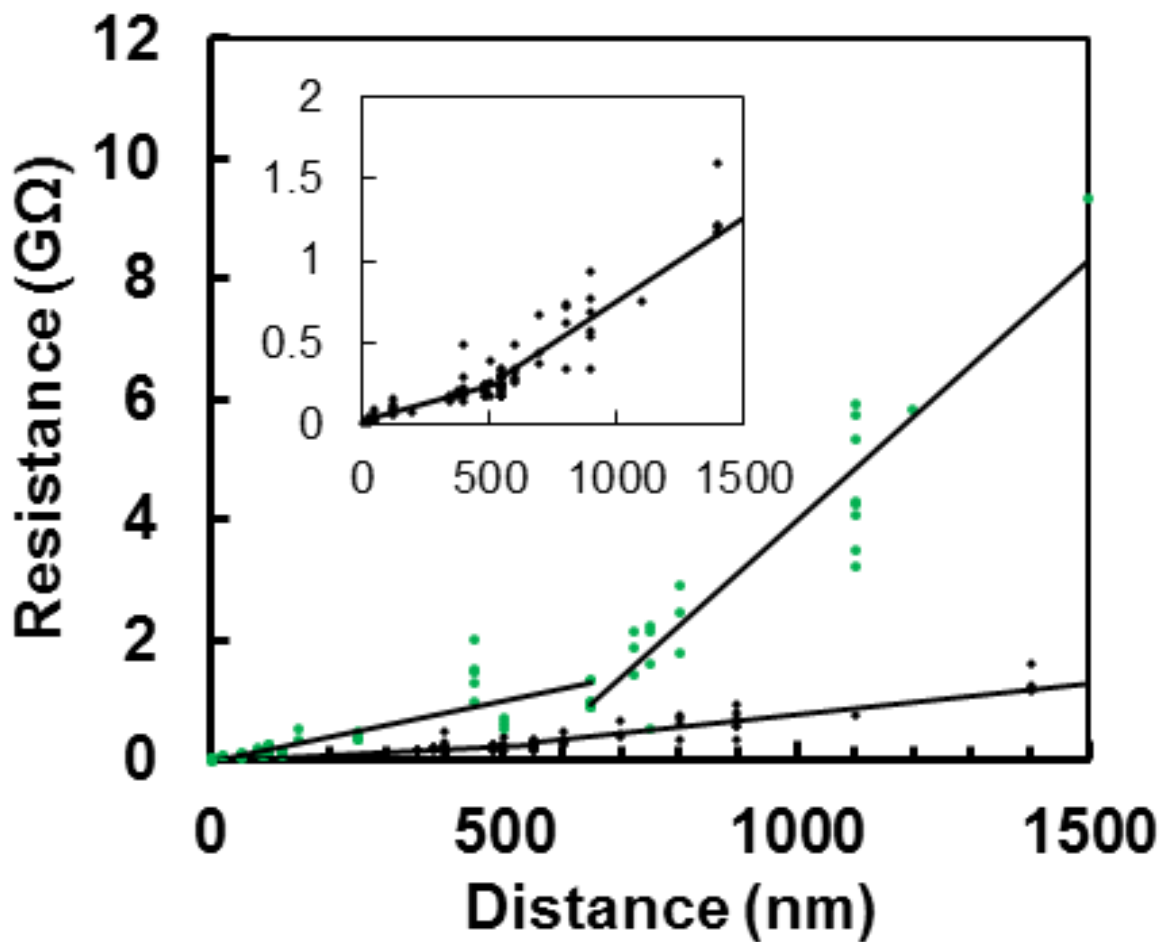


Figure 22 CP-AFM transport measurements along WT and Y27A pili

Correlations of resistance values and distance from the gold electrode were generated from measurements performed on WT (black) and Y27A mutant (green) pili, respectively. Expanded view of WT resistance values (inset).

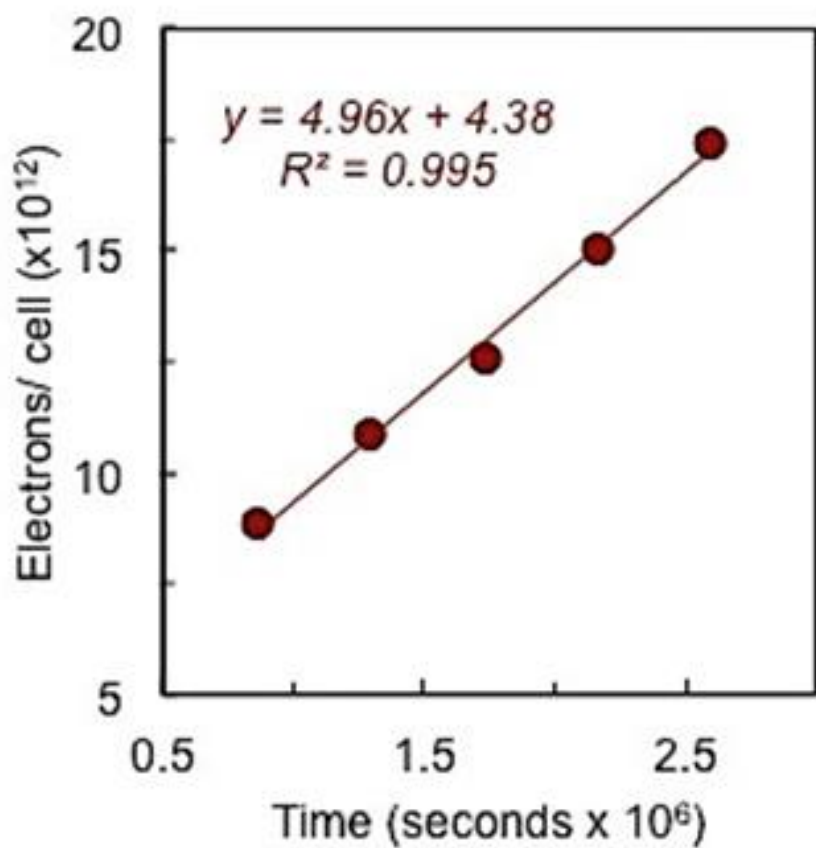


Figure 23 Electron transport rates per cell during growth of *G. sulfurreducens* with poorly crystalline Fe(III) oxides

Calculated from the rates of Fe(II) production and cell growth reported previously<sup>34</sup>.

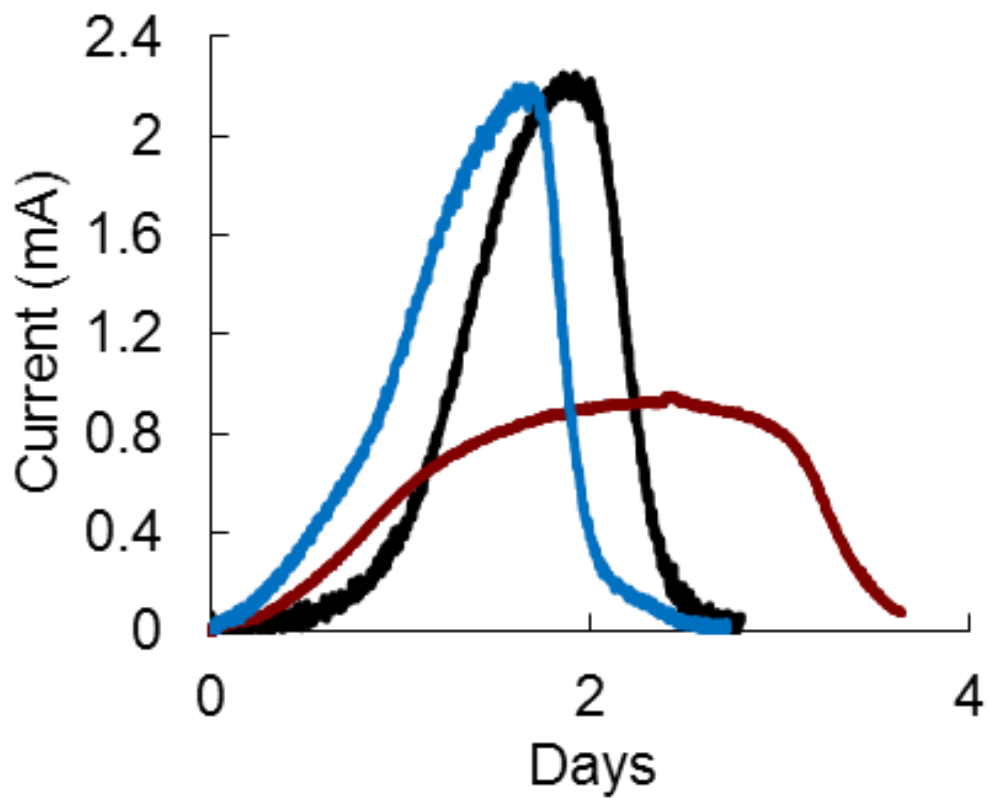


Figure 24 Biofilm electroactivity of phenylalanine vs. alanine replacement in MECs fed with 3 mM acetate

Current generation by WT (black), Tyr3-F (blue), and Tyr3 (red) in MECs fed with 3 mM acetate.

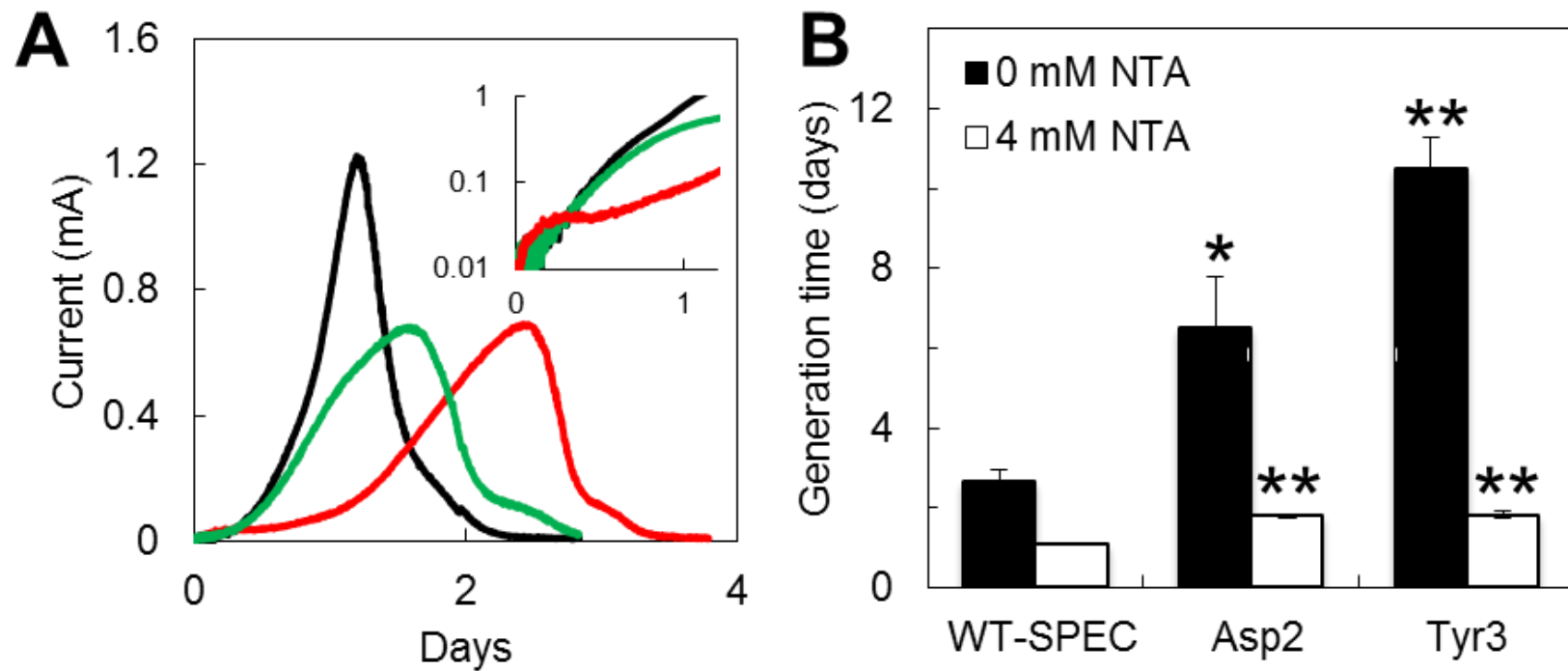


Figure 25 Comparison of the reduction of external electron acceptors by Asp2 and Tyr3

a) Current generation by WT (black), Asp2 (red), and Tyr3 (green) in MECs fed with 1 mM acetate. b) Fe(III) oxide reduction for WT-SPEC, Asp2, and Tyr3 with (white) and without (black) the addition of 4 mM NTA.

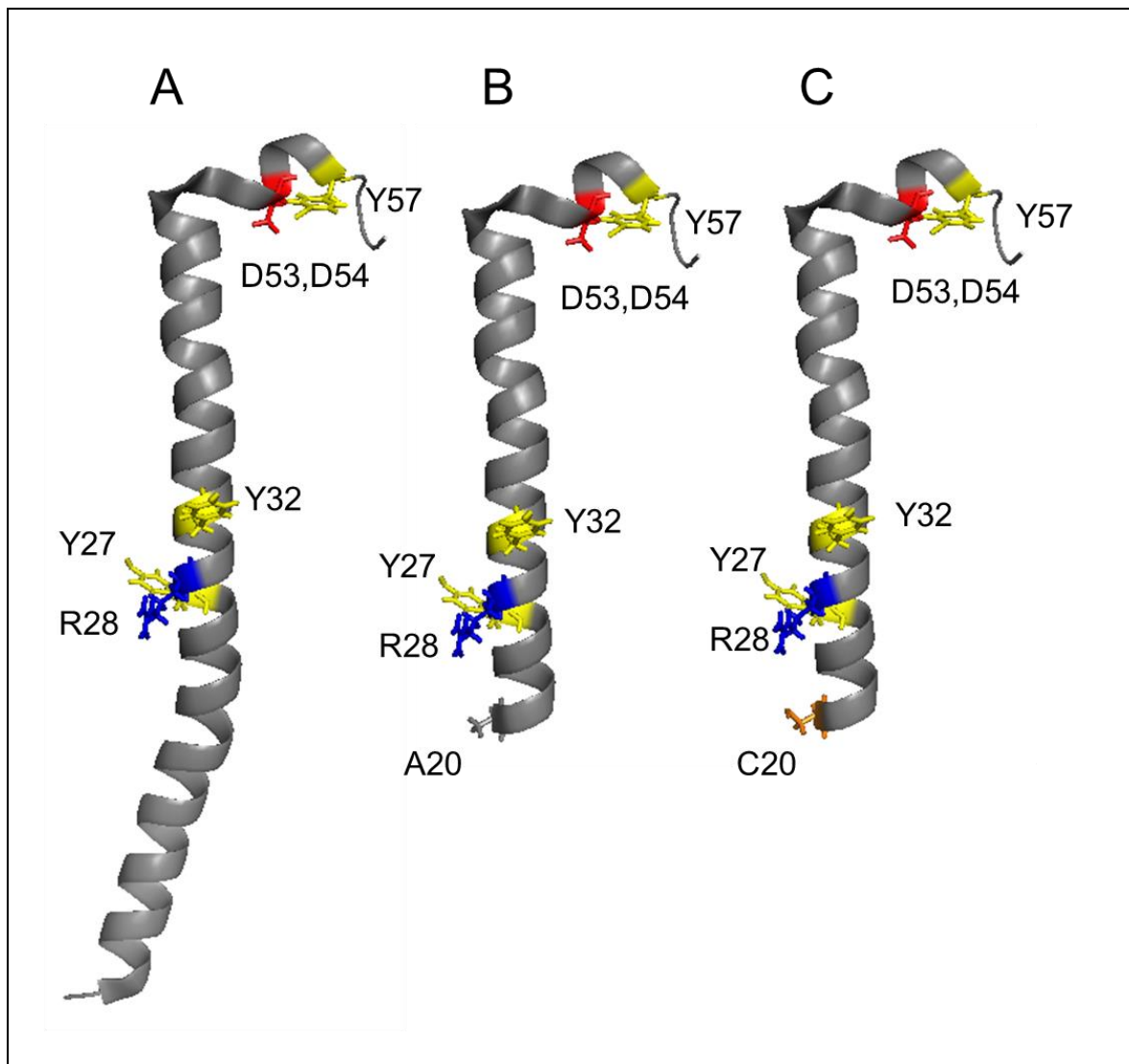


Figure 26 NMR-derived PiIa structural model of the *G. sulfurreducens* PiIa and predicted structure of recombinant PiIa<sub>19</sub> pilins

Structure of a) PiIa, b) PiIa<sub>19</sub> and c) PiIa<sub>19</sub>-A20C. All residues mutated for this study are labelled.

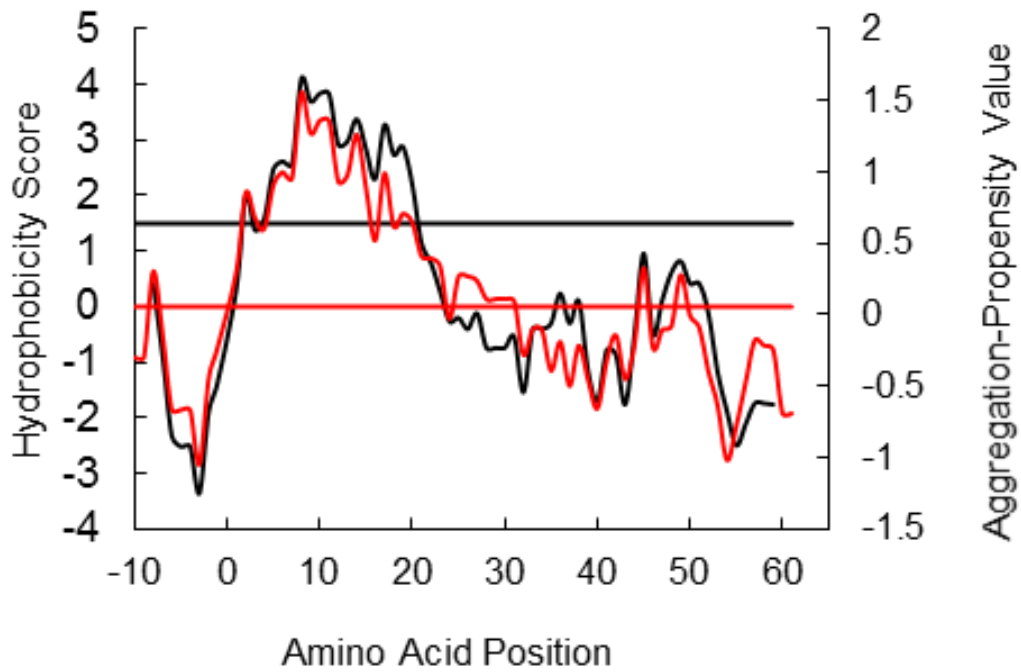


Figure 27 AGGRESCAN and Kyte-Doolittle analyses

The Kyte-Doolittle hydrophobicity plot (black) was determined using a 3 amino acid window for the the PilA pilin precursor, which contains a hydrophilic N-t leader peptide. The AGGRESCAN plot for the PilA precursor is also shown (red). The straight lines indicate the aggregation (red) and hydrophobicity (black) cut-offs (at 0 and 1.5, respectively) used for the analyses.

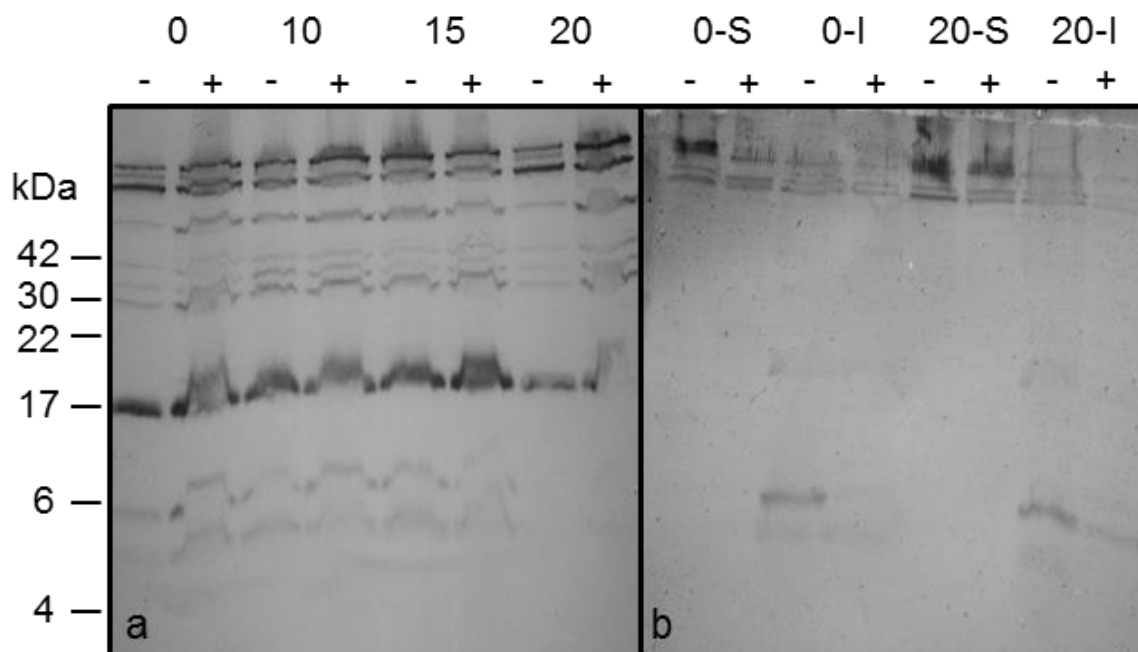


Figure 28 Expression and purification of recombinant pilins carrying a 6×His-tag

Western blot analysis using a) anti-PilA and b) anti-His antibodies. For gel A the soluble fraction of the untruncated PilA and the 10, 15, and 20 amino acid truncations were analyzed before (-) and after (+) induction. For gel B the soluble (S) and insoluble (I) fractions were analyzed before (-) and after (+) induction.

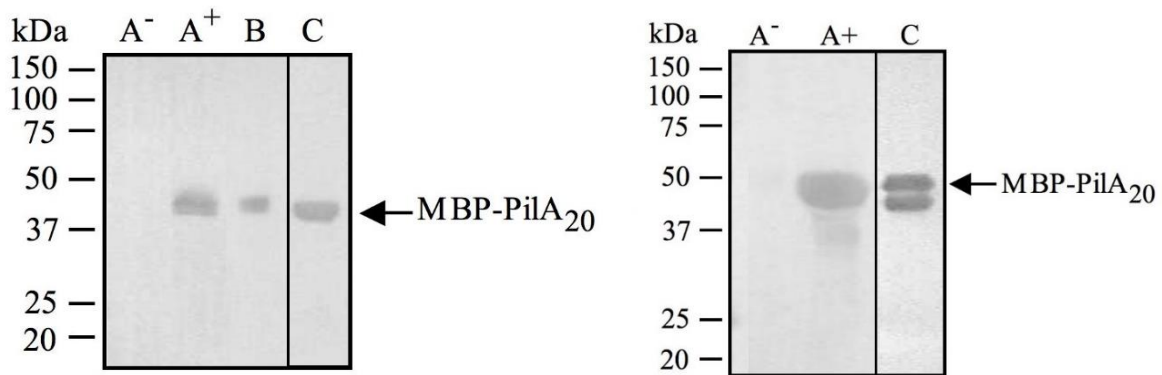


Figure 29 Western blot analysis of periplasmic (left) and cytoplasmic (right) proteins fractions during the expression and purification of MBP-PilA<sub>20</sub>

Proteins in crude extracts (A) before (-) and after (+) induction with IPTG, soluble protein fraction (B), and elution fraction from amylose column (C) were separated in a 12% glycine SDS-PAGE and blotted to a membrane for hybridization with anti-MBP antibodies. The migration of the periplasmic and cytoplasmic MBP-PilA<sub>20</sub> fusion protein is indicated with arrows.

Reproduced from <sup>166</sup> with permission from Dr. Angelines Castro-Forero.

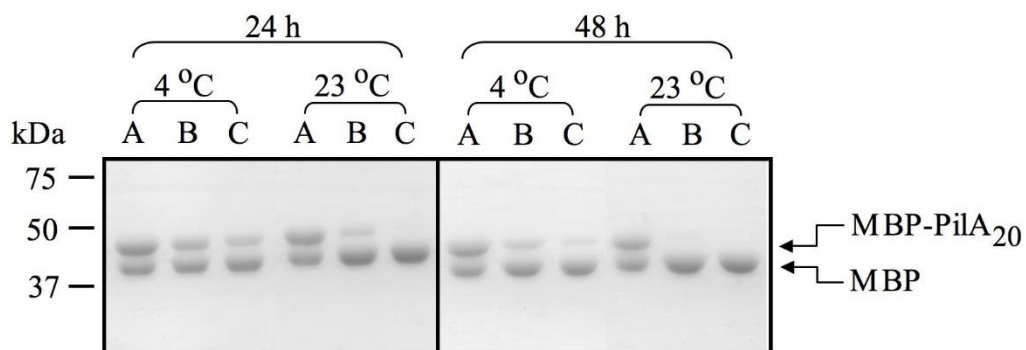


Figure 30 Cleavage efficiency of PilA<sub>20</sub> from its MBP tag by Factor Xa protease

Elution fractions from an amylose column were incubated with Factor Xa protease at 4°C and 23 °C for 24 h (left) and 48 h (right). Proteins in the samples were analyzed by 7.5% glycine SDS-PAGE. Shown are proteins in gels from controls incubated in buffer without protease (A), and samples incubated with 0.5 µg/mL (B) or 1.0 µg/mL (C) of protease. Reproduced from <sup>166</sup> with permission from Dr. Angelines Castro-Forero.

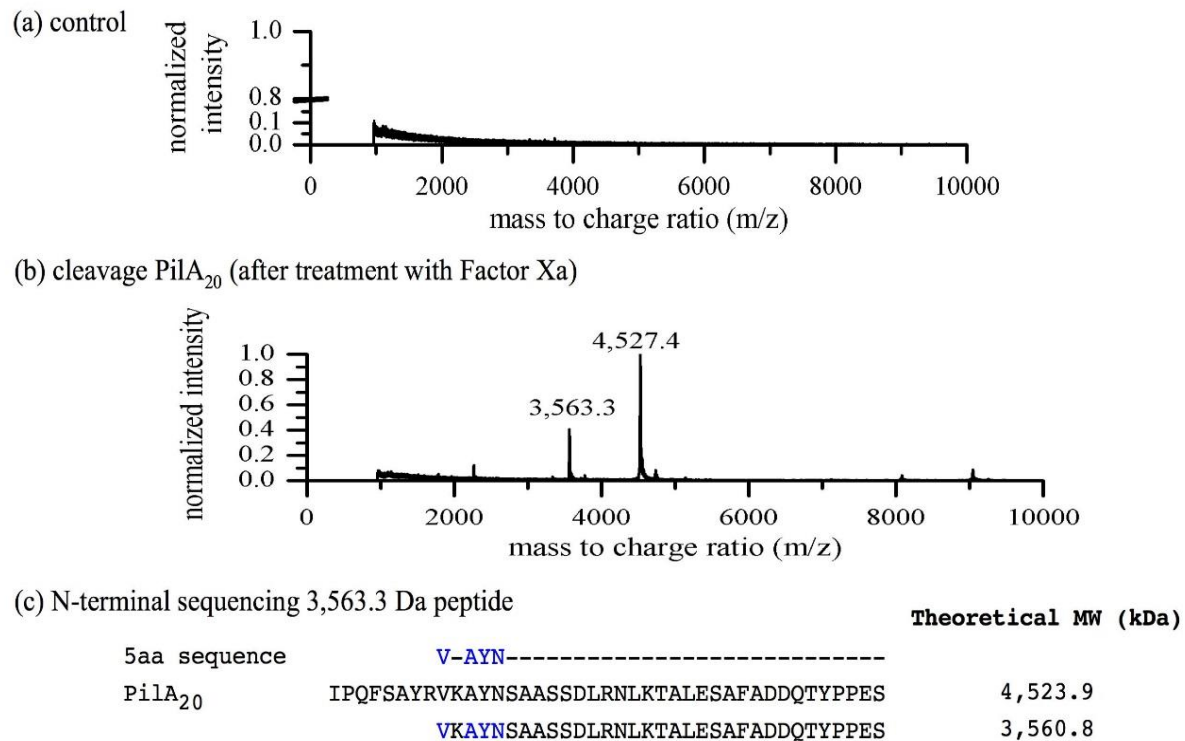


Figure 31 Production of PilA<sub>20</sub> subunits after treatment with Factor Xa protease

MALDI-TOF MS analysis of a) sample untreated with protease used as a control, and b) sample treated with protease. MS results indicate two peptides are produced during cleavage. The peptide with MW of 4,527.4 Da corresponds to the PilA<sub>20</sub> subunit. c) N-terminal sequencing of the peptide with MW of 3,563.3 Da. Sequencing indicated that non-specific cleavage of the pilin subunit occurred. Reproduced from <sup>166</sup> with permission from Dr. Angelines Castro-Forero.

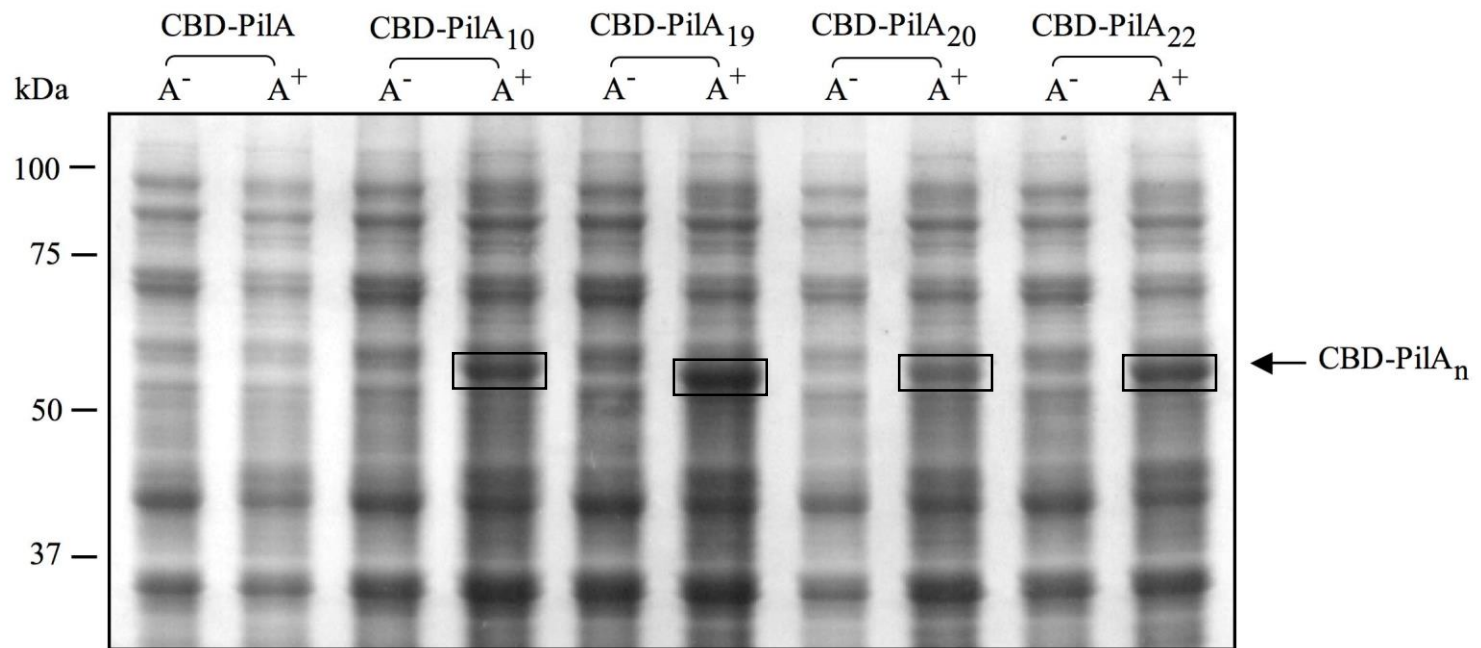


Figure 32 Expression of the full-length pilin (PilA) and various truncated pilins (PilA<sub>n</sub>), all in fusions with a CBD tag (CBD-PilA<sub>n</sub>)  
 Expression was determined by analyzing cell pellet samples before (A<sup>-</sup>) and after (A<sup>+</sup>) induction using a 12% glycine SDS-PAGE.

Modified from <sup>166</sup> with permission from Dr. Angelines Castro-Forero.

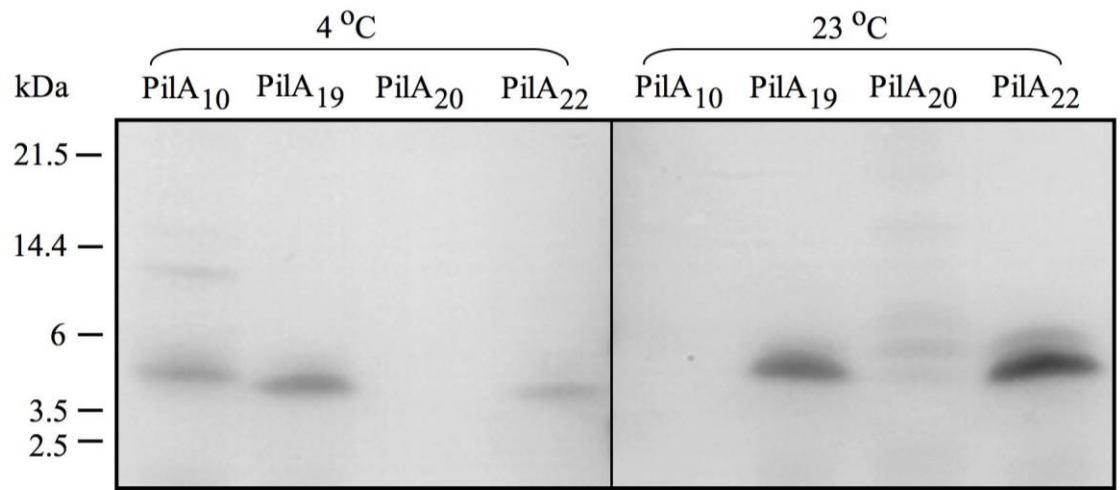


Figure 33 Presence of pilin monomers in elution from chitin column after cleavage from CBD tag determined by 16-20% Tricine SDS-PAGE

Reproduced from <sup>166</sup> with permission from Dr. Angelines Castro-Forero.

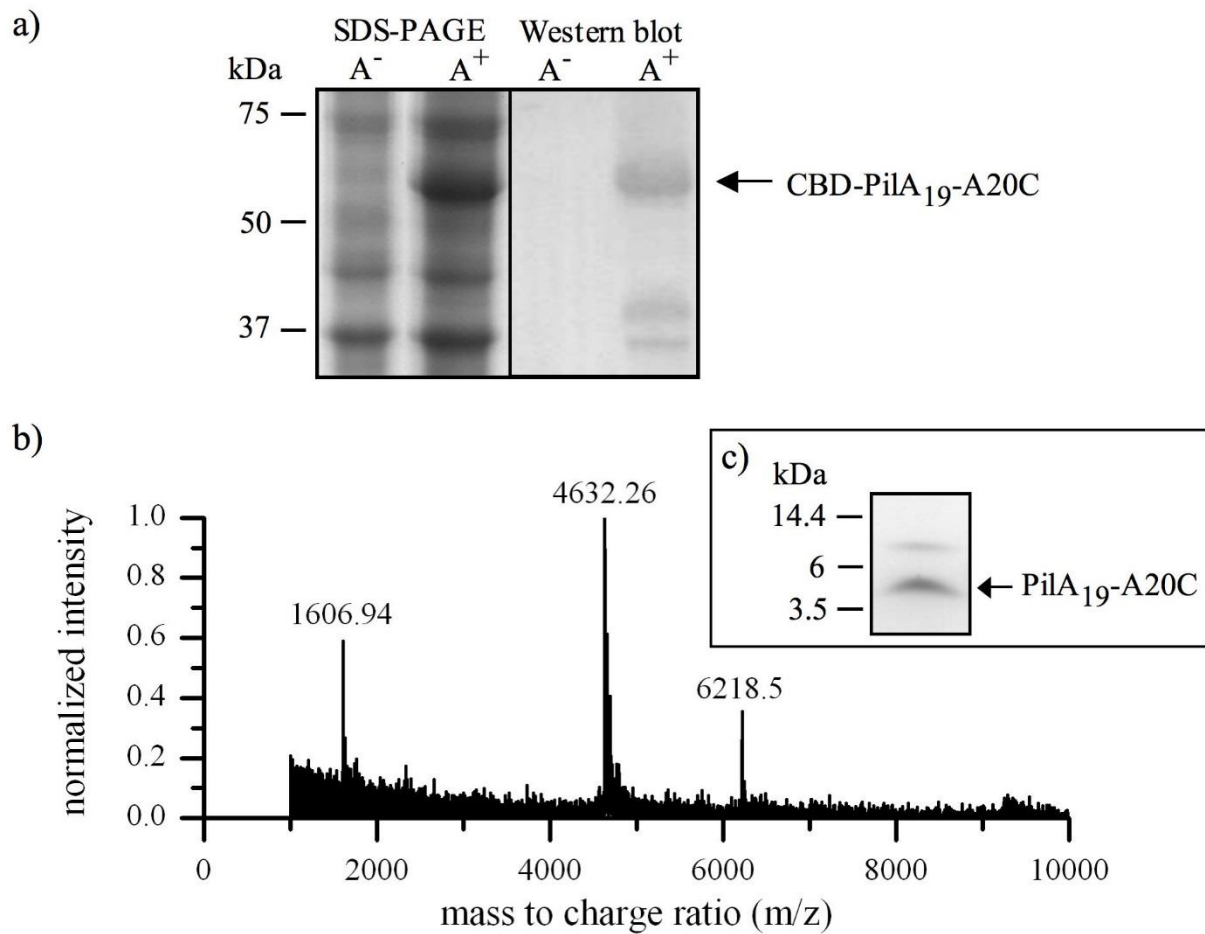


Figure 34 Expression and purification of recombinant PilA<sub>19</sub>-A20C subunits

a) 12% SDS-PAGE and Western blot analysis of cells before (A<sup>-</sup>) and after (A<sup>+</sup>) induction. Anti-chitin serum was used for the Western blot. b) MALDI-TOF mass spectrometry and c) 10-20% tricine gel of elution fraction after purification. Reproduced from <sup>166</sup> with permission from Dr. Angelines Castro-Forero.

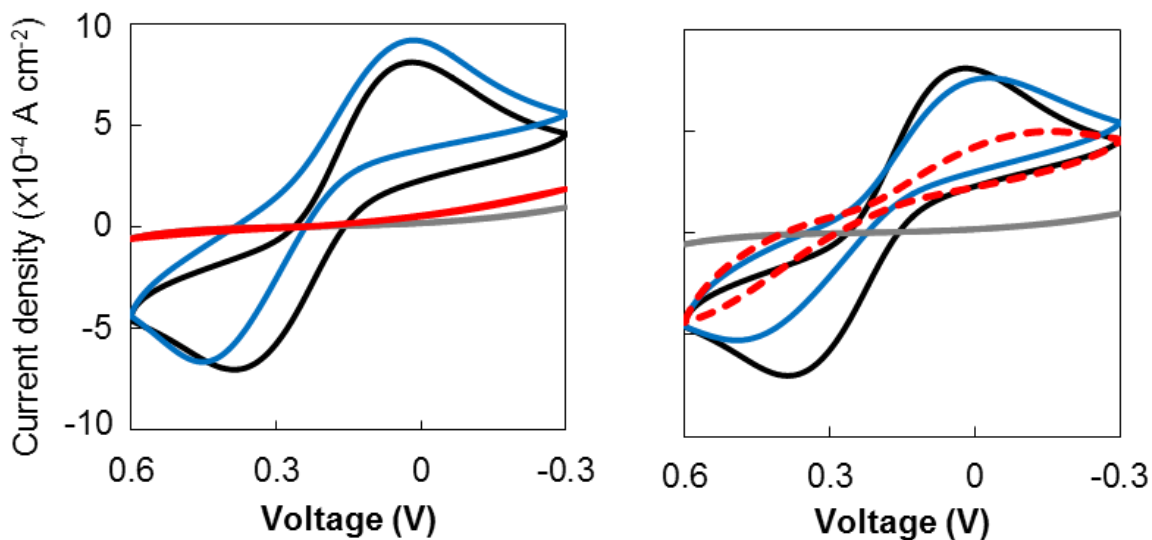


Figure 35 Effect of DTT on the electrochemical activity of PiA<sub>19</sub>-A20C pilins on a gold electrode. Shown in blue are cyclic voltammograms of gold electrodes incubated with PiA<sub>19</sub>-A20C to form a pilin monolayer in the presence (left) or absence (right) of DTT. Controls with pilin monolayers treated with 1-undecanethiol SAM (red), bare gold (black), and electrodes insulated with a 1-undecanethiol SAM (gray) are also shown. Data were recorded at room temperature in 100 mM sodium phosphate buffer at pH 7.0 containing 100 mM NaCl, and 5 mM K<sub>3</sub>[Fe(CN)<sub>6</sub>] at a potential scan rate of 100 mV s<sup>-1</sup>.

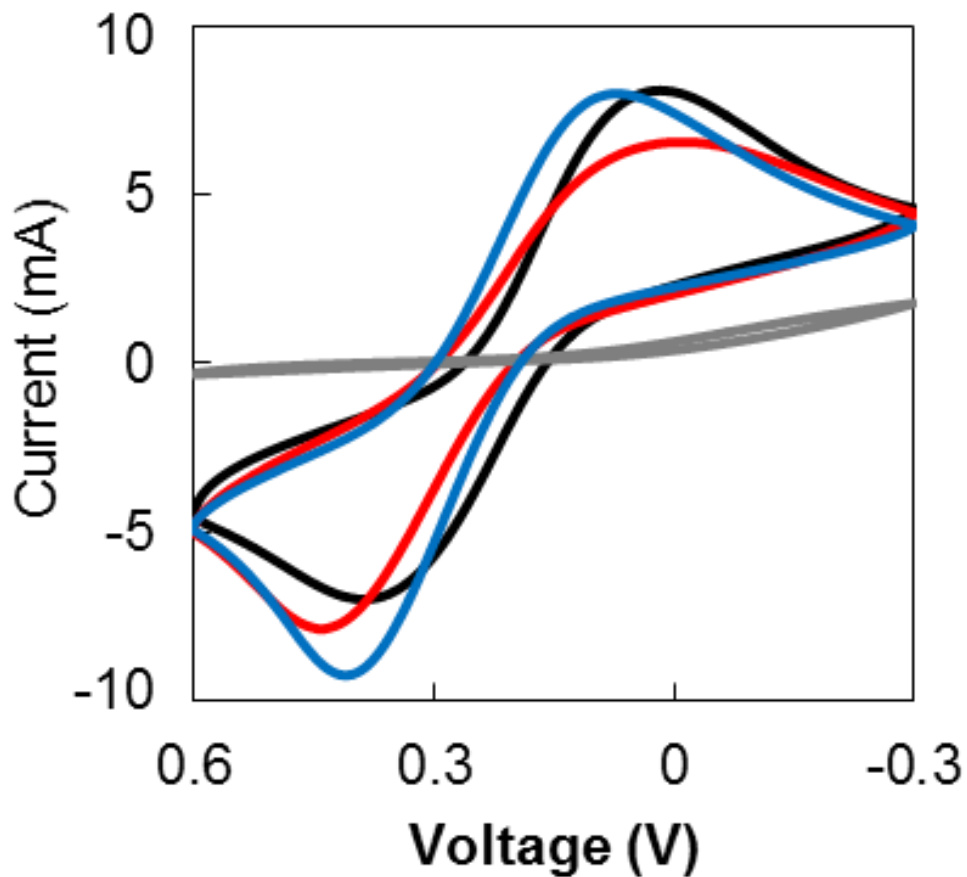


Figure 36 Effect of solvent (acetonitrile) in the deposition of  $\text{PiiA}_{19}\text{-A20C}$  on a gold electrode

Shown are cyclic voltammograms of gold electrodes incubated with either  $\text{PiiA}_{19}\text{-A20C}$  that has been buffer exchanged into acetonitrile (blue) or dialyzed into elution buffer (red) to form a pilin monolayer. Controls bare gold (black), and electrodes insulated with a 1-undecanethiol SAM (gray) are also shown. Data were recorded at room temperature in 100 mM sodium phosphate buffer at pH 7.0 containing 100 mM NaCl, and 5 mM  $\text{K}_3[\text{Fe}(\text{CN})_6]$  at a potential scan rate of 100  $\text{mV s}^{-1}$ .

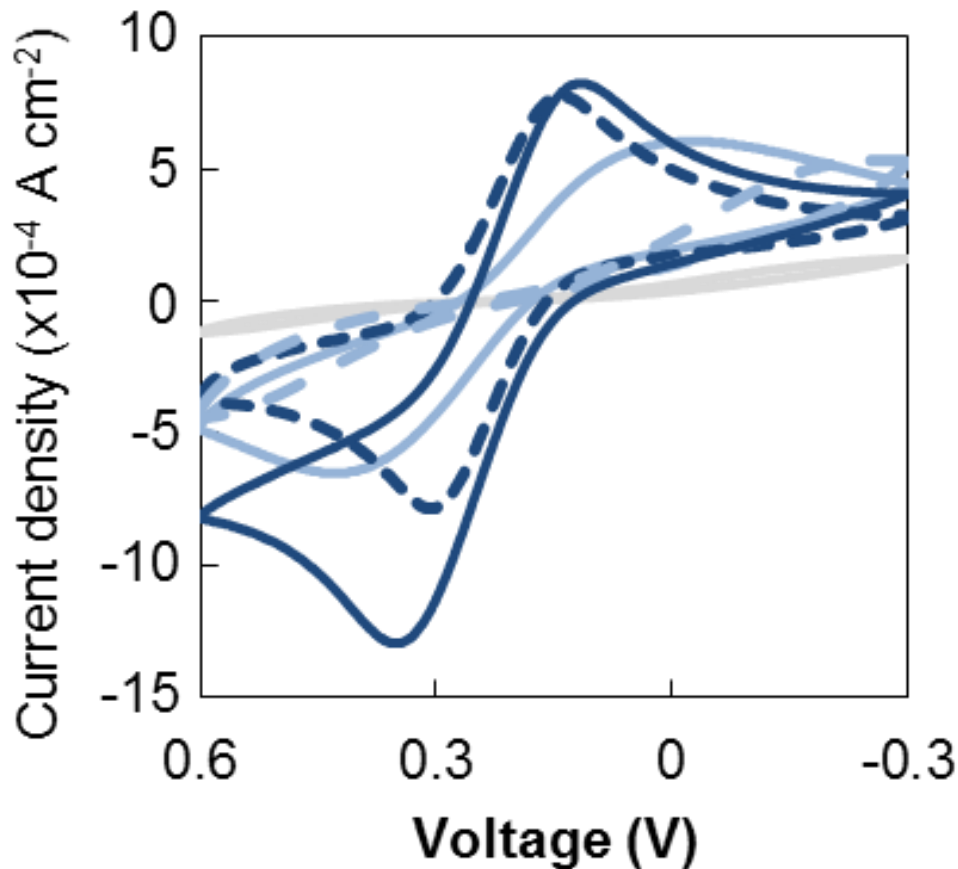


Figure 37 Effect of length of deposition time of PilA<sub>19</sub>-A20C in acetonitrile on a gold electrode

Recombinant pilins were incubated at room temperature in an anaerobic glove bag for differing times; 0 h (gray, solid), 12 h (light blue, dash), 24 h (light blue, solid), 48 h (dark blue, dashes), and 120 h (dark blue, solid). Electrodes were then washed with 100 % ethanol and incubated for 48 h with 1 mM 1-undecanethiol. Data were recorded at room temperature in 100 mM sodium phosphate buffer at pH 7.0 containing 100 mM NaCl, and 5 mM K<sub>3</sub>[Fe(CN)<sub>6</sub>] at a potential scan rate of 100 mV s<sup>-1</sup>.

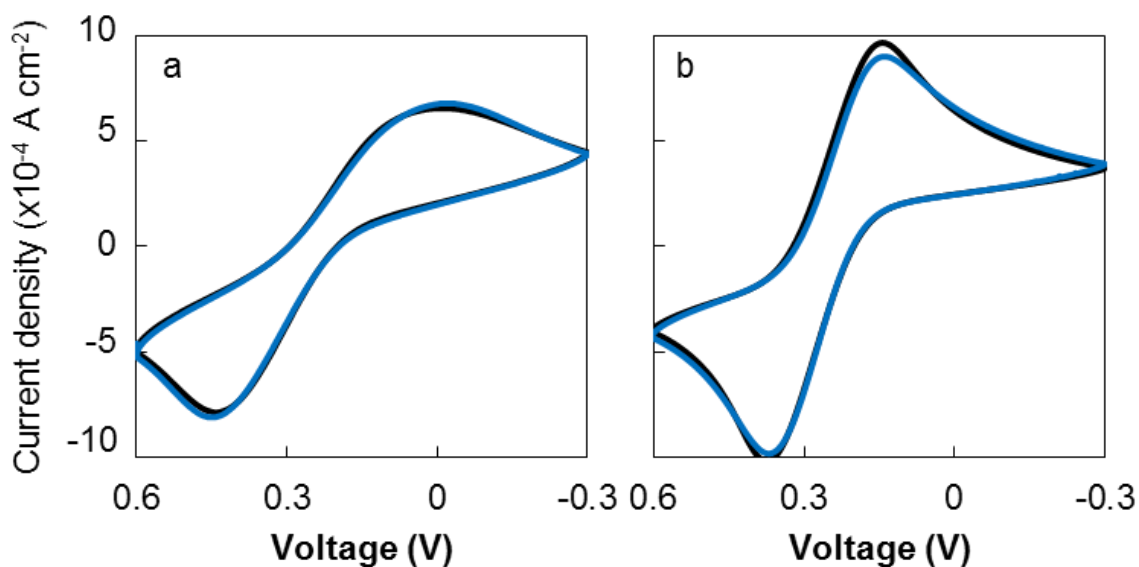


Figure 38 Effect of mixing and age of pilin sample on deposition of PilA<sub>19</sub>-A20C in acetonitrile

(a) Effect of mixing the PilA<sub>19</sub>-A20C solution: electrodes were rocked (blue) or stationary (black) and were deposited for 48 h. (b) A freshly purified pilin sample (blue) and an old pilin sample (stored for 30 days at 4 °C, black) were deposited on gold electrodes for 48 h. The pilin-electrode interfaces were then washed with 100 % ethanol and incubated for 48 h with 1 mM 1-undecanethiol to cover any exposed electrode areas. Current density was recorded at room temperature in 100 mM sodium phosphate buffer at pH 7.0 containing 100 mM NaCl, and 5 mM K<sub>3</sub>[Fe(CN)<sub>6</sub>] at a potential scan rate of 100 mV s<sup>-1</sup>.

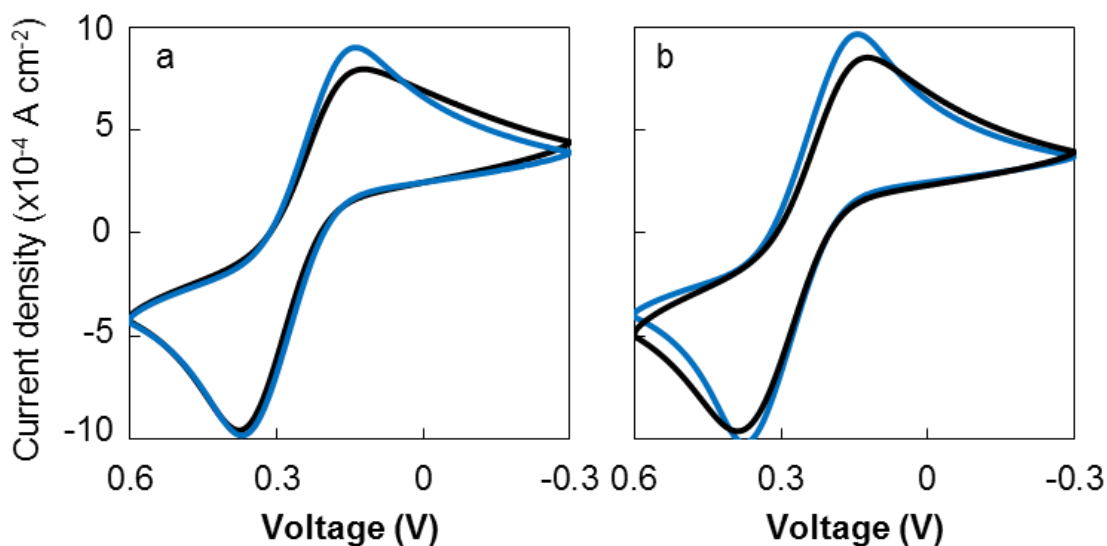


Figure 39 Effect of concentration and temperature of pilin sample on deposition of PILA<sub>19</sub>-A20C in acetonitrile

Pilins were deposited at a) the original concentration (blue) or a 1:10 dilution (black) or b) at 25 °C (black) or 4 °C for 48 h. Electrodes were then washed with 100 % ethanol and incubated for 48 h with 1 mM 1-undecanethiol. Data was recorded at room temperature in 100 mM sodium phosphate buffer at pH 7.0 containing 100 mM NaCl, and 5 mM  $\text{K}_3[\text{Fe}(\text{CN})_6]$  at a potential scan rate of  $100 \text{ mV s}^{-1}$ .

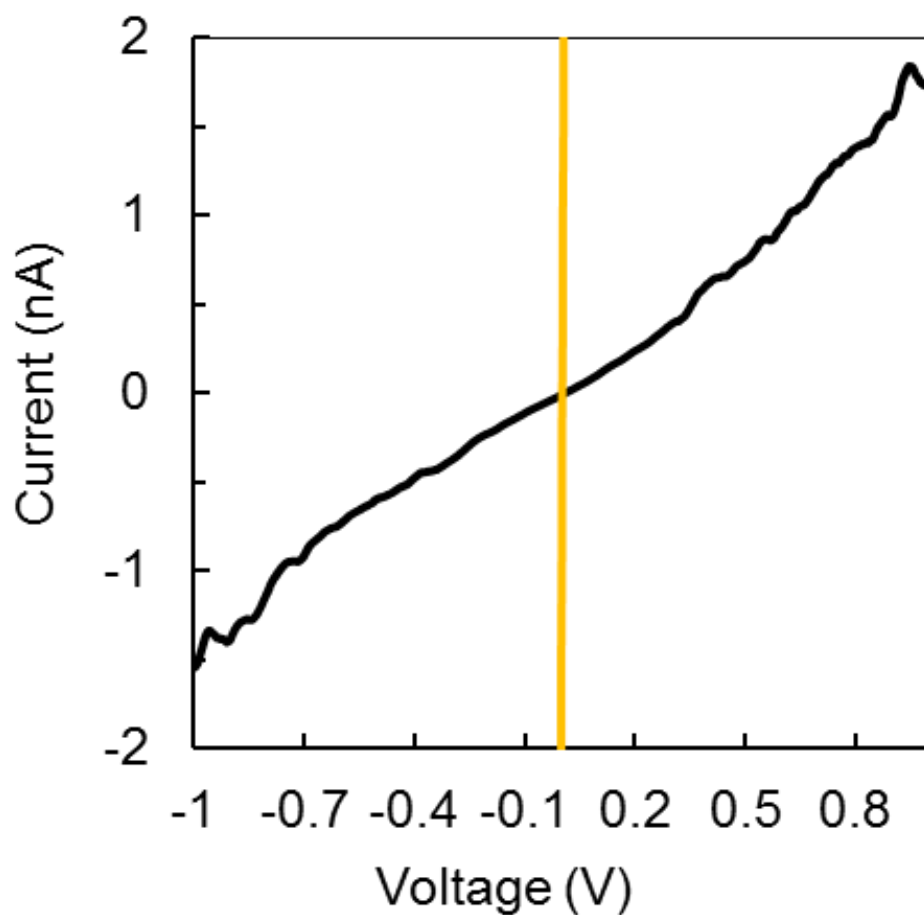


Figure 40 CP-AFM of P11A<sub>19</sub>-A20C monolayers on gold electrodes

Sample current-voltage (*I*-*V*) plots obtained after probing the transversal conductivity of a P11A<sub>19</sub>-A20C SAM coated gold electrode (black) and bare gold (yellow) at a force of 6 nN.

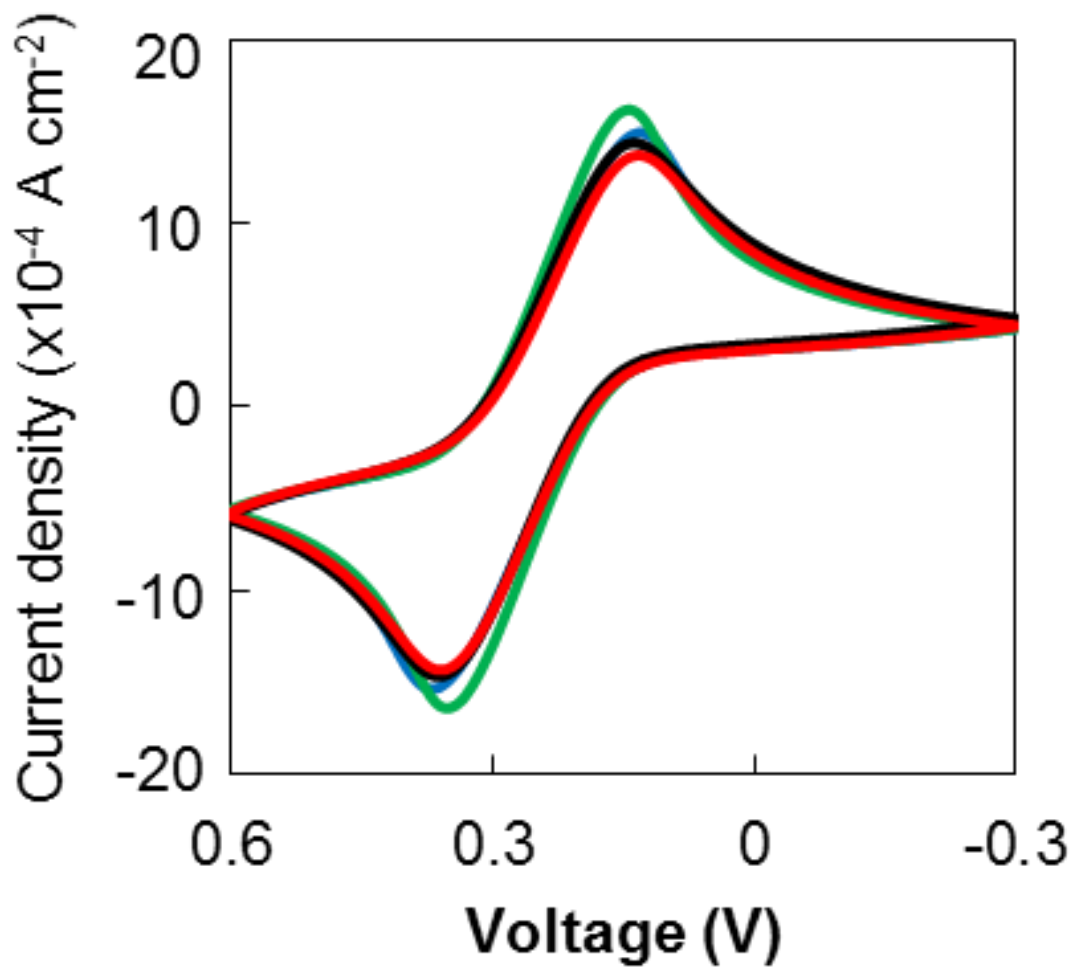


Figure 41 Effect of amino acid substitutions on cyclic voltammograms

Cyclic voltammograms of PiIA<sub>19</sub>-A20C variants deposited for 48 h: Tyr3 (green), Asp2 (red), R28A (blue) compared to wild-type (black). Electrodes were then washed with 100 % ethanol and incubated for 48 h with 1 mM 1-undecanethiol. Data were recorded at room temperature in 100 mM sodium phosphate buffer at pH 7.0 containing 100 mM NaCl, and 5 mM K<sub>3</sub>[Fe(CN)<sub>6</sub>] at a potential scan rate of 100 mV s<sup>-1</sup>.

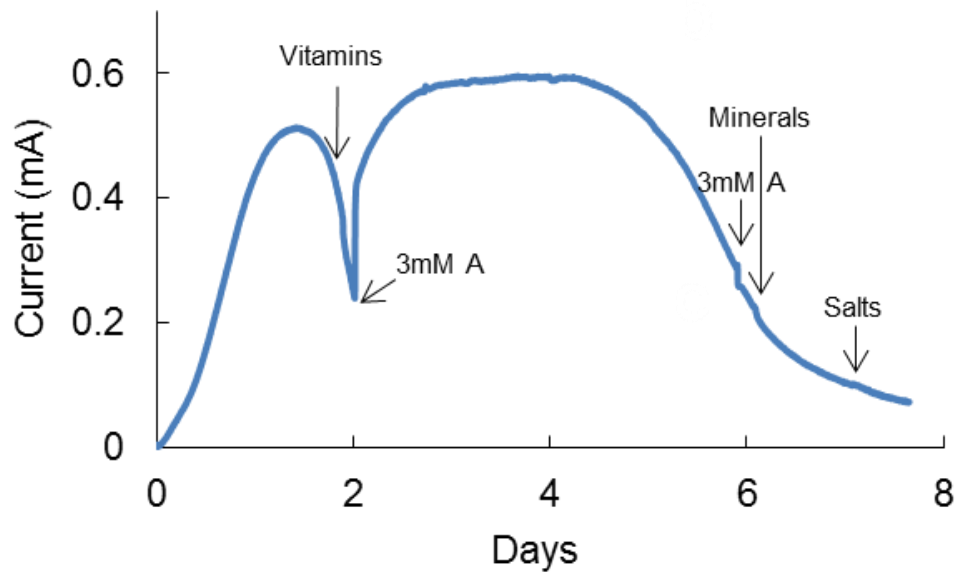


Figure 42 Test of media component limitation

After growth with 4 mM acetate current decreases regardless of the addition of more electron donor (acetate) or any other media components.

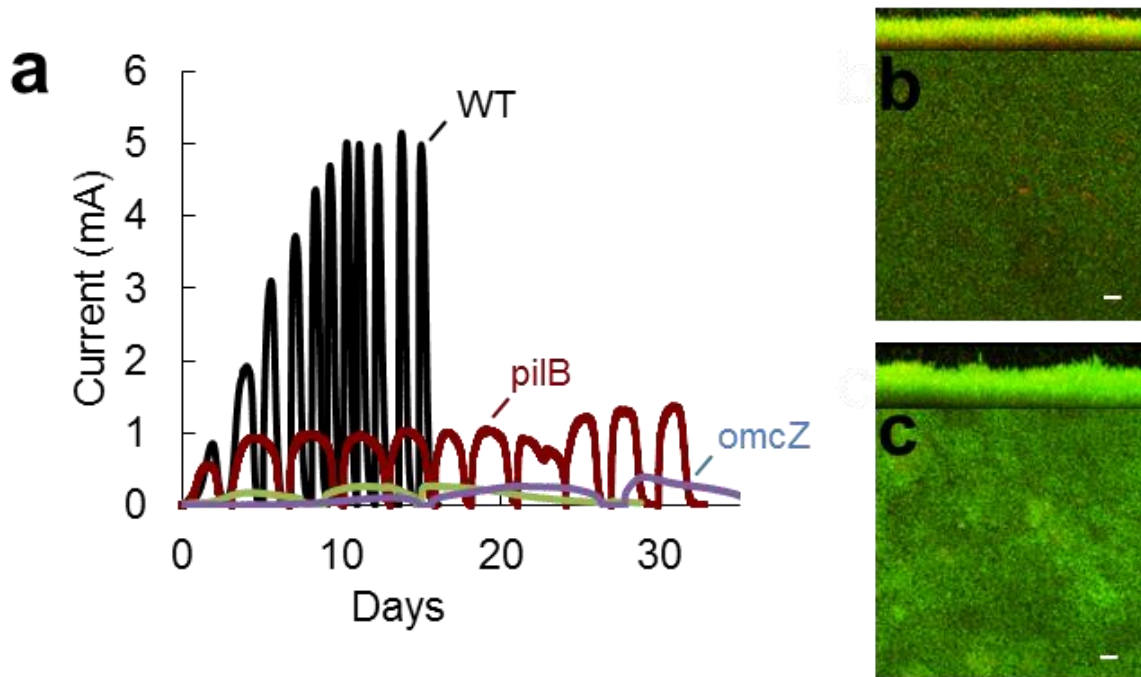


Figure 43 Growth adaptation of *pilB* after extended incubation in MFC

Current production (a) and CSLM micrographs of WT (b) and *pilB* (c) of MFCs after 10 media replacements (WT and *pilB*). CSLM micrographs are stained with the BacLight viability kit (green, live; red, dead). Scale bar, 20  $\mu\text{m}$ .

## REFERENCES

## REFERENCES

1. Röling, W. F. M. in *The Prokaryotes* 157–172 (2014). doi:10.1007/978-3-642-39044-9\_381.
2. Aklujkar, M. *et al.* The genome sequence of *Geobacter metallireducens*: features of metabolism, physiology and regulation common and dissimilar to *Geobacter sulfurreducens*. *BMC Microbiol.* **9**, 109 (2009).
3. Methé, B. A. *et al.* Genome of *Geobacter sulfurreducens*: Metal reduction in subsurface environments. *Science* **302**, 1967–1969 (2003).
4. Tremblay, P. L., Aklujkar, M., Leang, C., Nevin, K. P. & Lovley, D. A genetic system for *Geobacter metallireducens*: Role of the flagellin and pilin in the reduction of Fe(III) oxide. *Environ. Microbiol. Rep.* **4**, 82–88 (2012).
5. Coppi, M. V, Leang, C., Sandler, S. J. & Lovley, D. R. Development of a genetic system for *Geobacter sulfurreducens*. *Appl. Environ. Microbiol.* **67**, 3180–3187 (2001).
6. Lovley, D. R. *et al.* *Geobacter*. The microbe electric's physiology, ecology, and practical applications. *Adv. Microb. Physiol.* **59**, 1–100 (2011).
7. Lin, W. C., Coppi, M. V. & Lovley, D. R. *Geobacter sulfurreducens* can grow with oxygen as a terminal electron acceptor. *Appl. Environ. Microbiol.* **70**, 2525–2528 (2004).
8. Aklujkar, M. *et al.* The genome of *Geobacter bemidjiensis*, exemplar for the subsurface clade of *Geobacter* species that predominate in Fe(III)-reducing subsurface environments. *BMC Genomics* **11**, 490 (2010).
9. Summers, Z. M. *et al.* Direct exchange of electrons within aggregates of an evolved syntrophic coculture of anaerobic bacteria. *Science* **330**, 1413–1415 (2010).
10. Morita, M. *et al.* Potential for direct interspecies electron transfer in methanogenic wastewater digester aggregates. *MBio* **2**, (2011).
11. Botton, S., Van Harmelen, M., Braster, M., Parsons, J. R. & Röling, W. F. M. Dominance of *Geobacteraceae* in BTX-degrading enrichments from an iron-reducing aquifer. *FEMS Microbiol. Ecol.* **62**, 118–130 (2007).
12. Yan, J., Ritalahti, K. M., Wagner, D. D. & Löffler, F. E. Unexpected specificity of interspecies cobamide transfer from *Geobacter spp.* to organohalide-respiring *Dehalococcoides mccartyi* strains. *Appl. Environ. Microbiol.* **78**, 6630–6636 (2012).
13. Cologgi, D. L., Lampa-Pastirk, S., Speers, A. M., Kelly, S. D. & Reguera, G. Extracellular reduction of uranium via *Geobacter* conductive pili as a protective cellular mechanism. *Proc. Natl. Acad. Sci. U. S. A.* **108**, 15248–15252 (2011).

14. Bond, D. R. & Lovley, D. R. Electricity production by *Geobacter sulfurreducens* attached to electrodes. *Appl. Environ. Microbiol.* **69**, 1548–1555 (2003).
15. Cologgi, D. L., Speers, A. M., Bullard, B. A., Kelly, S. D. & Reguera, G. Enhanced uranium immobilization and reduction by *Geobacter sulfurreducens* biofilms. *Appl. Environ. Microbiol.* **80**, 6638–46 (2014).
16. Speers, A. M. & Reguera, G. Consolidated bioprocessing of AFEX-pretreated corn stover to ethanol and hydrogen in a microbial electrolysis cell. *Environ. Sci. Technol.* **46**, 7875–7881 (2012).
17. Speers, A. M., Young, J. M. & Reguera, G. Fermentation of glycerol into ethanol in a microbial electrolysis cell driven by a customized consortium. *Environ. Sci. Technol.* **48**, 6350–6358 (2014).
18. Weber, K. A., Achenbach, L. A. & Coates, J. D. Microorganisms pumping iron: Anaerobic microbial iron oxidation and reduction. *Nat. Rev. Microbiol.* **4**, 752–764 (2006).
19. Caccavo, F. *et al.* *Geobacter sulfurreducens* sp. nov., a hydrogen- and acetate-oxidizing dissimilatory metal-reducing microorganism. *Appl. Environ. Microbiol.* **60**, 3752–3759 (1994).
20. Inoue, K. *et al.* Purification and characterization of OmcZ, an outer-surface, octaheme c-type cytochrome essential for optimal current production by *Geobacter sulfurreducens*. *Appl. Environ. Microbiol.* **76**, 3999–4007 (2010).
21. Leang, C., Coppi, M. V. & Lovley, D. R. OmcB, a c-type polyheme cytochrome, involved in Fe(III) reduction in *Geobacter sulfurreducens*. *J. Bacteriol.* **185**, 2096–103 (2003).
22. Mehta, T., Coppi, M. V., Childers, S. E. & Lovley, D. R. Outer membrane c-type cytochromes required for Fe(III) and Mn(IV) oxide reduction in *Geobacter sulfurreducens*. *Appl. Environ. Microbiol.* **71**, 8634–8641 (2005).
23. Shelobolina, E. S. *et al.* Importance of c-type cytochromes for U(VI) reduction by *Geobacter sulfurreducens*. *BMC Microbiol.* **7**, 16 (2007).
24. Qian, X. *et al.* Biochemical characterization of purified OmcS, a c-type cytochrome required for insoluble Fe(III) reduction in *Geobacter sulfurreducens*. *Biochim. Biophys. Acta - Bioenerg.* **1807**, 404–412 (2011).
25. Butler, J. E., Kaufmann, F., Coppi, M. V., Núñez, C. & Lovley, D. R. MacA, a diheme c-type cytochrome involved in Fe(III) reduction by *Geobacter sulfurreducens*. *J. Bacteriol.* **186**, 4042–4045 (2004).
26. Kim, B. C. & Lovley, D. R. Investigation of direct vs. indirect involvement of the c-type cytochrome MacA in Fe(III) reduction by *Geobacter sulfurreducens*. *FEMS Microbiol. Lett.* **286**, 39–44 (2008).

27. Holmes, D. E. *et al.* Microarray and genetic analysis of electron transfer to electrodes in *Geobacter sulfurreducens*. *Environ. Microbiol.* **8**, 1805–1815 (2006).
28. Levar, C. E., Chan, C. H., Mehta-Kolte, M. G. & Bond, D. R. An inner membrane cytochrome required only for reduction of high redox potential extracellular electron acceptors. *MBio* **5**, e02034 (2014).
29. Schwertmann, U. & Cornell, R. M. *Iron oxides in the laboratory*. (Wiley-VCH Verlag GmbH, 2000). doi:10.1002/9783527613229
30. Rollefson, J. B., Stephen, C. S., Tien, M. & Bond, D. R. Identification of an extracellular polysaccharide network essential for cytochrome anchoring and biofilm formation in *Geobacter sulfurreducens*. *J. Bacteriol.* **193**, 1023–1033 (2011).
31. Reguera, G. *et al.* Biofilm and nanowire production leads to increased current in *Geobacter sulfurreducens* fuel cells. *Appl. Environ. Microbiol.* **72**, 7345–7348 (2006).
32. Reguera, G., Pollina, R. B., Nicoll, J. S. & Lovley, D. R. Possible nonconductive role of *Geobacter sulfurreducens* pilus nanowires in biofilm formation. *J. Bacteriol.* **189**, 2125–2127 (2007).
33. O'Toole, G. A. & Kolter, R. Flagellar and twitching motility are necessary for *Pseudomonas aeruginosa* biofilm development. *Mol. Microbiol.* **30**, 295–304 (1998).
34. Reguera, G. *et al.* Extracellular electron transfer via microbial nanowires. *Nature* **435**, 1098–1101 (2005).
35. Torres, C. I. *et al.* A kinetic perspective on extracellular electron transfer by anode-respiring bacteria. *FEMS Microbiol. Rev.* **34**, 3–17 (2010).
36. Inoue, K. *et al.* Specific localization of the *c*-type cytochrome OmcZ at the anode surface in current-producing biofilms of *Geobacter sulfurreducens*. *Environ. Microbiol. Rep.* **3**, 211–217 (2011).
37. Liu, Y., Kim, H., Franklin, R. R. & Bond, D. R. Linking spectral and electrochemical analysis to monitor *c*-type cytochrome redox status in living *Geobacter sulfurreducens* biofilms. *ChemPhysChem* **12**, 2235–2241 (2011).
38. Liu, Y. & Bond, D. R. Long-distance electron transfer by *G. sulfurreducens* biofilms results in accumulation of reduced *c*-type cytochromes. *ChemSusChem* **5**, 1047–1053 (2012).
39. Snider, R. M., Strycharz-Glaven, S. M., Tsoi, S. D., Erickson, J. S. & Tender, L. M. Long-range electron transport in *Geobacter sulfurreducens* biofilms is redox gradient-driven. *Proc. Natl. Acad. Sci.* **109**, 15467–15472 (2012).
40. Renslow, R. *et al.* Metabolic spatial variability in electrode-respiring *Geobacter sulfurreducens* biofilms. *Energy Environ. Sci.* **6**, 1827–1836 (2013).

41. Juárez, K. *et al.* PilR, a transcriptional regulator for pilin and other genes required for Fe(III) reduction in *Geobacter sulfurreducens*. *J. Mol. Microbiol. Biotechnol.* **16**, 146–158 (2009).
42. Leang, C., Qian, X., Mester, T. & Lovley, D. R. Alignment of the c-type cytochrome OmcS along pili of *Geobacter sulfurreducens*. *Appl. Environ. Microbiol.* **76**, 4080–4084 (2010).
43. Veazey, J. P., Reguera, G. & Tessmer, S. H. Electronic properties of conductive pili of the metal-reducing bacterium *Geobacter sulfurreducens* probed by scanning tunneling microscopy. *Phys. Rev. E - Stat. Nonlinear, Soft Matter Phys.* **84**, (2011).
44. Vargas, M. *et al.* Aromatic amino acids required for pili conductivity and long-range extracellular electron transport in *Geobacter sulfurreducens*. *MBio* **4**, (2013).
45. Feliciano, G. T. *et al.* Molecular and electronic structure of the peptide subunit of *Geobacter sulfurreducens* conductive pili from first principles. *J. Phys. Chem. A* **116**, 8023–8030 (2012).
46. Boesen, T., Nielsen, L. P. & Nielsen, P. Molecular dissection of bacterial nanowires transport mechanism. *MBio* **4**, (2013).
47. Maier, B., Potter, L., So, M., Seifert, H. S. & Sheetz, M. P. Single pilus motor forces exceed 100 pN. *Proc. Natl. Acad. Sci. USA* **99**, 16012–16017 (2002).
48. Craig, L. & Li, J. Type IV pili: paradoxes in form and function. *Curr. Opin. Struct. Biol.* **18**, 267–277 (2008).
49. Craig, L. *et al.* Type IV pilin structure and assembly: X-ray and EM analyses of *Vibrio cholerae* toxin-coregulated pilus and *Pseudomonas aeruginosa* PAK pilin. *Mol. Cell* **11**, 1139–1150 (2003).
50. Craig, L., Pique, M. E. & Tainer, J. A. Type IV pilus structure and bacterial pathogenicity. *Nat. Rev. Microbiol.* **2**, 363–378 (2004).
51. Aas, F. E. *et al.* Substitutions in the N-terminal alpha helical spine of *Neisseria gonorrhoeae* pilin affect Type IV pilus assembly, dynamics and associated functions. *Mol. Microbiol.* **63**, 69–85 (2007).
52. Strom, M. S. & Lory, S. Amino acid substitutions in pilin of *Pseudomonas aeruginosa*. Effect on leader peptide cleavage, amino-terminal methylation, and pilus assembly. *J. Biol. Chem.* **266**, 1656–1664 (1991).
53. Burrows, L. L. Twitching motility: Type IV pili in action. *Annu. Rev. Microbiol.* (2012). doi:10.1146/annurev-micro-092611-150055
54. Hartung, S. *et al.* Ultrahigh resolution and full-length pilin structures with insights for filament assembly, pathogenic functions, and vaccine potential. *J. Biol. Chem.* **286**, 44254–44265 (2011).

55. Parge, H. E. *et al.* Biochemical purification and crystallographic characterization of the fiber-forming protein pilin from *Neisseria gonorrhoeae*. *J. Biol. Chem.* **265**, 2278–2285 (1990).
56. Hazes, B., Sastry, P. A., Hayakawa, K., Read, R. J. & Irvin, R. T. Crystal structure of *Pseudomonas aeruginosa* PAK pilin suggests a main-chain-dominated mode of receptor binding. *J. Mol. Biol.* (2000). doi:10.1006/jmbi.2000.3801
57. Audette, G. F., Irvin, R. T. & Hazes, B. Purification, crystallization and preliminary diffraction studies of the *Pseudomonas aeruginosa* strain K122-4 monomeric pilin. *Acta Crystallogr. - Sect. D Biol. Crystallogr.* **59**, 1665–1667 (2003).
58. Reardon, P. N. & Mueller, K. T. Structure of the type IVa major pilin from the electrically conductive bacterial nanowires of *Geobacter sulfurreducens*. *J. Biol. Chem.* **288**, 29260–29266 (2013).
59. Keizer, D. W. *et al.* Structure of a pilin monomer from *Pseudomonas aeruginosa*: Implications for the assembly of pili. *J. Biol. Chem.* **276**, 24186–24193 (2001).
60. Nguyen, Y., Jackson, S. G., Aidoo, F., Junop, M. & Burrows, L. L. Structural characterization of novel *Pseudomonas aeruginosa* type IV pilins. *J. Mol. Biol.* **395**, 491–503 (2010).
61. Pirbadian, S. *et al.* *Shewanella oneidensis* MR-1 nanowires are outer membrane and periplasmic extensions of the extracellular electron transport components. *Proc. Natl. Acad. Sci.* **111**, 1–6 (2014).
62. Parge, H. E. *et al.* Structure of the fibre-forming protein pilin at 2.6 Å resolution. *Nature* **378**, 32–38 (1995).
63. Gorgel, M. *et al.* High-resolution structure of a type IV pilin from the metal-reducing bacterium *Shewanella oneidensis*. *BMC Struct. Biol.* **15**, 4 (2015).
64. Piepenbrink, K. H. *et al.* Structure of *Clostridium difficile* PilJ exhibits unprecedented divergence from known type iv pilins. *J. Biol. Chem.* **289**, 4334–4345 (2014).
65. Forest, K. T., Dunham, S. A., Koomey, M. & Tainer, J. A. Crystallographic structure reveals phosphorylated pilin from *Neisseria*: Phosphoserine sites modify type IV pilus surface chemistry and fibre morphology. *Mol. Microbiol.* **31**, 743–752 (1999).
66. Craig, L. *et al.* Type IV pilus structure by cryo-electron microscopy and crystallography: Implications for pilus assembly and functions. *Mol. Cell* **23**, 651–662 (2006).
67. Lauz, M., Eckhardt, S., Fromm, K. M. & Giese, B. The influence of dipole moments on the mechanism of electron transfer through helical peptides. *Phys. Chem. Chem. Phys.* **14**, 13785–8 (2012).

68. Arikuma, Y., Nakayama, H., Morita, T. & Kimura, S. Ultra-long-range electron transfer through a self-assembled monolayer on gold composed of 120 Å long  $\alpha$ -helices. *Langmuir* **27**, 1530–1535 (2011).
69. Gastric, P. *pilO*, a gene required for glycosylation of *Pseudomonas aeruginosa* 1244 pilin. *Microbiology* **141**, 1247–1254 (1995).
70. Virji, M. Post-translational modifications of meningococcal pili. Identification of common substituents: Glycans and alpha-glycerophosphate--a review. *Gene* **192**, 141–7 (1997).
71. Warren, M. J., Roddam, L. F., Power, P. M., Terry, T. D. & Jennings, M. P. Analysis of the role of pglI in pilin glycosylation of *Neisseria meningitidis*. *FEMS Immunol. Med. Microbiol.* **41**, 43–50 (2004).
72. Smedley, J. G. *et al.* Influence of pilin glycosylation on *Pseudomonas aeruginosa* 1244 pilus function. *Infect. Immun.* **73**, 7922–7931 (2005).
73. Chamot-Rooke, J. *et al.* Posttranslational modification of pili upon cell contact triggers *N. meningitidis* dissemination. *Science* **331**, 778–782 (2011).
74. Richter, L. V. Mutational analysis of geopilin function in *Geobacter sulfurreducens*. Access (Doctoral dissertation). (2011). Retrieved from ProQuest Dissertations and Theses. (Accession Order No. [3465075]).
75. Stimson, E. *et al.* Discovery of a novel protein modification: Alpha-glycerophosphate is a substituent of meningococcal pilin. *Biochem. J.* **316**, 29–33 (1996).
76. Merroun, M. L. *et al.* Complexation of uranium by cells and S-layer sheets of *Bacillus sphaericus* JG-A12. *Appl. Environ. Microbiol.* **71**, 5532–5543 (2005).
77. Malvankar, N. S. *et al.* Tunable metallic-like conductivity in microbial nanowire networks. *Nat. Nanotechnol.* **6**, 573–579 (2011).
78. Strycharz-Glaven, S. M. & Tender, L. M. Reply to the ‘Comment on “On electrical conductivity of microbial nanowires and biofilms”’ by N. S. Malvankar, M. T. Tuominen and D. R. Lovley, Energy Environ. Sci., 2012, 5, DOI: 10.1039/c2ee02613a. *Energy Environ. Sci.* **5**, 6250 (2012).
79. Malvankar, N. S. *et al.* Structural basis for metallic-like conductivity in microbial nanowires. *MBio* **6**, e00084–15– (2015).
80. Martinez, C. R. & Iverson, B. L. Rethinking the term ‘pi-stacking’. *Chem. Sci.* **3**, 2191–2201 (2012).
81. Solomon, G. C., Herrmann, C., Vura-Weis, J., Wasielewski, M. R. & Ratner, M. a. The chameleonic nature of electron transport through  $\pi$ -stacked systems. *J. Am. Chem. Soc.* **132**, 7887–7889 (2010).

82. Vura-Weis, J., Ratner, M. A. & Wasielewski, M. R. Geometry and electronic coupling in perylene-diimide stacks: Mapping structure - charge transport relationships. *J. Am. Chem. Soc.* **132**, 1738–1739 (2010).
83. Bonanni, P. S., Massazza, D. & Busalmen, J. P. Stepping stones in the electron transport from cells to electrodes in *Geobacter sulfurreducens* biofilms. *Phys. Chem. Chem. Phys.* **15**, 10300–10306 (2013).
84. Gray, H. B. & Winkler, J. R. Electron tunneling through proteins. *Q. Rev. Biophys.* **36**, 341–372 (2003).
85. Gray, H. B. & Winkler, J. R. Electron flow through proteins. *Chem. Phys. Lett.* **483**, 1–9 (2009).
86. Page, C. C., Moser, C. C., Chen, X. & Dutton, P. L. Natural engineering principles of electron tunnelling in biological oxidation-reduction. *Nature* **402**, 47–52 (1999).
87. Sek, S., Misicka, A., Swiatek, K. & Maicka, E. Conductance of alpha-helical peptides trapped within molecular junctions. *J. Phys. Chem. B* **110**, 19671–19677 (2006).
88. Arikuma, Y., Nakayama, H., Morita, T. & Kimura, S. Electron hopping over 100 Å along an  $\alpha$  helix. *Angew. Chemie - Int. Ed.* **49**, 1800–1804 (2010).
89. Brooksby, P. A., Anderson, K. H., Downard, A. J. & Abell, A. D. Voltammetric and electrochemical impedance study of ferrocenyl containing  $\beta$ -peptide monolayers on gold. *J. Phys. Chem. C* **115**, 7516–7526 (2011).
90. Horsley, J. R., Yu, J., Moore, K. E., Shapter, J. G. & Abell, A. D. Unraveling the interplay of backbone rigidity and electron rich side-chains on electron transfer in peptides: the realization of tunable molecular wires. *J. Am. Chem. Soc.* **136**, 12479–12488 (2014).
91. Zhong, D. Electron transfer mechanisms of DNA repair by photolyase. *Annu. Rev. Phys. Chem.* **66**, 691–715 (2015).
92. Reece, S. Y. & Nocera, D. G. Proton-coupled electron transfer in biology: Results from synergistic studies in natural and model systems. *Annu. Rev. Biochem.* **78**, 673–699 (2009).
93. Migliore, A., Polizzi, N. F., Therien, M. J. & Beratan, D. N. Biochemistry and theory of proton-coupled electron transfer. *Chem. Rev.* **114**, 3381–3465 (2014).
94. Ferreira, K. N., Iverson, T. M., Maghlaoui, K., Barber, J. & Iwata, S. Architecture of the photosynthetic oxygen-evolving center. *Science* **303**, 1831–1838 (2004).
95. Hays, A. M. A., Vassiliev, I. R., Golbeck, J. H. & Debus, R. J. Role of D1-His190 in proton-coupled electron transfer reactions in photosystem II: A chemical complementation study. *Biochemistry* **37**, 11352–11365 (1998).

96. Stubbe, J., Nocera, D. G., Yee, C. S. & Chang, M. C. Y. Radical initiation in the class I ribonucleotide reductase: Long-range proton-coupled electron transfer? *Chem. Rev.* **103**, 2167–2201 (2003).
97. Cordes, M. *et al.* Development of a model system for the study of long distance electron transfer in peptides. *Adv. Synth. Catal.* **350**, 1053–1062 (2008).
98. Cordes, M. *et al.* Influence of amino acid side chains on long-distance electron transfer in peptides: Electron hopping via 'stepping stones'. *Angew. Chemie - Int. Ed.* **47**, 3461–3463 (2008).
99. Dileesh, S. & Gopidas, K. R. Photophysical and electron transfer studies of a stable carbocation. *Chem. Phys. Lett.* **330**, 397–402 (2000).
100. Liang, N., Pielak, G. J., Mauk, A. G., Smith, M. & Hoffman, B. M. Yeast cytochrome *c* with phenylalanine or tyrosine at position 87 transfers electrons to (zinc cytochrome *c* peroxidase)<sup>+</sup> at a rate ten thousand times that of the serine-87 or glycine-87 variants. *Proc. Natl. Acad. Sci. U. S. A.* **84**, 1249–1252 (1987).
101. Porter, T. D. Mutagenesis at a highly conserved phenylalanine in cytochrome P450 2E1 affects heme incorporation and catalytic activity. *Biochemistry* **33**, 5942–5946 (1994).
102. Wittekindt, C., Schwarz, M., Friedrich, T. & Koslowski, T. Aromatic amino acids as stepping stones in charge transfer in respiratory complex I: An unusual mechanism deduced from atomistic theory and bioinformatics. *J. Am. Chem. Soc.* **131**, 8134–8140 (2009).
103. Cordes, M. How do amino acids transport electrons through peptides? (Doctoral dissertation). (2008). Retrieved from [http://edoc.unibas.ch/754/1/DissB\\_8284.pdf](http://edoc.unibas.ch/754/1/DissB_8284.pdf).
104. Chen, X. *et al.* Aromatic residues regulating electron relay ability of S-containing amino acids by formations of  $S\pi$  multicenter three-electron bonds in proteins. *J. Phys. Chem. C* **116**, 19682–19688 (2012).
105. Chen, X. *et al.* Relay stations for electron hole migration in peptides: Possibility for formation of three-electron bonds along peptide chains. *J. Phys. Chem. B* **112**, 14302–14311 (2008).
106. Sun, W. *et al.* Potent relay stations for electron transfer in proteins:  $\pi:\pi$  three-electron bonds. *J. Phys. Chem. C* **117**, 18325–18333 (2013).
107. Chen, X. *et al.*  $\alpha$ -Helix c-terminus acting as a relay to mediate long-range hole migration in proteins. *J. Phys. Chem. Lett.* **1**, 1637–1641 (2010).
108. Herz, T., Otto, P. & Clark, T. On the band gap in peptide  $\alpha$ -helices. *Int. J. Quantum Chem.* **79**, 120–124 (2000).

109. Gao, J. *et al.* Electron transfer in peptides: The influence of charged amino acids. *Angew. Chemie - Int. Ed.* **50**, 1926–1930 (2011).
110. Nakayama, H., Morita, T. & Kimura, S. Dipole effects on molecular and electronic structures in a novel conjugate of oligo(phenyleneethynylene) and helical peptide. *Phys. Chem. Chem. Phys.* **11**, 3967–3976 (2009).
111. Yu, J., Horsley, J. R. & Abell, A. D. The influence of secondary structure on electron transfer in peptides. *Aust. J. Chem.* **66**, 848–851 (2013).
112. Polo, F., Antonello, S., Formaggio, F., Toniolo, C. & Maran, F. Evidence against the hopping mechanism as an important electron transfer pathway for conformationally constrained oligopeptides. *J. Am. Chem. Soc.* **127**, 492–493 (2005).
113. Dey, S. K. *et al.* Study of electron transfer in ferrocene-labeled collagen-like peptides. *Langmuir* **23**, 6475–6477 (2007).
114. Yu, J. *et al.* Electron transfer through  $\alpha$ -peptides attached to vertically aligned carbon nanotube arrays: A mechanistic transition. *Chem. Commun.* **48**, 1132–1134 (2012).
115. Arikuma, Y., Takeda, K., Morita, T., Ohmae, M. & Kimura, S. Linker effects on monolayer formation and long-range electron transfer in helical peptide monolayers. *J. Phys. Chem. B* **113**, 6256–6266 (2009).
116. Hatcher, E., Balaeff, A., Keinan, S., Venkatramani, R. & Beratan, D. N. PNA versus DNA: Effects of structural fluctuations on electronic structure and hole-transport mechanisms. *J. Am. Chem. Soc.* **130**, 11752–11761 (2008).
117. Sleutels, T. H. J. A., Ter Heijne, A., Buisman, C. J. N. & Hamelers, H. V. M. Bioelectrochemical systems: An outlook for practical applications. *ChemSusChem* **5**, 1012–1019 (2012).
118. Borole, A. P. *et al.* Electroactive biofilms: Current status and future research needs. *Energy Environ. Sci.* **4**, 4813–4834 (2011).
119. Nevin, K. P. *et al.* Anode biofilm transcriptomics reveals outer surface components essential for high density current production in *Geobacter sulfurreducens* fuel cells. *PLoS One* **4**, e5628 (2009).
120. Richter, H. *et al.* Cyclic voltammetry of biofilms of wild type and mutant *Geobacter sulfurreducens* on fuel cell anodes indicates possible roles of OmcB, OmcZ, type IV pili, and protons in extracellular electron transfer. *Energy Environ. Sci.* **2**, 506–516 (2009).
121. Dalton, E. F. *et al.* Charge transport in electroactive polymers consisting of fixed molecular redox sites. *Chem. Phys.* **141**, 143–157 (1990).
122. Speers, A. M. & Reguera, G. Electron donors supporting growth and electroactivity of *Geobacter sulfurreducens* anode biofilms. *Appl. Environ. Microbiol.* **78**, 437–444 (2012).

123. Marx, C. J. & Lidstrom, M. E. Broad-host-range cre-lox system for antibiotic marker recycling in Gram-negative bacteria. *Biotechniques* **33**, 1062–1067 (2002).
124. Kim, B. C. *et al.* OmcF, a putative c-type monoheme outer membrane cytochrome required for the expression of other outer membrane cytochromes in *Geobacter sulfurreducens*. *J. Bacteriol.* **187**, 4505–4513 (2005).
125. McKinlay, J. B., Zeikus, J. G. & Vieille, C. Insights into *Actinobacillus succinogenes* fermentative metabolism in a chemically defined growth medium. *Appl. Environ. Microbiol.* **71**, 6651–6656 (2005).
126. Heydorn, a *et al.* Quantification of biofilm structures by the novel computer program COMSTAT. *Microbiology* **146** ( Pt 1, 2395–2407 (2000).
127. Schmittgen, T. D. & Livak, K. J. Analyzing real-time PCR data by the comparative C(T) method. *Nat. Protoc.* **3**, 1101–1108 (2008).
128. Senko, J. M. & Stolz, J. F. Evidence for iron-dependent nitrate respiration in the dissimilatory iron-reducing bacterium *Geobacter metallireducens*. *Appl. Environ. Microbiol.* **67**, 3750–3752 (2001).
129. Takaichi, S. & Morita, S. Procedures and conditions for application of the pyridine hemochrome method to photosynthetically grown cells of *Rhodospseudomonas sphaeroides*. *J. Biochem.* **89**, 1513–1519 (1981).
130. Thomas, P. E., Ryan, D. & Levin, W. An improved staining procedure for the detection of the peroxidase activity of cytochrome P-450 on sodium dodecyl sulfate polyacrylamide gels. *Anal. Biochem.* **75**, 168–176 (1976).
131. Burrows, L. L. *Pseudomonas aeruginosa* twitching motility: Type IV pili in action. *Annu. Rev. Microbiol.* **66**, 493–520 (2012).
132. Hentzer, M. *et al.* Alginate overproduction affects *Pseudomonas aeruginosa* biofilm structure and function. *J. Bacteriol.* **183**, 5395–5401 (2001).
133. Strycharz-Glaven, S. M., Snider, R. M., Guiseppi-Elie, A. & Tender, L. M. On the electrical conductivity of microbial nanowires and biofilms. *Energy Environ. Sci.* **4**, 4366–4379 (2011).
134. Babauta, J. T., Nguyen, H. D., Harrington, T. D., Renslow, R. & Beyenal, H. pH, redox potential and local biofilm potential microenvironments within *Geobacter sulfurreducens* biofilms and their roles in electron transfer. *Biotechnol. Bioeng.* **109**, 2651–2662 (2012).
135. Robuschi, L. *et al.* Spectroscopic slicing to reveal internal redox gradients in electricity-producing biofilms. *Angew. Chem. Int. Ed. Engl.* **52**, 925–928 (2013).

136. Marsili, E., Sun, J. & Bond, D. R. Voltammetry and growth physiology of *Geobacter sulfurreducens* biofilms as a function of growth stage and imposed electrode potential. *Electroanalysis* **22**, 865–874 (2010).
137. Feliciano, G. T., Steidl, R. J. & Reguera, G. Structural and functional insights into the conductive pili of *Geobacter sulfurreducens* revealed in molecular dynamics simulations. *Phys. Chem. Chem. Phys.* **17**, 22217–22226 (2015).
138. Yang, Z., Lux, R., Hu, W., Hu, C. & Shi, W. PilA localization affects extracellular polysaccharide production and fruiting body formation in *Myxococcus xanthus*. *Mol. Microbiol.* **76**, 1500–1513 (2010).
139. Withers, R. T., Damron, H. F., Yin, Y. & Yu, H. D. Truncation of type IV pilin induces mucoidy in *Pseudomonas aeruginosa* strain PAO579. *Microbiologyopen* **2**, 459–470 (2013).
140. Lu, H. M., Motley, S. T. & Lory, S. Interactions of the components of the general secretion pathway: Role of *Pseudomonas aeruginosa* type IV pilin subunits in complex formation and extracellular protein secretion. *Mol. Microbiol.* **25**, 247–259 (1997).
141. Strom, M. S., Nunn, D. & Lory, S. Multiple roles of the pilus biogenesis protein PilD: involvement of PilD in excretion of enzymes from *Pseudomonas aeruginosa*. *J. Bacteriol.* **173**, 1175–1180 (1991).
142. Richter, L. V, Sandler, S. J. & Weis, R. M. Two isoforms of *Geobacter sulfurreducens* PilA have distinct roles in pilus biogenesis, cytochrome localization, extracellular electron transfer, and biofilm formation. *J. Bacteriol.* **194**, 2551–2563 (2012).
143. Esteve-Núñez, A., Sosnik, J., Visconti, P. & Lovley, D. R. Fluorescent properties of c-type cytochromes reveal their potential role as an extracytoplasmic electron sink in *Geobacter sulfurreducens*. *Environ. Microbiol.* **10**, 497–505 (2008).
144. Chin, K., Esteve-Núñez, A., Leang, C. & Lovley, D. R. Direct correlation between rates of anaerobic respiration and levels of mRNA for key respiratory genes in *Geobacter sulfurreducens*. *Appl. Environ. Microbiol.* **70**, 5183–5189 (2004).
145. Stephen, C. S., LaBelle, E. V, Brantley, S. L. & Bond, D. R. Abundance of the multiheme c-type cytochrome OmcB increases in outer biofilm layers of electrode-grown *Geobacter sulfurreducens*. *PLoS One* **9**, e104336 (2014).
146. Bonanni, P. S., Bradley, D. F., Schrott, G. D. & Busalmen, J. P. Limitations for current production in *Geobacter sulfurreducens* biofilms. *ChemSusChem* **6**, 711–720 (2013).
147. Franks, A. E. *et al.* Novel strategy for three-dimensional real-time imaging of microbial fuel cell communities: monitoring the inhibitory effects of proton accumulation within the anode biofilm. *Energy Environ. Sci.* **2**, 113 (2009).

148. Carra, C., Iordanova, N. & Hammes-Schiffer, S. Proton-coupled electron transfer in a model for tyrosine oxidation in photosystem II. *J. Am. Chem. Soc.* **125**, 10429–10436 (2003).
149. Okegbe, C., Price-Whelan, A. & Dietrich, L. E. P. Redox-driven regulation of microbial community morphogenesis. *Curr. Opin. Microbiol.* **18**, 39–45 (2014).
150. McGaughey, G. B., Gagné, M., Rappé, A. K., Gagne, M. & Rappe, A. K.  $\pi$ -Stacking interactions. Alive and well in proteins. *J. Biol. Chem.* **273**, 15458–15463 (1998).
151. Cordes, M. & Giese, B. Electron transfer in peptides and proteins. *Chem. Soc. Rev.* **38**, 892–901 (2009).
152. Giese, B., Graber, M. & Cordes, M. Electron transfer in peptides and proteins. *Curr. Opin. Chem. Biol.* **12**, 755–759 (2008).
153. Shih, C. *et al.* Tryptophan-accelerated electron flow through proteins. *Science* **320**, 1760–1762 (2008).
154. Wang, M., Gao, J., Müller, P. & Giese, B. Electron transfer in peptides with cysteine and methionine as relay amino acids. *Angew. Chemie - Int. Ed.* **48**, 4232–4234 (2009).
155. Nugent, J. H. Oxygenic photosynthesis. Electron transfer in photosystem I and photosystem II. *Eur. J. Biochem.* **237**, 519–531 (1996).
156. Yu, J., Huang, D. M., Shapter, J. G. & Abell, A. D. Electrochemical and computational studies on intramolecular dissociative electron transfer in  $\beta$ -peptides. *J. Phys. Chem. C* **116**, 26608–26617 (2012).
157. Okamoto, S., Morita, T. & Kimura, S. Electron transfer through a self-assembled monolayer of a double-helix peptide with linking the terminals by ferrocene. *Langmuir* **25**, 3297–3304 (2009).
158. Yu, J., Horsley, J. R., Moore, K. E., Shapter, J. G. & Abell, A. D. The effect of a macrocyclic constraint on electron transfer in helical peptides: a step towards tunable molecular wires. *Chem. Commun. (Camb)*. **50**, 1652–4 (2014).
159. Reguera, G., Tessmer, S., Veazey, J. & Lampa-Pastirk, S. Microbial nanowires and products related thereto. (2012). U.S. Patent Application Serial No. 13/221,495, filed August 30, 2011, claiming priority to U.S. Provisional Patent Application Serial No. 61/378,240 filed on August 30, 2010.
160. Benavides-Garcia, M. G. & Balasubramanian, K. Structural insights into the binding of uranyl with human serum protein apotransferrin structure and spectra of protein-uranyl interactions. *Chem. Res. Toxicol.* **22**, 1613–1621 (2009).
161. Yu, J.-Y., Chung, S.-W. & Heath, J. R. Silicon nanowires: Preparation, device fabrication, and transport properties. *J. Phys. Chem. B* **104**, 11864–11870 (2000).

162. Barkleit, A., Moll, H. & Bernhard, G. Complexation of uranium(VI) with peptidoglycan. *Dalton Trans.* 5379–5385 (2009). doi:10.1039/b818702a
163. Reguera, G. Electron transfer at the cell-uranium interface in *Geobacter spp.* *Biochem. Soc. Trans.* **40**, 1227–32 (2012).
164. Reguera, G. & Steidl, R. Microbial nanowires. (2014). U.S. Patent Application Serial No. 13/221,495, filed August 30, 2011, claiming priority to U.S. Provisional Patent Application Serial No. 61/378,188, filed on August 30, 2010.
165. Shin, Y. G. K., Newton, M. D. & Isied, S. S. Distance dependence of electron transfer across peptides with different secondary structures: The role of peptide energetics and electronic coupling. *J. Am. Chem. Soc.* **125**, 3722–3732 (2003).
166. Castro Forero, A. Properties and applications of self-assembled biomolecules in nanostructured biomimetic interfaces (Doctoral dissertation). (2011). Retrieved from ProQuest Dissertations and Theses. (Accession Order No. [3489777]).
167. Conchillo-Solé, O. *et al.* AGGRESKAN: A server for the prediction and evaluation of 'hot spots' of aggregation in polypeptides. *BMC Bioinformatics* **8**, 65 (2007).
168. Kyte, J. & Doolittle, R. F. A simple method for displaying the hydropathic character of a protein. *J. Mol. Biol.* **157**, 105–132 (1982).
169. Rosano, G. L. & Ceccarelli, E. A. Recombinant protein expression in *Escherichia coli*: Advances and challenges. *Front. Microbiol.* **5**, 177–202 (2014).
170. Schägger, H. Tricine-SDS-PAGE. *Nat. Protoc.* **1**, 16–22 (2006).
171. Sasaki, Y. C. *et al.* Two-dimensional arrangement of a functional protein by cysteine-gold interaction: enzyme activity and characterization of a protein monolayer on a gold substrate. *Biophys. J.* **72**, 1842–1848 (1997).
172. Sek, S., Swiatek, K. & Misicka, A. Electrical behavior of molecular junctions incorporating alpha-helical peptide. *J. Phys. Chem. B* **109**, 23121–23124 (2005).
173. Pawlowski, J., Juhaniwicz, J., Tymecka, D. & Sek, S. Electron transfer across  $\alpha$ -helical peptide monolayers: Importance of interchain coupling. *Langmuir* **28**, 17287–17294 (2012).
174. Agonafer, D. D., Chainani, E., Oruc, M. E., Lee, K. S. & Shannon, M. A. Study of insulating properties of alkanethiol self-assembled monolayers formed under prolonged incubation using electrochemical impedance spectroscopy. *J. Nanotechnol. Eng. Med.* **3**, 031006 (2013).
175. Sek, S., Tolak, A., Misicka, A., Palys, B. & Bilewicz, R. Asymmetry of electron transmission through monolayers of helical polyalanine adsorbed on gold surfaces. *J. Phys. Chem. B* **109**, 18433–18438 (2005).

176. Uji, H., Morita, T. & Kimura, S. Molecular direction dependence of single-molecule conductance of a helical peptide in molecular junction. *Phys. Chem. Chem. Phys.* **15**, 757–760 (2013).
177. Klimes, A. *et al.* Production of pilus-like filaments in *Geobacter sulfurreducens* in the absence of the type IV pilin protein PilaA. *FEMS Microbiol. Lett.* **310**, 62–68 (2010).
178. Smith, J. A. *et al.* Going wireless: Fe(III) oxide reduction without pili by *Geobacter sulfurreducens* strain JS-1. *Appl. Environ. Microbiol.* **80**, 4331–4340 (2014).
179. Aas, F. E. *et al.* *Neisseria gonorrhoeae* type IV pili undergo multisite, hierarchical modifications with phosphoethanolamine and phosphocholine requiring an enzyme structurally related to lipopolysaccharide phosphoethanolamine transferases. *J. Biol. Chem.* **281**, 27712–27723 (2006).
180. Chang, M. C. Y., Yee, C. S., Stubbe, J. & Nocera, D. G. Turning on ribonucleotide reductase by light-initiated amino acid radical generation. *Proc. Natl. Acad. Sci. U. S. A.* **101**, 6882–6887 (2004).
181. Lukacs, A., Eker, A. P. M., Byrdin, M., Brettel, K. & Vos, M. H. Electron hopping through the 15 Å triple tryptophan molecular wire in DNA photolyase occurs within 30 ps. *J. Am. Chem. Soc.* **130**, 14394–14395 (2008).
182. Irebo, T., Reece, S. Y., Sjodin, M., Nocera, D. G. & Hammarstrom, L. Proton-coupled electron transfer of tyrosine oxidation: Buffer dependence and parallel mechanisms. *J. Am. Chem. Soc.* **129**, 15462–15464 (2007).
183. Arikuma, Y., Nakayama, H., Morita, T. & Kimura, S. Ultra-long-range electron transfer through a self-assembled monolayer on gold composed of 120-Å-long  $\alpha$ -helices. *Langmuir* **27**, 1530–1535 (2011).
184. Arikuma, Y., Takeda, K., Morita, T., Ohmae, M. & Kimura, S. Linker effects on monolayer formation and long-range electron transfer in helical peptide monolayers. *J. Phys. Chem. B* **113**, 6256–6266 (2009).
185. Guex, N. & Peitsch, M. C. SWISS-MODEL and the Swiss-PdbViewer: An environment for comparative protein modeling. *Electrophoresis* **18**, 2714–2723 (1997).